6

Aerodynamic Measurement and Analysis of the Flow in an Uncooled Turbine Stage

by

Léo M. Grépin

B. Eng. Honours Mechanical Engineering, McGill University (1996)

Submitted to the Department of Aeronautics and Astronautics
in partial fulfillment of the requirements for the degree of

Master of Science

at the

Massachusetts Institute of Technology

June 1998

Author_____
Department of Aeronautics and Astronautics
May 15, 1998

Certified by_____
Professor Alan H. Epstein
R. C. Maclaurin Professor of Aeronautics and Astronautics
Thesis Supervisor

Accepted by_____
Professor Jaime Peraire
Associate Professor of Aeronautics and Astronautics
Chair, Graduate Office

Aerodynamic Measurement and Analysis of the Flow in an Uncooled Turbine Stage

by

Léo M. Grépin

Submitted to the Department of Aeronautics and Astronautics
on May 15, 1998, in partial fulfillment of the
requirements for the degree of
Master of Science

Abstract

This thesis is part of an effort to develop new instrumentation techniques for blowdown turbine testing. Two experimental methods used to study turbine aerodynamics in the MIT Blowdown Turbine Facility are presented:

Differential pressure measurement - The high accuracy performance study of a turbine stage motivated research in mass flow measurement techniques in a blowdown environment. A combination of total and differential pressure and total temperature measurements was used to calculate the mass flow per unit area through the turbine stage. The design of a new differential pressure probe was a critical component of the research effort. Measurement uncertainties of less than 1% were required while operating near the sensor burst pressure. The mass flow measurements, accurate to 1%, served to validate mass flow measurements simultaneously acquired using a Venturi nozzle mass flow meter.

Particle Image Velocimetry - A successful application of particle image velocimetry in a fully-scaled rotating turbine rig is presented. The image processing procedure is described and the results are assessed using a comparison with a numerical solution. The CFD code used is a coupled Navier-Stokes/Euler 2-D solver with rotor/stator interaction. Differences of 20 to 60% between CFD and PIV local velocities were partially explained by modeling the motion of seeding particles in the turbine stage and assessing the influence of particle diameter on PIV accuracy. For the present application, 0.5 μm was found to be the maximum seeding particle size for tracking errors of less than 5%. The PIV results supported previous research in predicting substantial aperiodic unsteadiness in the rotor/stator passage.

Thesis Supervisor: Professor Alan H. Epstein
Title: R. C. Maclaurin Professor of Aeronautics and Astronautics

À LA MÉMOIRE DE MES GRANDS-PARENTS

ACKNOWLEDGMENTS

I would like to express my gratitude to Professor Alan Epstein and Dr. Gerald Guenette, for their guidance, encouragement and insightful suggestions throughout this work.

I am greatly indebted to: Lori Martinez, Holly Anderson, Bob Haimes, Viktor Dubrowski, Mariano Hellwig, James Letendre, Tom Ryan and Bill Haimes, for their invaluable administrative and technical support.

I am grateful to the students who worked with me on the Blowdown Turbine for always being helpful and for sharing with me explosions of joy and explosions of equipment: Rory Keogh, Jason Jacobs, Yi Cai and Chris Spadaccini.

I would like to thank all the friends who made my MIT experience unforgettable. Namely, Amit and Arnaud, for corrupting me into playing golf on busy week-ends; Luc for sharing with me memories of "poutine" and thoughts on life; Rory for our heated discussions on the "Wild,Wild West" and world issues; Zolti, for being more of a brother than a roommate to me; "les potes francais", Jérémie, Sophie, Omar and Ahmed for putting a little bit of France in the Boston sky, and finally all the people at the GTL for making everyday an interesting one.

Finally, I thank my family; you guided me, helped me, supported me without ever criticizing my decisions; you are my motivation and drive.

And Anna, my Love for you is behind every word in this thesis.

This project was sponsored by the US Air Force Office of Scientific Research Grant F49620-96-1-0266. Their support is gratefully acknowledged.

CONTENTS

List of Figures

List of Tables

NOMENCLATURE

Roman

a	speed of sound ($\sqrt{\gamma RT}$) $[m/s]$
A_c	frontal area of seed particle $[m^2]$
A_{eff}	effective area $[m^2]$
C_D	drag coefficient
C_p	mass specific heat capacity at constant pressure $[J/kg.K]$
d	seed particle diameter $[m]$
D	diameter $[m]$
L	length $[m]$
m	mass $[kg]$
M	Mach number ($\frac{\|\vec{V}\|}{a}$)
n	number of statistical samples
P	pressure $[Pa]$
δP	dynamic pressure $[Pa]$
R_{gas}	gas constant $[J/kg.K]$
s	curvilinear coordinate $[m]$
S_1	Sutherland's temperature constant $[K]$
t	time $[s]$
T	temperature $[K]$
u	axial component of velocity $[m/s]$
v	circumferential component of velocity $[m/s]$
V	volume of seed particle $[m^3]$
$\vec{V}$	velocity vector $[m/s]$
x	axial location $[m]$

$\vec{x}$	Cartesian position vector $[m]$
y	circumferential location $[m]$

Greek

γ	ratio of specific heats
ϵ	measurement uncertainty
θ	rotor inlet flow angle (from axial)
κ	rotor/stator index
μ	dynamic viscosity $[kg/m.sec]$
π	turbine pressure ratio
ρ	density $[kg/m^3]$
τ	torque $[N.m]$
ω	turbine angular speed $[rad/s]$

Superscripts

$\dot{}$	derivative with respect to time

Subscripts

f	fluid particle property
p	seed particle property
t	stagnation (or total) fluid quantity
1	supply tank
4	nozzle guide vane inlet

CHAPTER 1

INTRODUCTION

1.1 Background

The globalization and deregulation of the aeronautical industry in the last few decades has forced industry players to compete both on quality and price. The consequence of this has been two fold. Incremental improvements in technology have become crucial for competitive advantage and the budgets feeding the research have shrunk drastically. In the commercial and military industry, most development projects have evolved to include few test rigs. In the power generation industry where the engines and power requirements are large, components are tested in service.

This evolution in the research and development of gas turbine engines was made possible by advances in computer power and design tools such as computational fluid dynamics (CFD) and CAD/CAM programs. Certain design steps, however, still rely on empirical approaches. For example, the trade-offs involved in the design of cooled turbines have yet to be captured by computational tools and significant testing is still necessary during the development of a new engine.

To replace steady test rigs, short-duration transient facilities were developed in the 1980's to study components of gas turbine engines at fractions of the energy requirements and construction costs. The MIT Blowdown Turbine test rig is such a facility. It has been successfully used to study, amongst other things, the effect of inlet temperature distortions on turbine heat transfer and the impact of film cooling on heat transfer and efficiency.

This thesis focuses on demonstrating the feasibility of new applications in a blowdown environment. Namely, the design of a dynamic pressure probe is investigated along with its suitability for inferring Mach number and mass flow when combined with stagnation pressure and temperature sensors. Also, particle-image velocimetry (PIV) is studied as a candidate for obtaining instantaneous flow fields in a transient environment by non-intrusive means.

1.2 Literature Review

The MIT Blowdown Turbine Facility was one of the first short duration turbomachinery experiments developed in the early 1980's. Papers by Epstein [14] and Guenette [20] present the issues involved in the design of such a facility. The importance of time and physical scales is thoroughly discussed as well as the instrumentation required in unsteady short-duration testing.

During the past fifteen years, the MIT blowdown turbine facility has been successfully used to study key phenomena affecting turbine flow:

1. The effect of film cooling on blade heat transfer was investigated by Abhari [1] by measuring the heat transfer coefficient on the blade surface for cooled and uncooled blades. The results obtained in the blowdown turbine rig were compared to results obtained in a cascade facility and the unsteady nature of the cooling process was studied using a mathematical model.

2. The effect of inlet temperature distortions on turbine heat transfer was studied by Shang [27] in conditions typical of combustor exit flows. Radial temperature distortions were found to have a profound influence on blade heat transfer while circumferential distortions did not. The experimental study was complemented by a computational investigation of the mechanisms driving rotor blade surface heat transfer.

3. The latest research focuses on the effects of film cooling on turbine performance. The research was undertaken by Keogh [24] and Cai [9]. Most of the early efforts focused on developing instrumentation to accurately monitor the facility as efficiency

calculations require low-uncertainty measurements of mass flow, shaft torque, pressure and temperature.

1.3 Motivation and Objectives

The main motivation behind this work is the need for more accurate and complete tools to study, in a blowdown facility, the factors affecting turbine flow. More specifically, two experimental methods are examined as candidates to further the flexibility of transient turbine testing:

1. The measurement of dynamic pressure: Dynamic pressure measurements can be combined with total pressure and temperature measurements to infer Mach number and mass flow. The challenge in a blowdown environment is to accurately capture changes in differential pressure that are fractions of percents of the common mode pressure. In addition, the common mode pressure varies during a test between vacuum and several atmospheres, creating tremendous stress on the sensor.

2. Particle-image velocimetry: PIV can generate instantaneous velocity fields for unsteady flows. if the concept of PIV can be validated for turbomachinery flows, it would have many applications: at the design stage, the results can be used to fine tune blade shapes for unsteady effects, at the academic level, they can be used as a reference to validate CFD codes or to investigate unsteady effects in turbines.

As such, the specific objectives of this thesis are as follows:

1. To demonstrate the feasibility of a dynamic pressure probe in a blowdown environment.

2. To bound the accuracy of Mach number and mass flow calculations obtained from pressure and temperature measurements in a short-duration, transient experiment.

3. To demonstrate the feasibility and the potential of particle image velocimetry for transonic flow visualization and CFD code validation.

4. To quantify the difference between PIV and CFD solutions for the flow through the Rolls-Royce ACE turbine.

5. To identify the sources of discrepancies between the PIV and CFD results.

1.4 The MIT Blowdown Turbine Test Facility

This section describes the facility used for the acquisition of the experimental data contained in this thesis. The MIT Blowdown Turbine Facility is a fully scaled short duration transient wind tunnel. A detailed explanation of the design and operation of the facility can be found in references [14] and [20]. The following is a brief description of the operating concepts.

A blowdown turbine experiment rigorously simulates the operational environment of a transonic engine turbine stage: (1) the properties of the flow (pressure, temperature, mass flow) change throughout a test but the non-dimensional parameters governing fluid dynamic and heat transfer phenomena remain constant; (2) the time-scales of the flow and the rotor to stator passing frequency are much smaller than the test time of approximately 500 ms so that the turbine operates in a quasi-steady state similar to the steady state operation of an engine.

The test stage is a scaled down version of the stage in the full engine. Table 1.1 presents the characteristics of the 2:1 pressure ratio ground based turbine stage used for the development of the mass flow probe described in Chapter 2. The particle image velocimetry experiment, discussed in Chapter 3 was conducted on a 4:1 pressure ratio turbine stage, the scaling parameters of which are summarized in Table 3.1.

The choice of the test gas and of its initial conditions is based on the need to match relevant non-dimensional parameters and to maximize the safety of the facility. *Argon* and CO_2 are used in the experiments presented in this thesis. Due to the high density of the working gas, the Reynolds number similarity can be achieved at low pressure and, due to the high density, the tip Mach number similarity can be satisfied at a fairly low Mach number. The mixture ratio is set to match the specific heat ratio, γ, of the full-scale turbine.

A schematic of the blowdown turbine facility is presented in figure 1-1. The main components are the supply tank, the fast acting valve, the test section, the downstream

Parameters	Full Scale Engine	MIT BDT
Working Fluid	Air	$Argon - CO_2$
Ratio of Specific Heats, γ	1.28	1.28
Mean Metal Temperature	1100 K	300 K
Metal/Gas Temp. Ratio	0.647	0.647
Inlet Total Temperature	1700 K	464 K
Midspan NGV Chord	0.15 m	0.0365 m
Reynolds Number	5.6×10^6	5.6×10^6
Inlet Total Pressure	15 atm	7 atm
Exit Total Pressure	7.4 atm	3.47 atm
Exit Total Temperature	1470 K	401 K
Prandtl Number	0.928	0.742
Design Rotor Speed	3600 rpm	5954 rpm
Design Mass Flow	312 kg/s	23.3 kg/s
Turbine Power Output	91 MW	1.26 MW
Test Time	$Continuous$	0.3 sec

Table 1.1: MIT blowdown turbine scaling for a ground based turbine stage at design point.

translator and the dump tank. The cross sectional view of the test section, in figure 1-2, shows the flowpath and some of the instrumentation.

During a blowdown test, the facility is pumped down to vacuum and the supply tank is heated to the desired temperature. The fast acting valve is closed and the supply tank is filled to test pressure. All the pressure sensors undergo a post-fill calibration. After setting the data acquisition system, translator and eddy current brake to standby mode, the rotor is spun up in vacuum by a drive motor to a speed slightly above the test speed. The drive motor is shut off and the rotor slows down due to friction in the bearings. When the rotor speed reaches the test speed, the fast acting valve opens in 20-50 ms and the eddy current brake, translator and data acquisition system are triggered. The test gas from the supply tank enters a contraction which simulates the combustor exit upstream of the nozzle guide vanes. Boundary layer bleeds are located upstream of the contraction and ensure a uniform velocity profile at the inlet of the test section. The turbine pressure ratio is set by a throttle plate downstream of the test section. Start-up transients decay in about 200 ms and are followed by 500-800 ms during which the throttle plate remains choked. For the 2:1 pressure ratio turbine tests, the first 1000 ms of data are acquired at 3.03 kHz. The facility is then monitored at 1 Hz for 9 min to track the decay of the flow and to conduct post-test sensor calibrations.

1.5 Organization of the Thesis

This chapter introduces the content of the thesis, presents previous research undertaken in a blowdown environment, outlines the motivations behind this research and describes the characteristics of the MIT blowdown turbine facility.

Chapter two treats the need for and complexity of differential pressure measurements in a blowdown environments. A method for inferring Mach number and mass flow from flow property measurements is presented along with its implementation and the results of the tests.

Chapter three presents some of the first data obtained in rotating turbomachinery using Particle Image Velocimetry (PIV). The experimental apparatus and the image processing algorithm are described, along with the results of the particle image velocimetry experiments.

In chapter four, Computational Fluid Dynamics (CFD) results are presented as a basis for comparison with the PIV data. The numerical algorithm used is described, as well as the details of the calculations.

Chapter five is a comparison between the results of the two previous chapters. It presents the agreement of the experimental and computational solutions to the flow field through the ACE turbine and discusses sources of discrepancies.

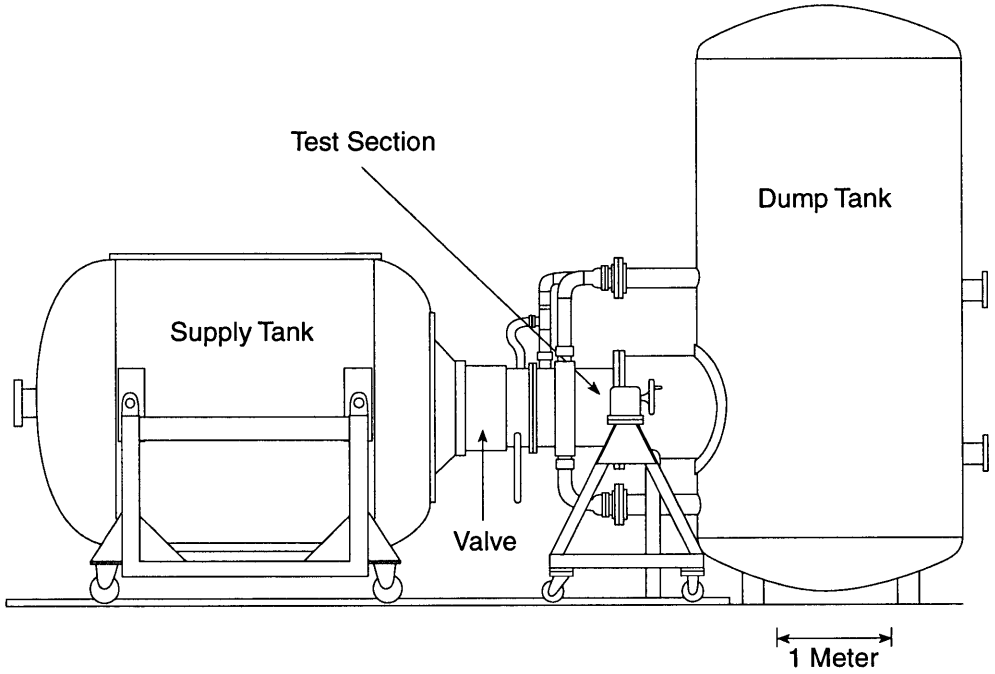

Figure 1-1: The MIT Blowdown Turbine Facility.

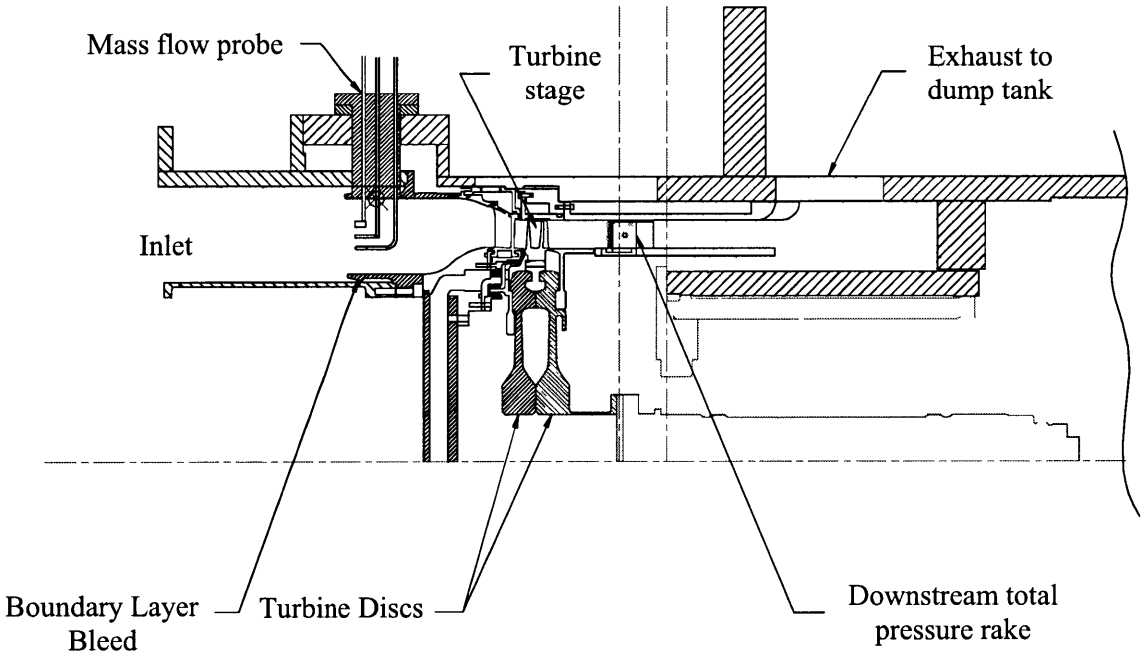

Figure 1-2: The MIT Blowdown Turbine Facility flow path. Note: the mass flow probe is described in Chapter 2.

Chapter 2

Measurement of Dynamic Pressure

2.1 Introduction

Testing in a short-duration transonic tunnel requires high accuracy and fast response instruments. Static and total pressure sensors have been refined over the years and are accurate to within 1% or better [24]. Dynamic pressure on the other hand is difficult to measure in a transient environment and has received little attention. The challenge arises from the nature of a blowdown test: the dynamic pressure sensor must be capable of measuring pressure fluctuations on the order of a hundredth of a psi while at the same time surviving a start-up transient of a few milliseconds during which the ambient pressure in the tunnel rises from vacuum to values in excess of 100 psi. A probe designed to overcome the above technical challenge has many applications. Dynamic pressure measurements can be used to infer flow properties such as Mach number, mass flow and efficiency.

This chapter presents research contributing to a series of experiments on a 2:1 pressure ratio turbine stage. The purpose of the testing is to generate high accuracy (less than 1% uncertainty) performance data for the uncooled and cooled version of the turbine stage. As part of this effort, several techniques for measuring mass flow were investigated. The combination of total and dynamic pressure and total temperature measurements was one of the options. The requirements of a dynamic pressure probe, its feasibility and its suitability for the aforementioned applications is discussed below.

2.2 Constraints on Differential Pressure Instrumentation

The design of the differential pressure probe and its feasibility are based on three requirements: accuracy, time response and robustness.

Accuracy

Differential pressure measurements are useful if they can be combined with total pressure and total temperature measurements to infer mass flow and Mach number. The target uncertainty for the mass flow measurements in these experiments is 1% or less. This figure was used as an upper bound in the design of the differential pressure probe. A first order estimate for the accuracy requirement of the differential probe was calculated assuming experimental uncertainty in the total pressure and differential pressure measurements only. The mass flow uncertainty is then given by:

$$\frac{\epsilon_{\dot{m}}}{\dot{m}} = \frac{\sqrt{\left(\frac{\partial \dot{m}}{\partial P_t}\right)^2 \epsilon_{P_t}^2 + \left(\frac{\partial \dot{m}}{\partial \delta P}\right)^2 \epsilon_{\delta P}^2}}{\dot{m}} \tag{2.1}$$

where $\dot{m}$ is defined as in Equation 2.4.

Figure 2-1 is a contour plot of the percentage uncertainty in mass flow as a function of the percentage uncertainty in P_t and δP. The total pressure measurement is expected to be accurate to within 1% (cf. Appendix A). Using a conservative estimate, an uncertainty level of 1% or less for the differential pressure measurements ensures a propagated uncertainty of less than 1% for the inferred mass flow calculations.

Time Response

The second design constraint is the time response of the instrument. A pressure transducer time response of 1 ms is sufficient to track the overall behavior of the flow during the steady operation of the rig. During the start-up transient, however, the probe is subjected to a pressure step and must stabilize quickly in order to accurately measure the flow during the quasi-steady portion of the expansion process. Putting this in perspective with the time scale of the test, the effects of the initial pressure peak on the probe must have decayed in

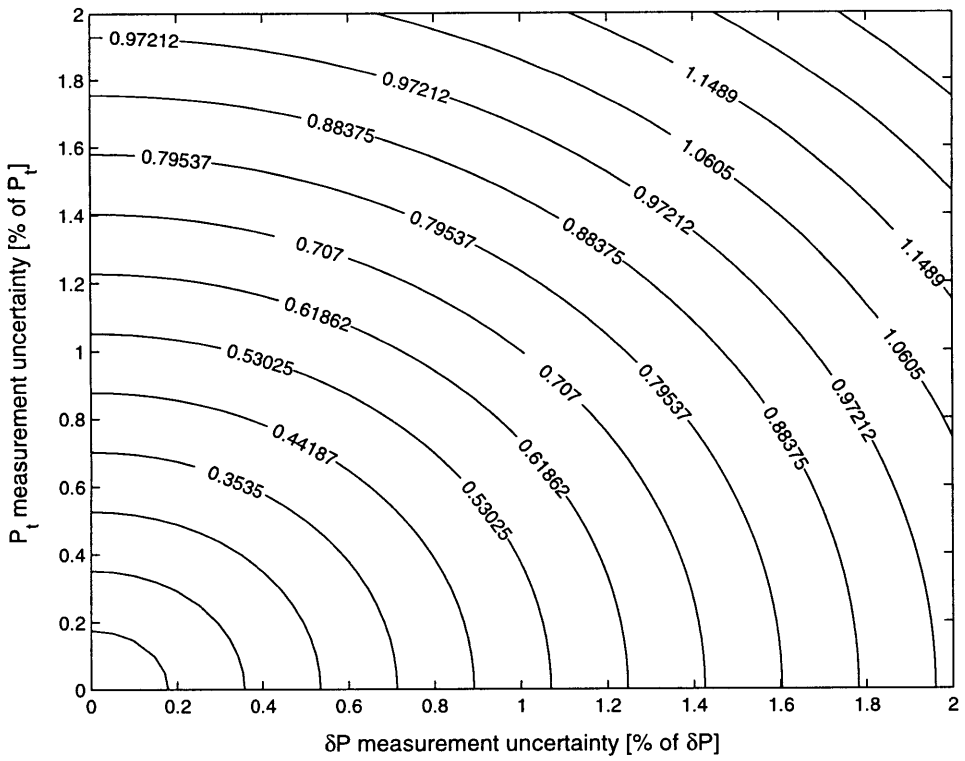

Figure 2-1: Percentage uncertainty in mass flow calculations due to uncertainty in total and differential pressure measurements.

a few dozen milliseconds.

Probe Robustness

The final concern in the design of the dynamic pressure probe is its ability to survive the start-up transient that follows the opening of the fast-acting valve. To estimate the dynamic pressure to which the sensor is subjected during the passage of the expansion wave in the tunnel, a Pitot static probe was connected to a 100 psi differential pressure sensor during a blowdown test at 50 *psi*. The results of the test are presented in Figure 2-2. They show that the differential sensor must survive a few millisecond exposure to a differential pressure on the order of 15 *psi*.

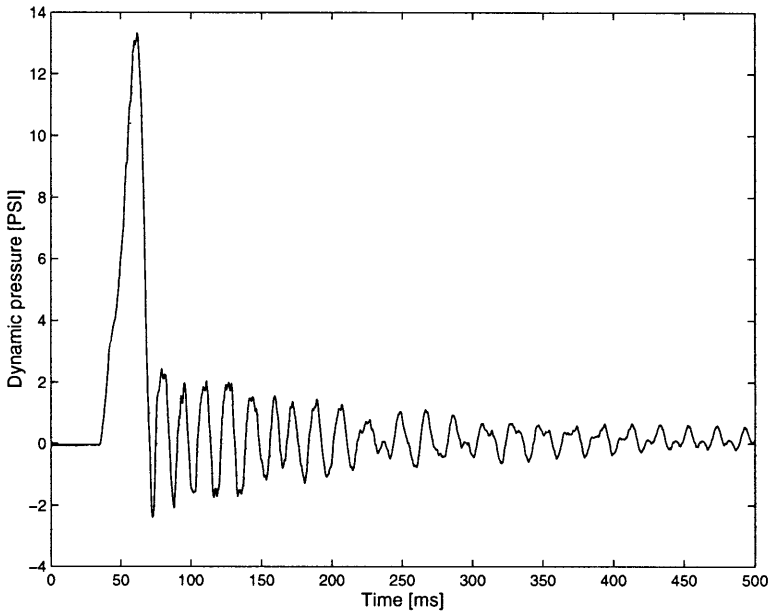

Figure 2-2: Plot of the dynamic pressure during the start-up transient of a test with initial pressure of 50 psi.

2.3 Design of the Differential Pressure Probe

The differential pressure probe was designed based on the three criteria described above. The probe consists of three components: the Pitot static tube, the pressure sensor and the calibration equipment.

Pitot Static Tube

The Pitot static tube was chosen based on its time-response, its accommodation to misalignment with the flow and its size to minimize the disturbances on the downstream flow. A 1/8" diameter United Sensor Pitot-static probe was chosen (cf. Figure 2-6). Empirical tests concluded that a 5^o misalignment contributes to less than 0.5% error in the measurement. The disturbance to the turbine stage inlet flow forty probe diameters downstream are expected to be negligible.

The time response of the tube and its connections to the sensor was calculated based on the work of Grant [19]. For a probe subjected to a step change in pressure, the probe

Sensor	δP	δP calibration	P_t
Manufacturer	*Kulite*	*Setra*	*Kulite*
Model	$XCS-062-5D$	$228-1$	$XCQ-062-100D$
Pressure Range	0 *to* 5 *psi D*	0 *to* 1 *psi D*	0 *to* 100 *psi D*
Maximum overload	15 *psi D*	100 *psi D*	300 *psi D*
Time response	-	40 *ms*	-
Nonlinearity	$\pm 0.5\% FS$	$\pm 0.2\% FS$	$\pm 0.5\% FS$
Hysteresis	0.1% *FS*	0.2% *FS*	0.1% *FS*
Non-repeatability	0.1% *FS*	$\pm 0.2\%$ *FS*	0.1% *FS*
Overall accuracy	$\pm 0.5\% FS$	$\pm 0.25\% FS$	$\pm 0.5\% FS$
Resolution	*Infinite*	*Infinite*	*Infinite*

Table 2.1: Specifications of the pressure sensors.

volume fills exponentially. The time constant for the process is:

$$\tau = \frac{128 \mu L V}{\pi D^4 P} \tag{2.2}$$

where μ is the dynamic viscosity of the fluid, L is the length of the probe, V is its volume, D is the probe head orifice diameter and P is the pressure step.

τ is the time required for 63% of the eventual response to the pressure step to occur. In 5τ, 99.3% of the response is achieved. This corresponds to 11 ms for the present probe design with a pressure step of 70 psi.

Differential Pressure Sensor

The pressure sensor was the most critical component of the design, with the following requirements: small internal volume for fast time response, low measurement uncertainty (1% or less) and high burst pressure (15 psi or higher). The Kulite 5 psi differential pressure sensor was found to be the most suitable candidate. In particular, it remains stable under pressures three times the full scale pressure, which was necessary during the start-up transient. Its characteristics are presented in table 2.1.

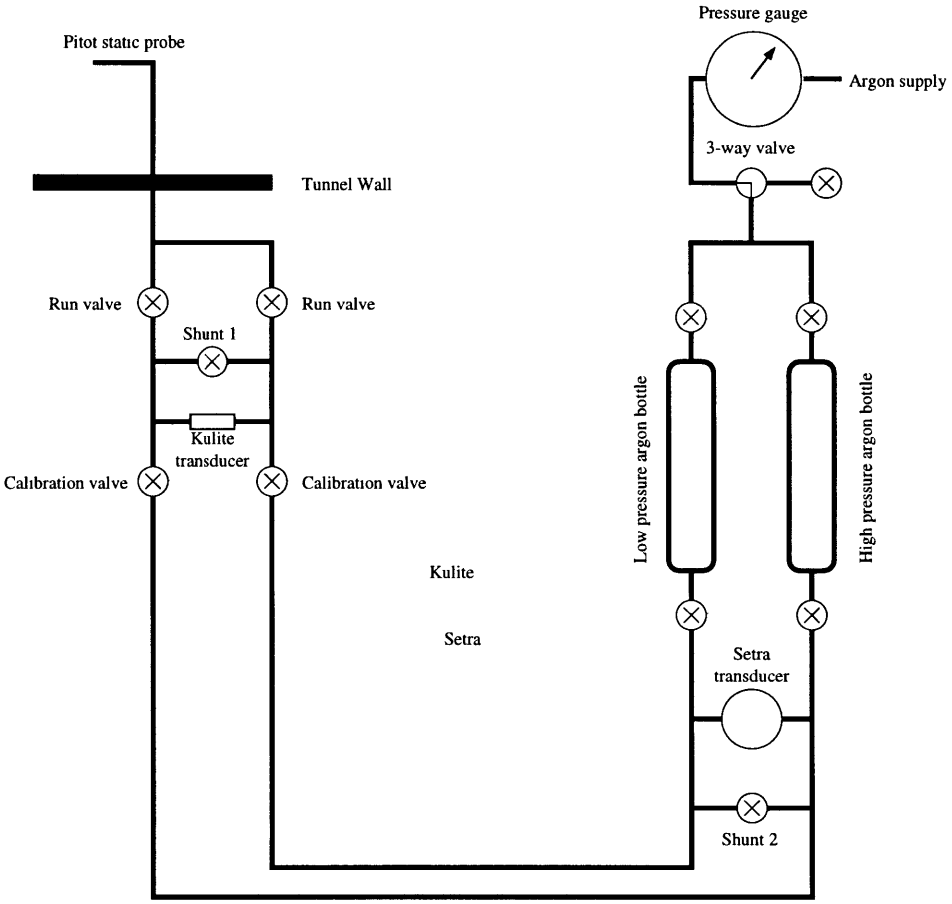

Figure 2-3: Schematic of the dynamic pressure probe (all valves are manual).

Calibration Equipment

To control the Kulite sensor calibration, its gain was monitored before and after each test using a 1 psi differential Setra pressure gauge accurate to $\pm 0.25\%$ of full scale. The accuracy of the calibration was maximized by performing it at the same common mode pressure as during the experimental tests. The specifications of the Setra transducer are presented in Table 2.1.

Figure 2-3 presents the main features of the differential pressure probe calibration set-up. The shunt valves were installed to prevent the differential pressure sensors from being exposed to a pressure above their burst pressure during the manipulation of the system before and after the test.

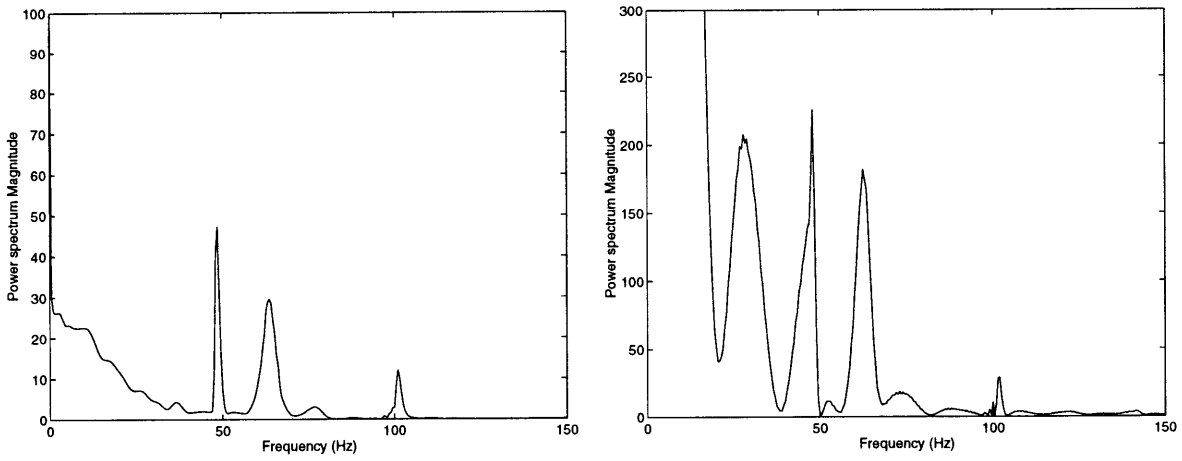

(a) Dynamic pressure signal

(b) Total pressure signal

Figure 2-4: Power spectra of the pressure probe signals upstream of the turbine.

Complete Dynamic Pressure Probe

Several versions of the dynamic pressure probe were tested. The main problem with the measurement was the high level of oscillation in the signal. To determine if this was due to resonance in the cavities of the dynamic pressure probe, the frequency content of the total and dynamic pressure signals were compared (cf. Figure 2-4). Since the dominant frequencies in the signal of the dynamic pressure probe are also present in the signal of the total pressure probe, the vibrations are most likely a consequence of the sudden expansion process at start-up.

To damp out the vibrations, different size expansion chamber silencers were interposed between the Pitot tube and the Kulite sensor (cf. Figure 2-5). Because the orifice of the Pitot tube restricts the mass flow filling up the cavities leading to the Kulite sensor, there is a trade-off between damping the vibrations and decreasing the frequency response of the probe. It was found that the silencer necessary to suppress the dominant 50Hz frequency, decreased the response of the probe to 500 ms during the startup transient. The probe is required to respond in less than 15 ms so the silencer was not used in the final design.

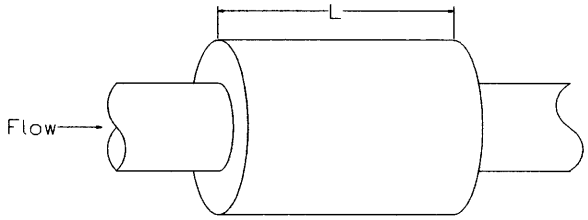

Figure 2-5: Schematic of a single expansion chamber silencer. Maximum damping occurs at frequencies for which $sin\ \omega L/c = \pm 1$. The magnitude of the damping depends on the geometry of the silencer [12].

Mass Flow Probe

To complement the dynamic pressure measurements, a stagnation pressure probe and a stagnation temperature probe were mounted beside the Pitot probe (cf. Figure 2-6). For the total pressure measurements, a 100 psi Kulite sensor was selected and connected to a 1/8" Venturi type Kiel probe (cf. Table 2.1). The mass flow probe is represented inserted in the flow path in Figure 1-2.

The total temperature probes use Omega 0.0005in diameter type K thermocouples located inside an impact probe. Their design was developed by Cai [9] and their uncertainty was demonstrated to be less than 0.05%.

In order to account for circumferential non-uniformities, three sets of probes were used and are referred to as probe A, probe B and probe C, respectively. They were installed 120^o apart and 60^o from the structural struts at the inlet of the contraction. The probe heads were positioned at the annulus centerline.

2.4 Experimental Set-Up

The dynamic pressure instrumentation was developed to serve in the latest application of the blowdown turbine: the measurement of the influence of film-cooling on turbine performance. The facility used is a modified version of that presented in Section 1.4. The operating principles are the same but a Venturi mass flow meter has been added between

the test section and the dump tank. A complete description of the facility can be found in reference [24].

2.5 Calibration Sequence

To ensure the accuracy of the sensor calibrations and, hence of the measurements, all the instruments were calibrated before and after the experimental tests. This procedure was used to monitor the drift of the sensors due to the high pressure expansion wave during the start-up transient and the time stability from test to test. The calibration sequence is described below in detail.

Calibration of the differential pressure probes

Before and after the test, the Kulites were calibrated at the operating common mode pressure . The sensors have a linearity of $\pm 0.5\%$ FS and therefore a 2-point calibration was used between 0 psi differential and a differential of approximately 0.5 psi, the approximate pressure difference during the test. The Setra sensor was used as a reference for the differential pressure calibration.

During calibration, the tunnel is in vacuum for the pre-test calibration and at a pressure of several atmospheres for the post-test calibration. The *run valves* must be closed to isolate the calibration set-up from the run environment (cf. Figure 2-3). All other valves are open, in particular the *shunt 1* and *shunt 2 valves*, whose function it is to protect the Kulite and Setra sensors from pressures above their burst pressure. The calibration system is pressurized to the expected working pressure during the test using the Argon supply. The *high and low pressure bottles* are closed and the *low pressure bottle* is bled to 0.5 psi below the pressure of the *high pressure bottle.* The data acquisition system is triggered. The zero differential of the sensors is monitored for two minutes after which the system is switched to differential mode: the *shunt* valves are closed to isolate the two sides of the Kulite and Setra sensors. The *low* and *high pressure bottles* are opened on the side communicating with the calibration system, yielding a pressure differential across the sensors. The differential is monitored for two minutes after which the system is brought back to zero differential by

opening the *shunt valves* and recording the sensor output for two more minutes.

Calibration of the total pressure probes

The total pressure sensors are also calibrated before and after the test. A pressure differential is applied between the reference pressure side of the Kulites and the sensing side, monitoring the tunnel conditions. For the pre-test calibration, the tunnel is in vacuum. The post-test calibration is performed after the tunnel has reached equilibrium. The calibration is executed by switching the reference pressure between atmosphere and vacuum. Since the pressure sensors are linear, a two point calibration is used to transform the voltage output of the sensors into engineering units.

Calibration of the total temperature probes

The total temperature sensors are calibrated in an oil bath monitored by NIST-traceable instruments. A fifth order polynomial is fitted through the multi-point calibration to yield an uncertainty of less than 0.05%. The calibration procedure is described in detail in reference [9].

2.6 Applications of Dynamic Pressure Measurements

Dynamic pressure measurements are valuable because in conjunction with stagnation pressure and temperature measurements, they are used to calculate the Mach number and mass flow properties of the flow. These quantities in turn can be applied to inferring the mechanical efficiency of the turbine stage under study. The details of these calculations are presented below.

Mach Number Calculations

The Mach number, M, in the contraction upstream of the turbine stage can be calculated from the compressible flow equations:

$$M = \sqrt{\frac{2}{\gamma - 1} \cdot \left[\left(\frac{P_t}{P_t - \delta P} \right)^{\frac{\gamma - 1}{\gamma}} - 1 \right]} \tag{2.3}$$

where P_t is the stagnation pressure, δP is the dynamic pressure and γ is the ratio of specific heats.

Mass flow Calculations

The mass flow, $\dot{m}$, through the turbine facility can also be inferred using the compressible flow equations and the measurements at the upstream contraction:

$$\dot{m} = \frac{A_{eff} P_t}{\sqrt{T_t}} \cdot \frac{\sqrt{\frac{\gamma}{R}} M}{\left(1 + \frac{\gamma - 1}{2} M^2\right)^{\frac{\gamma + 1}{2(\gamma - 1)}}} \tag{2.4}$$

where A_{eff} is the effective area in the plane of the dynamic pressure probe in the upstream contraction and the other variables are as defined above.

Efficiency Calculations

The latest research efforts in the Blowdown Turbine Facility have been in the measurement of turbine performance in a blowdown environment. The measurement of thermodynamic efficiency was investigated by Cai [9] and the measurement of shaft efficiency by Keogh [24]. The latter is based on the measurement of the mass flow through the turbine and the torque on the turbine shaft. It is defined as the ratio of the actual power to the ideal power extracted from the turbine and, in its ideal gas form, can be expressed as:

$$\eta_s = \frac{\tau \cdot \omega}{\dot{m} C_p T_{t4} \left(1 - \pi^{\frac{\gamma - 1}{\gamma}}\right)} \tag{2.5}$$

where τ, ω, T_{t4}, π, and C_p are the torque, angular speed, turbine inlet stagnation temperature, turbine pressure ratio and specific heat capacity, respectively.

2.7 Validation of Experimental Procedure

The prime goal of the experiments on the ground based turbine stage was to accurately measure aerodynamic performance. The biggest challenge in achieving this goal was obtaining accurate mass flow measurements. This problem was studied at length by Keogh [24]. The most reliable mass flow measurement technique is to use a Venturi nozzle calibrated against NIST standards between the choking plate and the dump tank. This method gives results accurate to within $\pm 0.25\%$. The technical difficulty, however is that the flow through the Venturi is only a fraction of the flow through the turbine. The total mass flow is a combination of the primary flow going through the Venturi nozzle, and the secondary flow leaking into adjacent cavities. Hence, at any moment of time, the mass flow rate through the turbine may not match the mass flow rate through the Venturi nozzle. The relationship between the turbine and nozzle mass flows can be described as;

$$\dot{m}_{Turbine} = \dot{m}_{Nozzle} + \dot{m}_{Stored} \tag{2.6}$$

A transient correction was derived to account for the mass flow stored in the cavities. The description of the model can be found in reference [24].

The mass flow measured using the mass flow probe described in this chapter is the actual mass flow through the turbine. Hence, this measurement can be used to validate the transient correction used with the Venturi nozzle to account for the stored mass flow. In Equation 2.4, all the variables but the effective area can be calculated. The best validation available, then, is verifying the decay of the mass flow rate. If A_{eff} in Equation 2.4 is replaced by 1, and the calculated $\dot{m}$ is a fraction of the Venturi mass flow measurement, then the ratio is an estimate of the effective area in the plane of the probes.

Test	*Pressure*	Re_{avg}	M_A	M_B	M_C
030	32 *psi*	9.38×10^5	0.088	0.089	–
036	104.5 *psi*	2.28×10^6	0.083	–	–
037	104.5 *psi*	2.25×10^6	0.081	–	–
038	94.7 *psi*	2.35×10^6	0.085	–	–
039	100.4 *psi*	2.37×10^6	0.082	–	–
040	104.5 *psi*	2.26×10^6	0.082	–	–

Table 2.2: Average Mach number measurements (*Pressure* is the initial supply tank pressure and Re_{avg} is the Reynolds number averaged over the usable duration of the test - 500 to 1000ms - cf. Footnote 1).

2.8 Results

Experimental measurements

During each test, the mass flow probe sensors measure three flow properties - total and dynamic pressure and total temperature - at three equispaced locations around the annulus. Figure 2-8 presents typical traces for total and dynamic pressure and total temperature. For most tests, the usable time is from 500 ms to 1000 ms. Since the measurements of the probe are used to track the overall behavior of the blowdown process and not small time scale unsteadiness, the signals are curve fitted using a second order polynomial and used to infer Mach number and mass flow. For the results below, measurements from Probes A & B are available only, as Probe C and later Probe B were damaged during high pressure testing.

Mach Number

The average Mach number during the quasi-steady portion of the test (500-1000 ms) for different test conditions is summarized in Table 2.2. The Mach number is higher for lower Reynolds numbers, as thicker boundary layers are responsible for higher flow speeds in the core.

The Mach number history for low and high pressure tests is presented in Figure 2-9. For low pressure test 030, measurements from probe A and B agree to within 1% and the Mach number magnitude varies by less than 1% throughout the usable part of the test during

which the throttle plates are choked. For the high pressure tests, the Mach number increase with time by as much as 2%.

Under theoretical conditions, the Mach number should remain constant so long as the inlet guide vanes are choked. During a blowdown test, several factors can cause the Mach number to change slightly with time:

1. During a test, the inlet pressure and temperature decay, causing the Reynolds number[1] to decrease by 10 to 15% in a 500 ms time span. Theoretically, the decrease in Reynolds number causes boundary layers to grow and the core flow Mach number to increase. The sensitivity of the Mach number to Reynolds number changes was evaluated by running a 2-D coupled viscous/inviscid model (UNSFLO, cf. Chapter 4) of the stage flow for conditions corresponding to $t = 500\ ms$ and $t = 1000\ ms$ and for the low and high pressure tests. The Mach number upstream of the NGV changed by less than 0.1% for both the high and low pressure cases. Although these figures are expected to underestimate the effects of Reynolds number change as the 2D model does not account for the endwall boundary layers, it can be concluded that Reynolds number effects play a minor role in the variation of core flow Mach number.

2. As the tunnel walls heat up to gas temperature, the boundary layer stabilizing effect of the cold wall vanishes [26]. The boundary layer thickness increases, enhancing the effect of increasing Reynolds number mentioned above. This factor is accounted for in the numerical simulation described above.

3. The recovery factor of the pressure probes changes with Reynolds number. However, this effect was found to be negligible from empirical testing by the Pitot static probe manufacturer.

4. The response of the Kulite pressure sensors is temperature dependent. Their measurement is expected to drift as they heat up to gas temperature.

5. The curvature of the Mach number trace might be an artifact of the curve fitting of the experimental data.

[1]The Reynolds number is defined as: $Re = \frac{P_t M D \sqrt{\gamma}}{\sqrt{R T_t}\mu}$, where M is the local Mach number and D is the inner annulus diameter.

Test	*Pressure*	Re_{avg}	$\frac{A_{eff_A}}{A}$	$\frac{A_{eff_B}}{A}$	$\frac{A_{eff_C}}{A}$
030	32 *psi*	9.38×10^5	0.808	0.797	–
036	104.5 *psi*	2.28×10^6	0.854	–	–
037	104.5 *psi*	2.25×10^6	0.859	–	–
038	94.7 *psi*	2.35×10^6	0.825	–	–
039	100.4 *psi*	2.37×10^6	0.856	–	–
040	104.5 *psi*	2.26×10^6	0.863	–	–

Table 2.3: Ratio of the inferred effective area to the geometric area in the plane of the mass flow probe.

Mass Flow

$\dot{m}/A_{eff}$ was computed from the mass flow probe data. Mass flow was also predicted by Keogh [24] using Venturi nozzle measurements. Since A_{eff} is unknown, it was derived by taking the fraction of $\dot{m}_{Venturi\ corrected}$ by $(\dot{m}/A_{eff})_{Mass\ flow\ probe}$. Figure 2-7 shows mass flow as predicted by the correction of the Venturi measurements and by the mass flow probes. The calculations agree to within 1% for the entire usable span of the data. The agreement between Probe A and B is better than 1% for the shape of the curve and 1% for the calculation of A_{eff}.

Table 2.3 presents calculations of the effective area for different test conditions. The results agree with theoretical expectations: the effective area increases with Reynolds number as boundary layers thin out when the flow becomes less viscous. Successive tests at the same test conditions yield effective areas agreeing to within less than 0.5%. The agreement can also be observed by comparing the corrected mass flow time history of tests with similar conditions (cf. Figure 2-10).

2.9 Chapter Summary

The concept of a dynamic pressure probe was presented, along with its applications to calculating Mach number and mass flow. Several conclusions and recommendations are available at this point of the instrument development.

1. It is possible to build a 1% accurate dynamic pressure probe and to use it to calculate mass flow with 1% uncertainty.

2. The oscillations generated by the start-up transient are a major limitation on the quality of the signal as their amplitude is of the same order as the differential pressure being measured. Further investigation in the origin of the oscillations would help to determine if the oscillations can be filtered out or if they have important physical relevance.

3. The 5 psi Kulite sensors used did not survive successive rounds of high pressure testing as the start-up transient generated differential pressures in excess of 15 psi, the burst pressure of the instrument. For subsequent high pressure tests, a more rugged sensor should be utilized.

4. The mass flow calculated using the mass flow probe data decayed at the same rate as the mass flow calculated using the corrected Venturi nozzle measurement. Hence, the theoretical correction derived by Keogh [24] correctly predicts the dynamics of the tunnel.

5. The original goal for this research was for the three probe combination to serve as a stand alone mass flow measuring device. In order to do so, a correlation of Reynolds number and effective area is necessary. This can be achieved using the Venturi nozzle measurements as a reference. Such a correlation should be compared with results from theoretical modeling of the inlet flow.

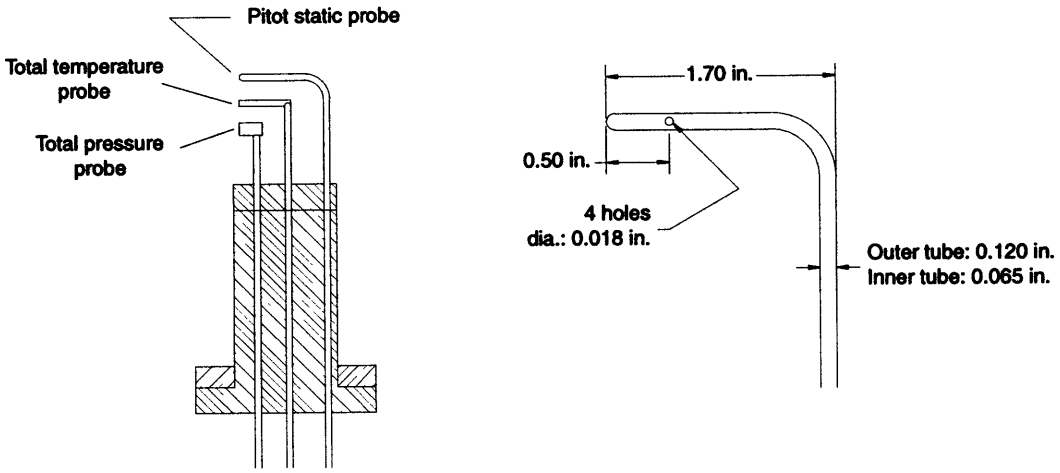

Figure 2-6: Schematic of the mass flow probe and dimensions of the Pitot tube.

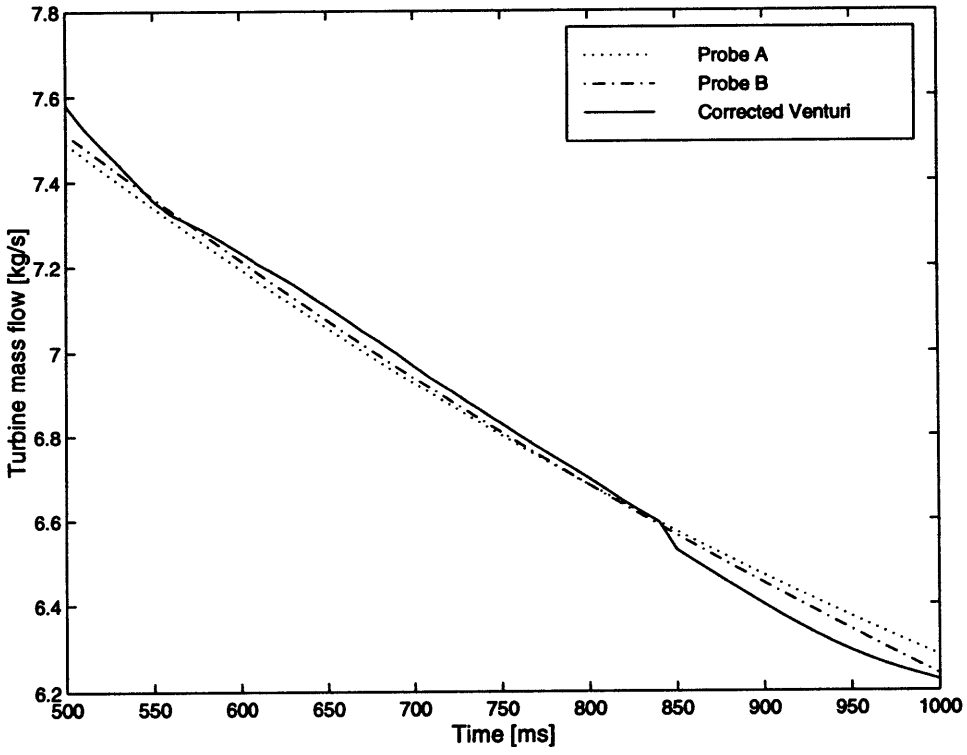

Figure 2-7: Turbine mass flow as a function of time (Test 030).

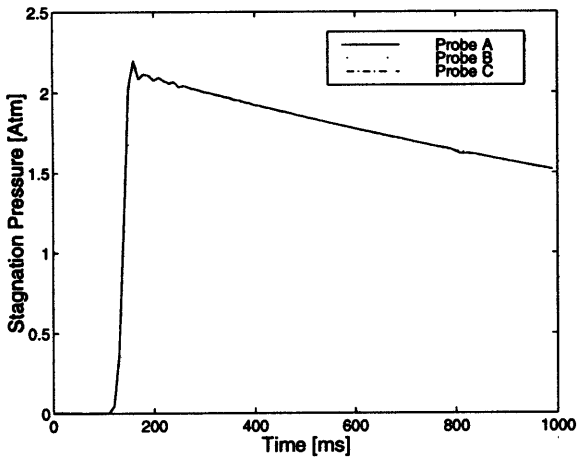

(a) Total pressure probes

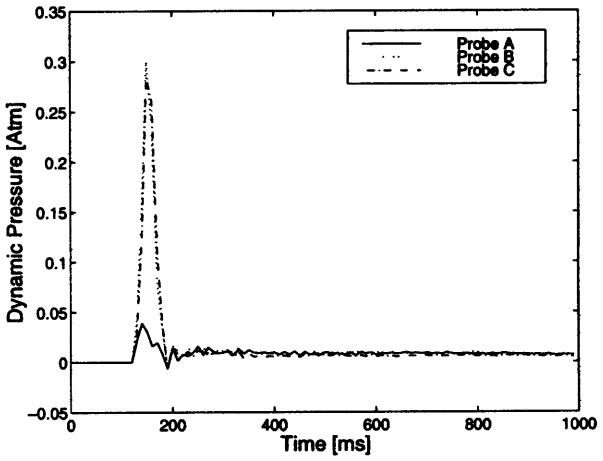

(b) Dynamic pressure probes

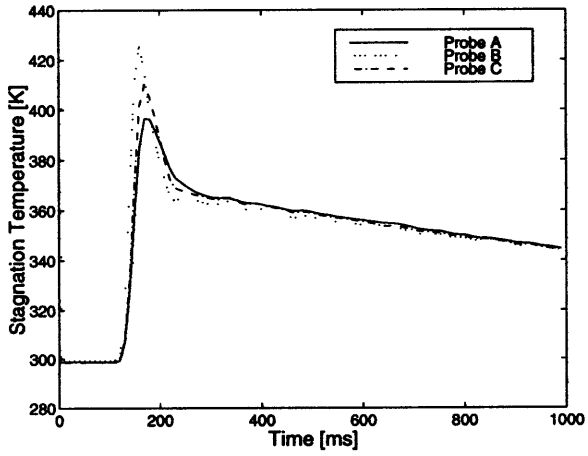

(c) Total temperature probes

Figure 2-8: Mass flow probe pressure and temperature signals.

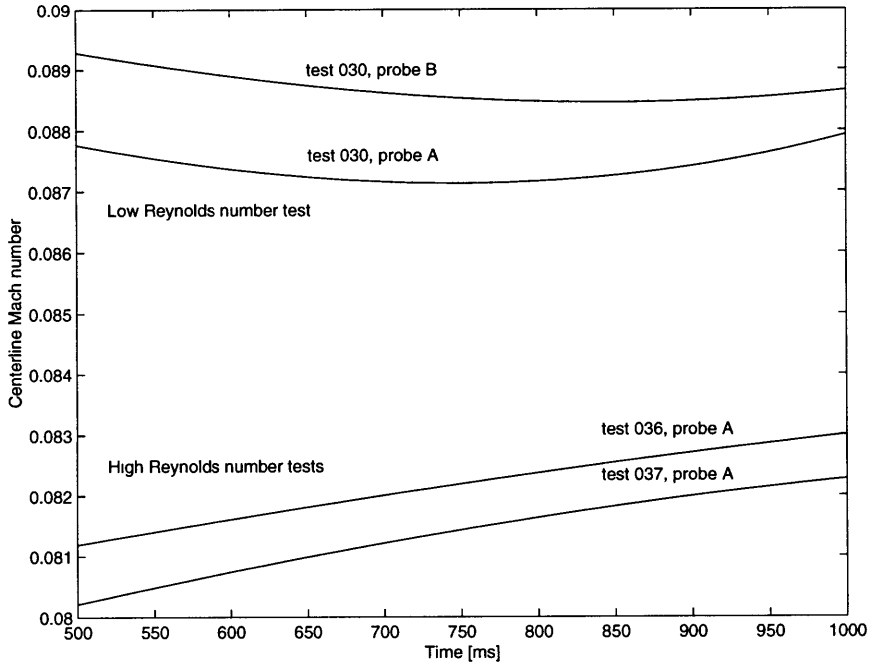

Figure 2-9: Time history of Mach number for low and high Reynolds number tests.

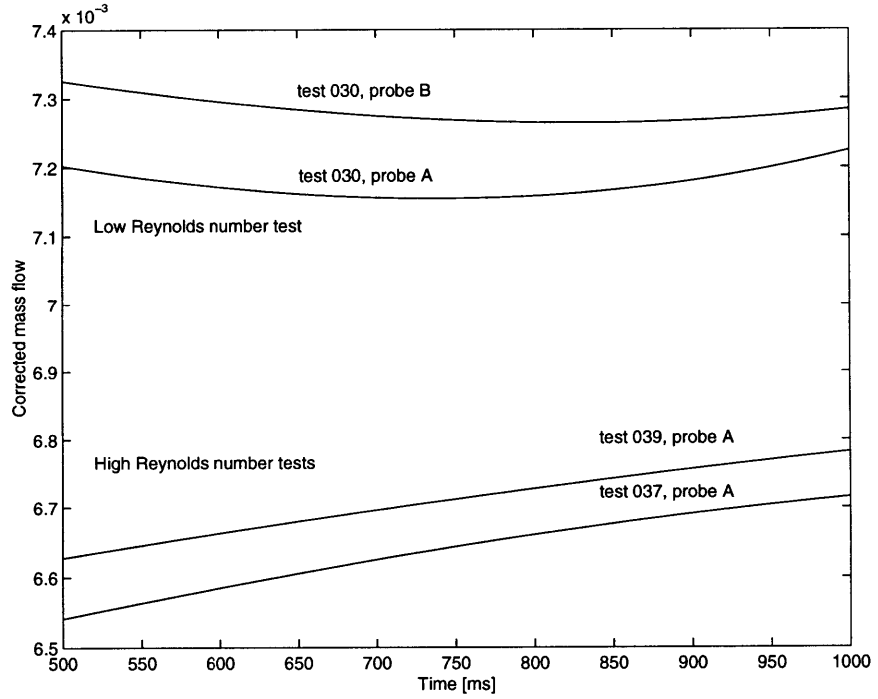

Figure 2-10: Time history of corrected mass flow for low and high Reynolds number tests.

Chapter 3

Non-Intrusive Study of Turbine Flow: Particle Image Velocimetry

3.1 Introduction

In the last two decades, flow visualization techniques for unsteady flows have been constantly improved. Particle Image Velocimetry (PIV) is the latest method used in this field of research and generates instantaneous velocity fields by non-intrusive means. It has been tested extensively for the visualization of simple cases such as the flow around cylinders. It is only recently that the technique has been applied to more complex cases such as turbomachinery flows. Several research groups have reported PIV results in cascade experiments [18]. This chapter presents the results of one of the first attempts at applying PIV in fully scaled rotating turbomachinery[1].

The application of PIV to turbomachinery presents several challenges. First, installing the required instrumentation inside a turbine stage is a complex process. Second, the application of PIV to transonic flows is difficult because high accelerations are present in the flow and the experiment must be designed so that the seeding particles accurately follow the flow to capture these changes. The trade-offs involved are described below and

[1]To the best knowledge of the author, the only other successful applications of PIV in a rotating turbomachinery stage were by Wernet in a transonic axial compressor [28] and by Bryanston-Cross in a transonic turbine stage [10].

are complemented with the results of the experiment.

3.2 Flow Visualization using Particle Image Velocimetry

The latest innovations in the field of experimental fluid flow visualization have been the successful applications of particle-image velocimetry to unsteady flows. This particle-imaging method belongs to a broader class of velocity-measuring techniques, known under the common name of Pulsed Light Velocimetry (PLV). The author refers the reader to a review article by Adrian [3] for an excellent discussion of the subtleties of pulsed-light velocimetry and more specifically particle-image velocimetry. The following description is a brief introduction to the topic and should allow the reader to understand some of the issues and trade-offs present in the experimental application of PIV.

3.2.1 Pulsed-Light Velocimetry

The different techniques, grouped under the name of pulsed-light velocimetry, consist in tracking the displacement of discrete markers present in the flow. By monitoring the position of the markers over different, known, time intervals, the local velocity, $\vec{V}$, of the marker can be calculated as:

$$\vec{V}(\vec{x},t) = \frac{\Delta\vec{s}(\vec{x},t)}{\Delta t} \tag{3.1}$$

where $\Delta\vec{s}$ is the displacement of the marker located at $\vec{x}$ at time t, during the time interval Δt separating successive observations of the markers.

The different PLV methods are characterized by the properties of the markers used. Solid particles in gases and liquids have been used as well as gaseous bubbles in liquids and liquid droplets in gases. On a smaller scale, molecules have also served as markers. In all cases however, PLV consists in repeatedly illuminating the flow and recording the image of the markers using an optical device.

3.2.2 Particle-Image Velocimetry

Particle-Image Velocimetry distinguishes itself from other PLV techniques in that the markers are particles that are statistically always individually distinguishable. In other words, the density of the particles is small enough that the distance between them guarantees an individual image for each marker on the imaging medium.

Before going into the details of PIV image processing, it is useful to look at the technical implementation of the method. Although three dimensional PIV has been successfully demonstrated [21], this research will deal only with the two-dimensional application. The general principles of two-dimensional PIV are as follows: the flow to be studied is seeded with particles of appropriate properties (cf. Section 3.3.3); a light sheet is pulsed in the plane of interest; the illuminated particles scatter light back into an optical system oriented perpendicular to the sheet; the plane of focus of the optical system coincides with the plane of the light sheet and the image is recorded on a optical recording medium.

The two most popular recording medium are photographic film and digital camera imaging system. The digital system is more practical than the photographic film as its data can be transferred to a computer for automatic post-processing. However, digital imaging technology is not advanced enough to be applied to all PIV applications. Three factors prevent this leap. First, digital cameras do not yet offer the same resolution as photographic film. A typical digital camera consists of an array of 1000×1000 pixels. The region of interest must therefore be small enough so that the particles correspond to at least the size of a pixel. Second, image files are very big and today's computer systems cannot always handle the rapid inflow of data necessary for high speed digital imaging. Finally, the frame acquisition speed must be fast, so that the particle displacement between successive frames can be assumed to be linear. For high speed flow applications, which require a very small Δt between frames, the best digital cameras are still too slow and high speed photographic cameras must be used.

Particle image velocimetry was differentiated above from other techniques of pulsed-light velocimetry by the low probability that separate particles will overlap on the image. Within this range of conditions lie two extremes, low-density PIV or Particle-Tracking Velocimetry (PTV) and high-density PIV.

In particle-tracking velocimetry, the distance traveled by a particle between two successive light pulses is small compared with the mean distance between adjacent particles. The velocity field is obtained by tracking the displacement of individual particles.

In high-density PIV, the density of particles is high enough that the displacement of individual particles between successive light flashes is larger than the mean distance between adjacent particles, but not so much that two particles overlap in the image. Tracking each particle would be time consuming due to their number and ambiguous due to the proximity of the particles. Instead of following individual markers, the displacement of small groups of particles is measured. The use of high-density PIV is tied to advanced image processing algorithms using cross-correlation or auto-correlation to track the displacement of the groups of markers. Adrian provides a detailed explanation of the procedure [3]. This method is a good complement to CFD: its output is a velocity field on a structured grid as opposed to a solution made up of randomly located velocity vectors for particle tracking velocimetry. The drawback, however, is that the scale of the observable flow phenomena is limited, as in CFD, by the size of the interrogation cells over which the correlation is executed.

The time interval between successive frames is an additional constraint in the application of PIV. In many engineering flows, the time interval necessary to calculate an approximately instantaneous velocity of the particles is small compared to the acquisition speed of the best digital imaging systems. In most turbomachinery applications, for example, the flow is transonic, and images corresponding to successive light flashes cannot be recorded on different frames. Instead, two or more images are superimposed on a single imaging medium. Although in theory this is not a problem for either of the high- or low-density methods, it brings about some ambiguities in the analysis. For example, it can be difficult to distinguish the particles of the first light flash from those of the second light flash. This can affect the accuracy of the solution. In particle-tracking velocimetry, the particles at different instants of times can be mistaken as being adjacent particles. The direction of velocity can also be ambiguous, as particles from successive instants in time can be identified in space but not in time. Adrian [3] explores several options to alleviate this problem, including using different colors of light pulses on color photographic paper.

In the experiment presented herein, photographic film was chosen as the imaging medium for double exposure low-density PIV. This decision was driven by two factors: (1) for tran-

Parameters	Full Scale Engine	MIT BDT
Working Fluid	*Air*	$Argon - CO_2$
Ratio of Specific Heats, γ	1.28	1.28
Mean Metal Temperature	1118 K	295 K (*room temp.*)
Gas/Metal Temp. Ratio	1.59	1.59
Inlet Total Temperature	1780 K	478 K
Inlet Total Pressure	19.6 atm	4.3 atm
Exit Total Pressure	4.5 atm	1.0 atm
Reynolds Number	2.7×10^6	2.7×10^6
Design Rotor Speed	12,734 rpm	6190 rpm
Design Mass Flow	49 kg/s	17 kg/s
Midspan Axial NGV Chord	0.080 m	0.059 m
Midspan Axial Rotor Chord	0.035 m	0.026 m
Interblade Row Axial Gap	0.015 m	0.011 m
NGV Inlet Angle (from Axial)	0^o	0^o
NGV Exit Angle	74^o	74^o
Rotor Inlet Angle	57^o	57^o
Rotor Exit Angle	-65^o	-65^o

Table 3.1: MIT Blowdown Turbine scaling for the ACE turbine stage at design point.

sonic turbomachinery applications, successive frames must be captured within milliseconds of each other; (2) the size of the region of interest was relatively large and necessitated high resolution .

3.3 Experimental Set-Up

The PIV experiments were conducted in the Blowdown Turbine Facility at the MIT Gas Turbine Laboratory. The apparatus was set-up by Bryanston-Cross and D'Hoop [11] and the data analyzed herein was acquired during the summer of 1996 by Guenette, Bryanston-Cross, Keogh and Cai and is believed to be the first successful application of PIV in a turbomachinery stage under engine conditions.

3.3.1 Test Facility

The general characteristics of the facility were presented in Chapter 1. The reader can consult [14] and [20] for a more detailed description. The Blowdown Turbine Facility was modified to accommodate the PIV instrumentation system. An optical path inside

the casing, a light source and a seeding source all had to be added to the facility. The modifications to the Blowdown Turbine Facility for the PIV experiments are discussed in great length in references [11] and [8]. The experiments were conducted on a scaled version of the Rolls-Royce ACE turbine stage. The characteristics of the rig and the scaling parameters can be found in Table 3.1.

3.3.2 Optical System

One of the metallic windows at the axial position of the rotor was replaced by a ground and polished glass window, which was designed to minimize optical distortion. Two optical periscopic probes located upstream of the stator and downstream of the rotor projected two complementary light sheets (each 2 mm in thickness and 20 mm in width) into the turbine stage. One of the metallic stators was replaced by a copy made out of transparent polished acrylic to create an unobstructed light path for the upstream light probe. The rotors were coated with black paint to minimize reflection of the laser light on the blade surface.

The light sheet was generated by a Spectra Physics GCR Series Nd-YAG double pulsed, Q-switched laser, specifically designed for PIV applications. It generated a visible 532nm wavelength green beam and was pulsed at a repetition rate of 15Hz during the PIV experiments. The two pulses, necessary for double exposure of each PIV picture, were separated by 0.6, 0.8 or 1.0 μs and were characterized by a 10 ns width at an energy level of approximately 100 mJ.

The imaging system was placed at a distance of 0.5 m in front of the transparent window and perpendicular to the light sheet (cf. Figure 3-5). It consisted of a high speed Hulcher sequence camera, fitted with an Olympus 90 mm macrolens and synchronized with the laser. Kodak Tmax 3200 film was chosen for its high resolution (100 line-pairs/mm) and high sensitivity (3200-50000 ASA).

3.3.3 Particle Seeding

Particle seeding is critical in the application of particle image velocimetry. The choice of seeding material is constrained by two contradicting factors. On one hand, particles must

Name	Styrene
Systematic name	Vinylbenzene
Molecular formula	C_8H_8
Molecular weight	104.15 kg/kmol
Melting point	-31^oC
Boiling point	145^oC
Density at 25°C	900.1 kg/m^3

Table 3.2: Seed particle properties in the PIV experiments.

be as large as possible to maximize signal strength in the image. On the other hand, they must be neutrally buoyant in the fluid and small enough so that they follow the flow path in regions of high acceleration [3]. Styrene was selected as the seed material for this experiment. It is a convenient source of low-density mono-dispersed particles of spherical shape (cf. Table 3.2). The temperature tolerance of styrene (up to 100 degree C) and its scattering properties for the Nd-YAG laser light were adequate. Based on a study by Bryanston-Cross and Epstein [7], a mean particle diameter of 500 nm with a standard deviation of 100 nm was selected, at a concentration of one particle/mm^3 in the supply tank. The particles were injected in the supply tank using a TSI model 9306 six-jet atomiser and the seed concentration was monitored using a laser particle counter.

3.4 Image Processing Algorithm

This section describes the steps required to reduce the PIV pictures from the exposed photographic film to the velocity flow field. The image processing algorithm is illustrated in Figure 3-4.

3.4.1 Digitized PIV Images

The photographic film from the PIV experiment was developed and the pictures were digitized in Kodak PCD format. The resolution of the pictures is 2048 × 3072 pixels in digital format. Given that the field of the picture is approximately 36 × 54 mm^2, one square pixel represents a square of roughly 17.5 × 17.5 μm^2. The pictures were then converted into GIF format before being processed on a UNIX workstation using Matlab and the Matlab Image

Processing Toolbox.

The final step of the pre-processing procedure was to divide the pictures in four quarters. When uncompressed, an entire picture was too large to be processed by a single workstation despite the several hundred megabytes of RAM available. Also, dividing the pictures offered better resolution of individual features on the computer screen.

3.4.2 Autocorrelation

In the steps described below, the method of autocorrelation is used to evaluate the distance between points on a digital image. Following is a brief explanation of the method [3].

A digital picture is defined by a map of the intensity of each pixel, $\mathbf{I}(\mathbf{X})$, at location $\mathbf{X}$. Autocorrelation consists in taking a small interrogation spot on the picture and displacing it by a small amount, $\mathbf{s}$. Integrating the product of the two intensity maps over the interrogation spot gives the autocorrelation for a displacement of $\mathbf{s}$:

$$R(\mathbf{s}) = \int_{spot} \mathbf{I}(\mathbf{X})\mathbf{I}(\mathbf{X}+\mathbf{s})d\mathbf{X} \tag{3.2}$$

Repeating the procedure for the area surrounding the initial interrogation spot gives a map of autocorrelation. If the area contains two similar features such as the image of a particle at time t and time $t+\Delta t$, the correlation map will be characterized by two peaks: the tallest one is the autocorrelation of the interrogation spot containing the particle at time t onto itself when $\mathbf{s} = \mathbf{0}$, the other one is the autocorrelation of the interrogation spot containing the particle at time t with the spot containing the particle at time $t + \Delta t$. The magnitude of $\mathbf{s}$ is the distance between the two peaks and represents the displacement of the particle between two laser flashes.

3.4.3 Image Calibration

The digital pictures were calibrated to obtain the first order magnification factor of the images and to quantify the second order pin-cushioning distortions. The rotor passage was photographed under the same conditions as for PIV with a grid positioned in the plane of the laser light sheet (cf. Figure 3-1). The reference grid was a section of graph paper with 20

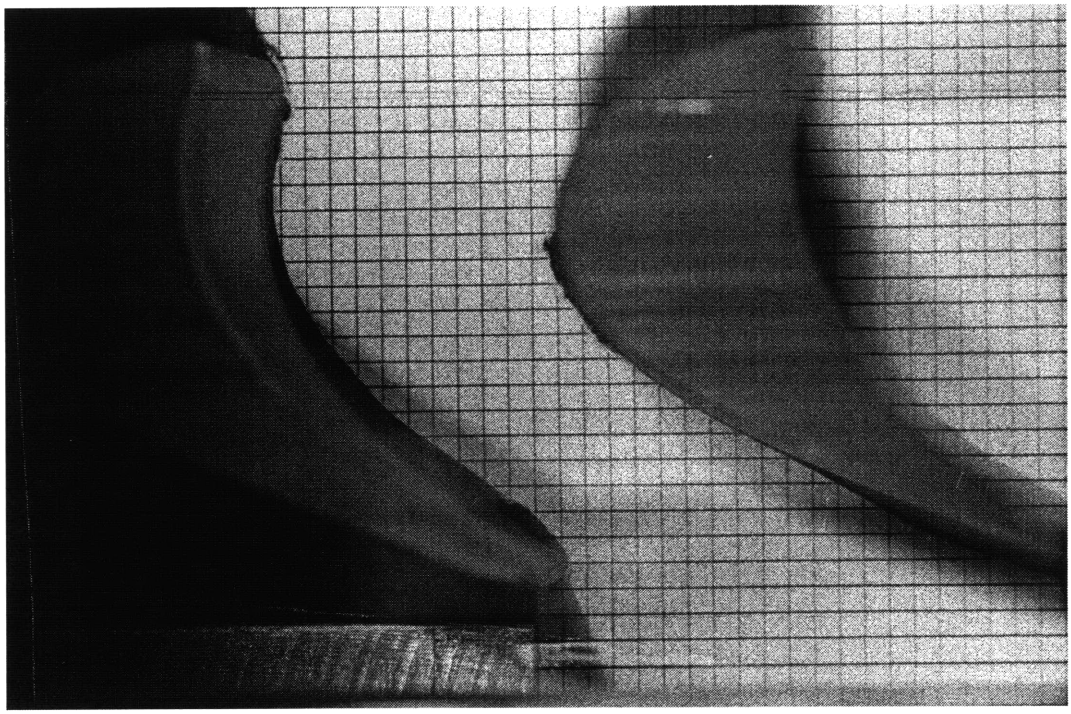

Figure 3-1: Digitized image of the PIV calibration grid.

lines per inch. For different pictures, the distance between several hundred intersections of the vertical and horizontal lines was measured by correlating neighboring intersections onto each other. The results yielded a distribution of the scaling factor between full size and the digital image at different locations on the frame. The mean and standard deviation of the distribution were $17.58 \mu m/pi.$ and $0.19 \mu m/pi.$ respectively in the circumferential direction and $17.10 \mu m/pi.$ and $0.14 \mu m/pi.$ in the axial direction. For the analysis of the PIV data, the axial and circumferential distortions were assumed to be uniform over an entire picture and the scaling factors above were used to transform pixel-based units into metric units. Appendix B treats the problem of the errors associated with this assumption.

3.4.4 Generation of the Velocity Flow field

The transformation of the GIF files into a velocity field was the most demanding part of the processing procedure. It was conducted in three steps: the identification of particles, the identification of particle pairs and the inference of the velocity vectors. The code used for these tasks was a modification of a program developed by Bons [6].

The identification of the particles was the most difficult step to program. Finding

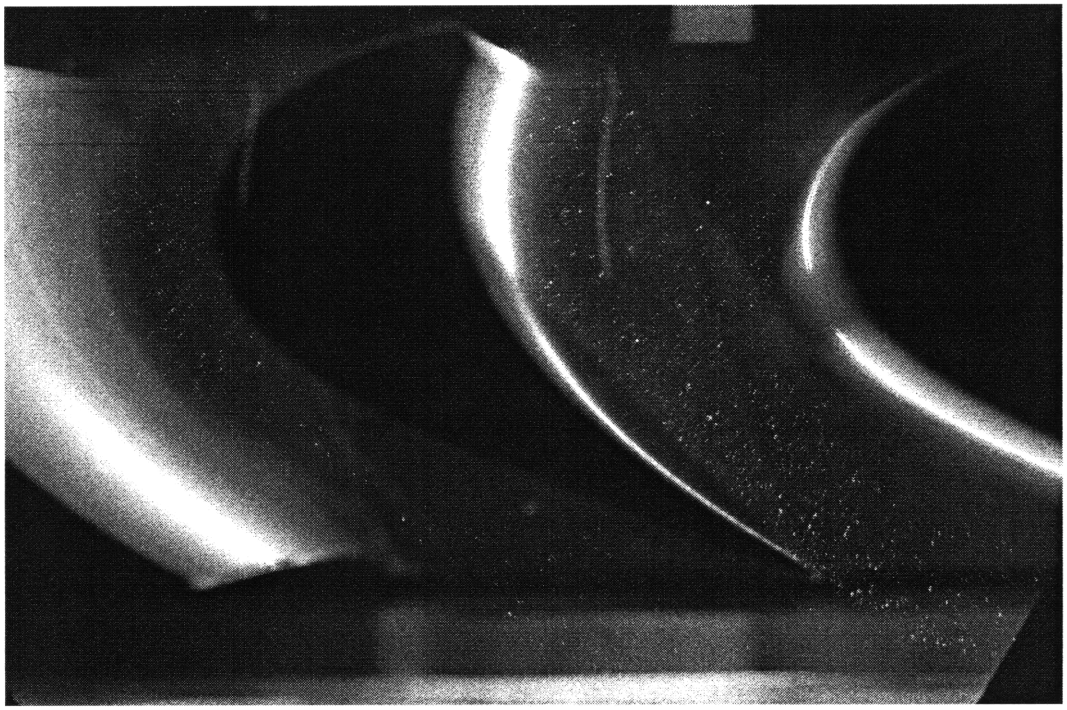

Figure 3-2: Digitized PIV picture.

particles in a picture is done using a recognition algorithm based on the brightness and distribution of the pixels. Since the image of a particle is a group of very bright pixels, the image can be searched for features satisfying this description. In theory, this should be trivial because the particles are easily distinguishable on the PIV pictures (cf. Figure 3-3). Unfortunately, the reflection of the laser light sheet on the blade surface created regions of glare in the neighborhood of the blades which confused the image recognition program (cf. Figure 3-2).

One solution to this problem was to digitally enhance the pictures before processing them. The regions of glare were removed from the pictures and the contrast was increased in the rotor passage. The solution was not optimum, however, as data was lost in the process. Instead, the image recognition software was tuned to improve the quality of the results. The particles were first selected using a sorting algorithm that identified the brightest pixels and determined if the distribution of the light intensity for surrounding pixels constituted a particle. Several selection criteria were set such as the minimum brightness of the pixel, the gradients of intensity around it and finally the size of the identified particle. The criteria were set empirically by observing the properties of typical particles. After this step, it was

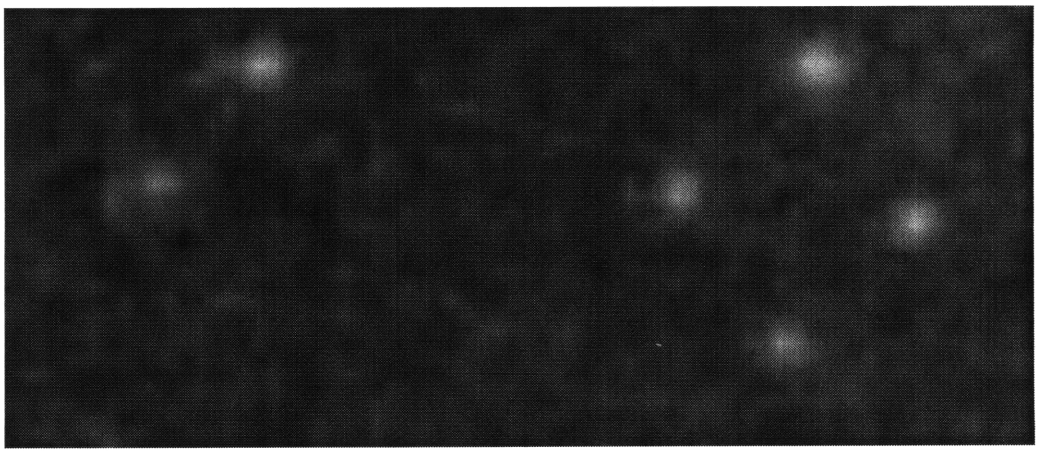

Figure 3-3: Detail of a PIV picture showing three particle pairs.

possible to manually remove or add particles by selecting them with the mouse.

The next step was to pair up particles. Pairs were identified by process of elimination using selection criteria based on the knowledge of the flow. However, since the seeding density was very low, these constraints were not rigorously applied and the pairing was rarely ambiguous (cf. Figure 3-3). Sometimes, the algorithm was unable to identify the pairs, in which case they could be added manually.

Finally, the velocity vectors were computed for each pair of particles. To reduce the uncertainty of the measurement, the first particle of a pair was correlated onto the region surrounding the second particle. The correlation map was characterized by two peaks, one for the correlation of the first particle onto itself and one for the correlation of the first particle onto the second one. The apex of the two peaks was identified by fitting a Gaussian distribution on the correlation map and finding its maximum. The displacement $\mathbf{s}$, corresponding to the distance between the two peaks was used to calculate velocity, and the midpoint of the segment joining the two peaks was taken as the origin of the velocity vector.

Auto-correlation was more accurate than finding the position of the first particle, the position of the second particle and computing the distance between them. In the first case, only one measurement is involved, the displacement of the interrogation spot, $\mathbf{s}$. In the second case, there is an error associated with the location of each particle.

3.4.5 Test Conditions

During a PIV test, high frequency transducer data was acquired to determine the test conditions of each picture. The most important measurements are NGV inlet total pressure, rotor exit static pressure and supply-tank static temperature and pressure.

Assuming isentropic expansion between the supply tank and the test section, the total temperature can be calculated at the NGV inlet:

$$T_{t4}(t) = T_1(0)\frac{P_{t4}(t)}{P_1(0)} \tag{3.3}$$

The ACE turbine stage used for the PIV experiments was studied extensively by Rolls-Royce. Under design conditions, the NGV's are choked and the non-dimensional weight flow remains constant according to the similarity principle. Rolls-Royce measured the corrected weight flow to be:

$$\frac{W\sqrt{T_t}}{P_t} = 8.250 \times 10^{-4}\ m^2 \tag{3.4}$$

for the MIT BDT scaled version of the ACE turbine. The dimensional mass flow of the turbine can therefore be calculated for the PIV conditions. Rolls-Royce streamline calculations were also available for the PIV test conditions. These were used to calculate the average flow angle at the rotor inlet based on the similarity principle.

The relative position of the rotor with respect to the stator was obtained by locating the leading edge of the rotor in the digitized picture and relating it to the position of the picture frame relative to the stator. The test conditions for each picture are presented in Table 3.3.

3.5 Results

The image processing algorithm was used to reduce 37 pictures. Due to spread in the quality of the pictures - different optical settings, seeding densities and test conditions were used - some velocity fields contained as many as 700 velocity vectors, some as few as 50. A typical reduced flow field is presented in Figures 3-7 and 3-8.

The PIV solutions shared some common features. (1) There was more data at the rotor outlet than at the inlet. This is a consequence of the laser lighting system. Since the laser probes were located upstream and downstream of the stage, the inter-blade passage is not illuminated enough to yield good results despite the transparent stators. (2) The velocity vectors are much denser on the pressure side of the blades than on the suction side. It is conceivable that styrene particles with a density 225 times that of Argon-CO_2 could be migrating from the suction side as they make their way through the rotor passage, explaining the low particle density near the rotor exit suction side.

3.6 Chapter Summary

This experiment was planned as a proof of concept for the application of PIV in rotating turbomachinery. The quality of the results was such, however, that analysis of the data was instructive. The subsequent chapters focus on this analysis.

Implementing PIV in a full-scale turbine stage was challenging due to geometric restrictions and short time scales in the blowdown facility. These constraints dictated many of the technical choices. However, subsequent PIV experiments in a blowdown facility could benefit from implementing changes to the experimental set-up:

1. The flow in the ACE turbine is well behaved and has been extensively studied. It was therefore fairly easy to determine the direction of the flow when pairing particles. In a compressor with local flow reversal, it would be difficult to separate particles belonging to the first laser flash from those belonging to the second one in a double-exposure picture. Using a digital camera alleviates the problem of velocity direction ambiguity. Two successive laser flashes are captured on different frames, instead of one for a double exposure on a single picture. This choice also allows cross-correlation of the two successive images and yields a flow field on a uniform grid. This method, however, averages out the small scale features of the flow and low-density PIV might be more appropriate for certain applications. In this case, Wernet suggests using two light sheet pulses of different wavelength and color film to prevent flow direction ambiguity while still capturing local small scale flow features with particle tracking

velocimetry [28].

2. In the results presented in this thesis, the timing of the laser light pulses was random with respect to the rotor position. Firing the laser at a frequency matching that of the rotor would allow tracking the changes in the flow for a single rotor passage and give information on the magnitude of the aperiodic and periodic unsteadiness of the flow. If the laser flashes were fired close enough to each other, the evolution of the unsteadiness in a single blade passage could also be quantified.

3. The application of PIV in turbomachinery presents many challenges. One is the interpretation of the data: fluid in an axial turbine flows along a circular annulus; the laser light sheet on the other hand is planar and only captures 2D features of the flow. This can be a problem for two reasons: (1) turbomachinery flow is rarely 2D, and streamlines do not keep a constant radius throughout an engine; (2) if the width of the area being studied is large relative to the circumference of the annulus, the flow being observed throughout the picture will correspond to different radial positions and therefore to different streamlines. If the radial component of velocity is not available, it can be difficult to interpret the results. This problem has stimulated research in the area of 3D PIV [21].

Image	NGV inlet stagnation pressure [Pa]	NGV inlet stagnation temperature [K]	Rotor exit stagnation pressure [Pa]	Rotor exit static pressure [Pa]	Pressure ratio, π	Rotor angular speed, ω [rps]	Mass flow [kg/s]	Rotor inlet flow angle [deg]	Rotor/stator index
2649	255155	330	66164	52530	3.86	121.1	11.59	47.5	0.19
2650	245606	327	62094	52261	3.96	120.4	11.20	47.3	0.11
2651	238097	325	61233	53034	3.89	119.8	10.90	49.4	0.90
2652	230755	323	60382	53185	3.82	119.1	10.60	49.2	0.37
2653	223343	321	60359	54886	3.70	118.3	10.29	49.0	0.18
4001	235329	324	62977	52436	3.74	121.1	10.79	46.9	0.85
4002	228690	322	61824	52549	3.70	120.6	10.51	49.2	0.05
4003	221371	320	60567	52661	3.65	120.0	10.21	46.6	0.10
4004	214481	318	59893	52793	3.58	119.2	9.92	48.8	0.97
4005	207369	316	60218	54646	3.44	118.3	9.63	48.6	0.19
4007	248911	325	63074	52324	3.95	121.1	11.39	47.1	0.54
4008	242012	323	61554	52993	3.93	120.6	11.11	46.9	0.30
4009	233670	321	61328	52452	3.81	119.9	10.77	46.6	0.00
4010	227022	319	60473	53626	3.75	119.3	10.49	46.4	0.11
4011	219376	316	60309	55139	3.64	118.3	10.18	48.6	0.92
4013	246182	328	63443	52630	3.88	120.7	11.22	47.3	0.49
4014	240170	325	62108	52747	3.87	120.2	10.99	49.4	0.74
4015	232137	324	61201	51982	3.79	119.6	10.65	46.9	0.20
4017	218482	319	60344	54621	3.62	118.1	10.09	48.9	0.00
4019	253487	330	63030	52606	4.02	121.8	11.52	47.5	0.62
4021	237947	325	61321	52864	3.88	121.0	10.89	49.4	0.82
4022	231187	323	60413	53238	3.83	120.4	10.61	49.2	0.46
4023	223694	321	60374	55052	3.71	119.8	10.30	46.6	0.50
4025	245394	326	65039	52512	3.77	121.2	11.21	47.2	0.00
4026	237544	325	61890	52053	3.84	120.7	10.87	49.4	0.78
4027	230944	322	61400	52638	3.76	120.1	10.61	46.8	0.69
4028	223518	320	60363	53307	3.70	119.4	10.30	46.6	0.53
4029	217176	318	60305	54981	3.60	118.7	10.05	48.8	0.81
4034	225650	322	59921	53392	3.77	120.6	10.38	46.7	0.57
4035	217976	320	60085	54918	3.63	119.8	10.06	48.9	0.86
4037	251256	325	63932	52589	3.93	120.6	11.49	47.1	0.77
4038	244403	324	62325	52212	3.92	120.0	11.20	47.0	0.94
4039	236688	321	61700	53071	3.84	119.5	10.89	49.1	0.91
4053	222056	319	60611	54854	3.66	119.0	10.26	48.9	0.84
4055	249997	329	62279	52913	4.01	122.6	11.36	44.8	0.46
4056	242636	327	61652	53371	3.94	122.5	11.08	47.2	0.44
4057	235494	325	60472	53234	3.89	122.2	10.78	47.0	0.75

Table 3.3: Experimental conditions for the PIV images.

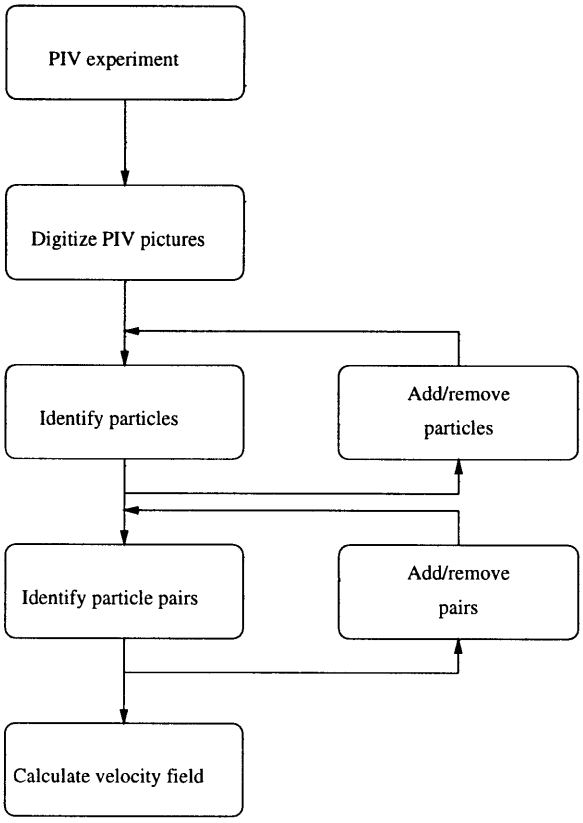

Figure 3-4: Image processing algorithm for PIV images.

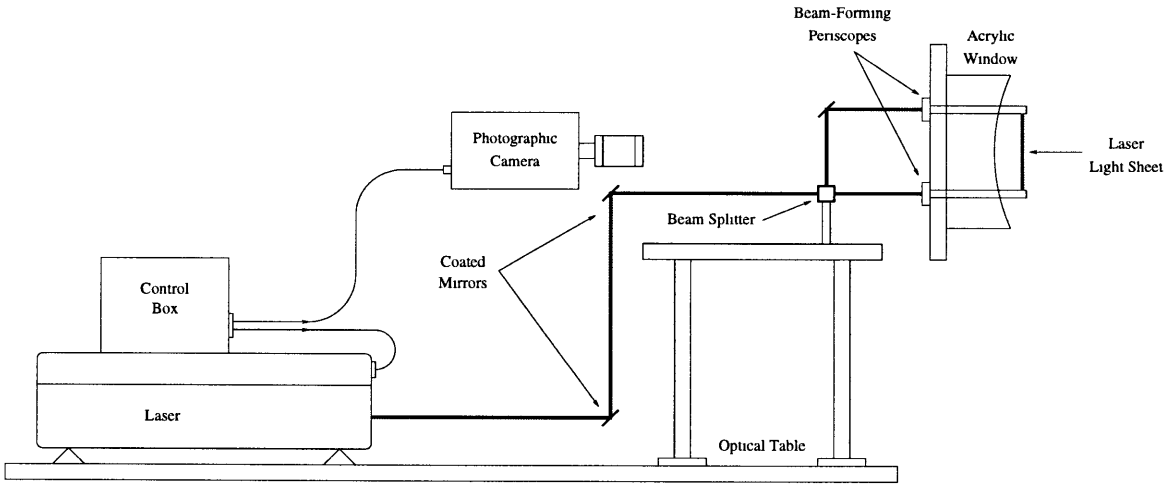

Figure 3-5: Optical system for particle-image velocimetry experiments.

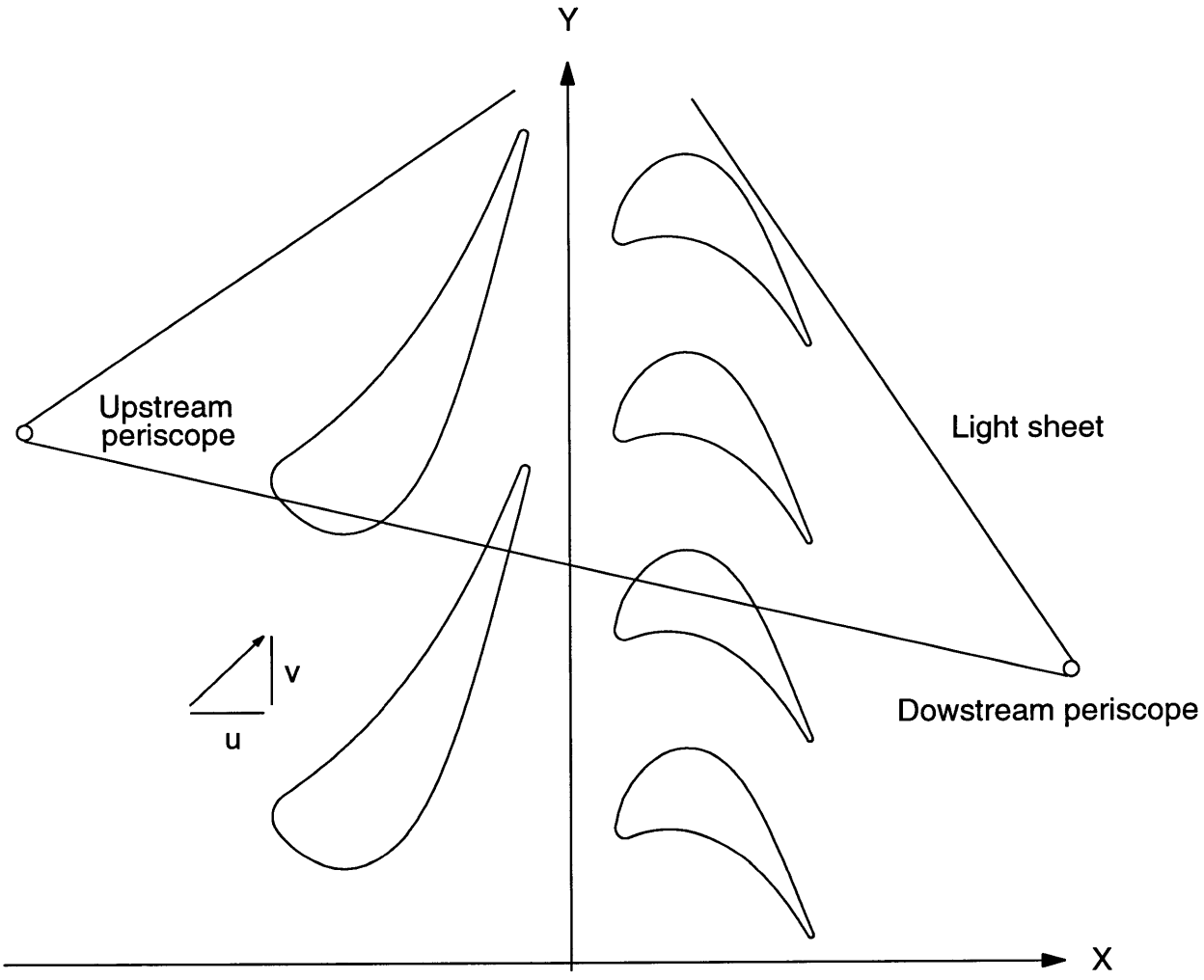

Figure 3-6: Schematic view of the laser light sheet plane.

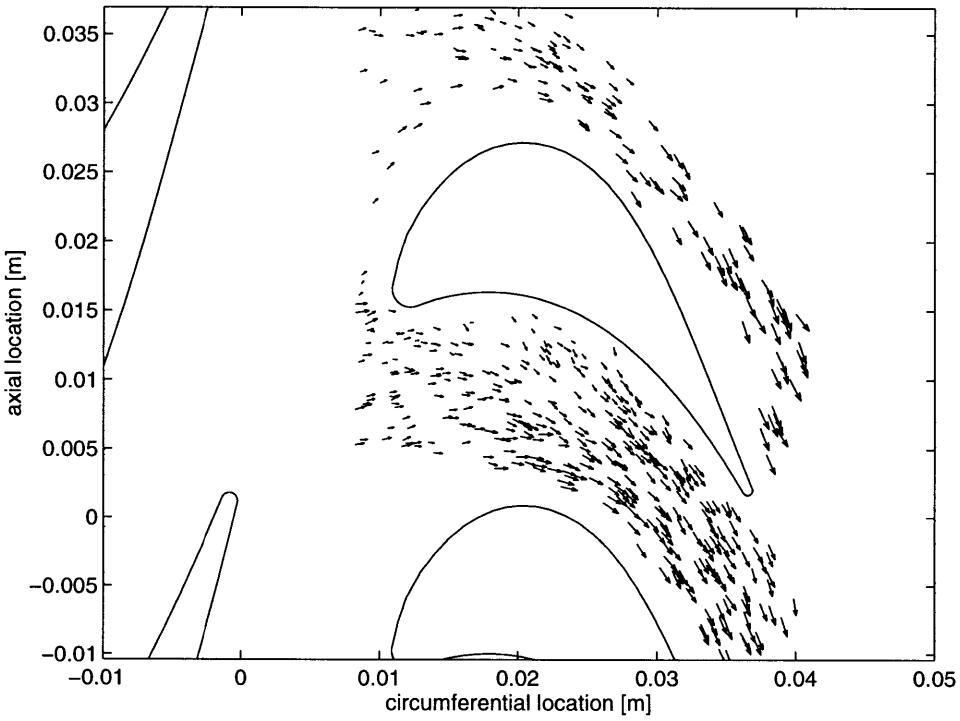

Figure 3-7: Instantaneous velocity field at the midspan of the ACE turbine in the rotor reference frame (image 4001).

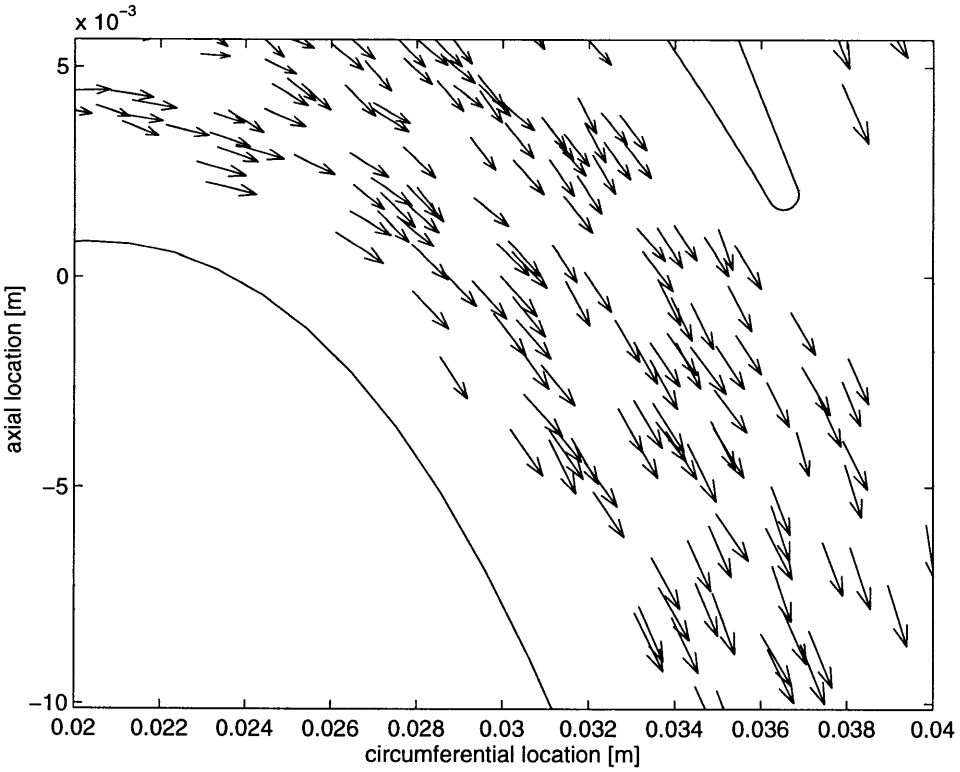

Figure 3-8: Close-up of rotor passage exit PIV solution (image 4001).

Chapter 4

Numerical Modeling of the Flow through the ACE Turbine

4.1 Introduction

This chapter presents the numerical modeling of the flow through the ACE turbine at the test conditions of the PIV experiments, using the UNSFLO code. This theoretical baseline will be used to analyze the results of the PIV experiments.

The first part of this chapter describes the UNSFLO code and the inputs necessary for computation. Typical results are presented as well as a detailed study of the effects of initial conditions and rotor/stator relative position on the rotor passage flow.

4.2 Numerical Model (UNSFLO)

UNSFLO is a quasi-3D, Reynolds-averaged, unsteady multi-blade row, Navier-Stokes solver developed by Giles [15] & [16]. The code solves the thin shear layer Navier-Stokes equations on a body fitted boundary layer grid using an implicit algorithm and the Euler equations on an outer inviscid grid using an explicit algorithm. For unsteady calculations, the interface between two successive blade rows is solved using time-inclined computational planes. To permit arbitrary rotor-stator pitch ratios, the code uses a space-time coordinate transformation called "time-tilting". Numerical smoothing is used to numerically capture shocks and to prevent saw-tooth oscillations in the solutions. The non-reflecting boundary con-

ditions at the flow inlet, outlet and at the blade row interface allow to bring the far-field location close to the blades without any detrimental effect on the solution. The smaller computational domain leads to more efficient calculations. Quasi-three dimensional effects are obtained by specifying a streamline height distribution across the blade rows.

The inviscid grid is an unstructured triangular grid on which the Euler equations are solved using a second-order accurate generalization of Ni's Lax-Wendroff algorithm. The viscous grid is a structured O-type mesh around each blade and uses an algebraic turbulence model. This model is not capable of predicting boundary layer transition and for the calculations in this thesis, transition to turbulence is assumed at the leading edge of the blade [2].

The Navier-Stokes and Euler equations are solved in non-dimensional form. Dimensions are non-dimensionalized by an arbitrary length scale (L_{ref} = 1.0 m). Flow properties are normalized by P_{ref}, T_{ref}, ρ_{ref} and c_{ref}, the stagnation stator inlet pressure, temperature, density and speed of sound, respectively. The last two reference quantities are defined as:

$$\rho_{ref} = \frac{P_{ref}}{R_{gas} T_{ref}} \qquad \text{and,} \qquad c_{ref} = \sqrt{\gamma R_{gas} T_{ref}} \tag{4.1}$$

where R_{gas} is the fluid gas constant and γ is the specific heat ratio.

4.3 Assessment of the UNSFLO Code

The UNSFLO code has been validated extensively, both against theoretical data and experimental data. Abhari compared UNSFLO solutions to ACE turbine cascade measurements and to heat transfer measurements for the rotating ACE turbine [1] & [2]. Giles et al. compared the results with theoretical aerodynamic and heat transfer predictions for a flat plate cascade [17].

Two important points come out of the validation of UNSFLO. (1) The turbulence model in the viscous grid does not adequately predict the heat transfer between the blades and the flow and is not capable to predict boundary layer transition. For this reason, the transition is assumed to be at the leading edge of the blades. (2) The input of the streamline height has a direct influence on the predictions of the flow and in particular on the prediction of

the shock structure.

4.4 Computational Procedure

The computational domain for the unsteady calculations consists of 2 NGV passages and 4 rotor passages to model the decimal rotor-stator pitch ratio of the ACE turbine stage ($number\ of\ blades/number\ of\ vanes \approx 1.69$). For the calculations, 16 points were used across the boundary layer and a total of 32,000 points were used throughout the domain (Figure 4-1). The outlet plane of the grid was chosen to match with the location of the static pressure taps in the experimental set-up. The steady and unsteady solutions required less than 24 CPU hours on a IBM RS/6000.

The streamline height distribution used as an input for the quasi-3D code was obtained from a streamline curvature prediction provided by Rolls-Royce for the test conditions of the PIV experiments. Figure 4-5 shows the streamline height used for the quasi-3D calculations and the location of the laser light sheet during the experimental tests.

Steady calculations required about 10,000 iterations to reach a converged solution with RMS residual of approximately 10^{-6}. For the unsteady calculations, 7 to 10 periods (time for the rotor grid to move through 2 NGV passages) were used.

4.5 Initial Conditions

The initial conditions for the CFD calculations were computed from the test conditions of the PIV experiments. The non-dimensional inputs include:

Reynolds number: $$RE = \frac{R_{ref} U_{ref} L_{ref}}{\mu_{ref}} \tag{4.2}$$

Outlet static pressure: $$POUT = \frac{P_{outlet}}{P_{ref}} \tag{4.3}$$

Rotor speed: $$VROTOR = \frac{2\pi R\omega}{c_{ref}} \tag{4.4}$$

Sutherland's temperature constant: $$TVCON = \frac{S_1}{T_{ref}} \tag{4.5}$$

Wall temperature: $$TWALL = \frac{T_{wall}}{T_{ref}} \tag{4.6}$$

The CFD initial conditions corresponding to the the PIV results are compiled in Table 4.1.

4.6 Results

The velocity field of several of the PIV pictures was calculated using UNSFLO. Figure 4-2 presents a contour plot of the velocity magnitude in the rotor relative reference frame for typical PIV test conditions. The disturbance generated by the stator wake in the rotor inlet flow is distinguishable. Abhari studied the time-unsteady behavior of the incoming wakes and concluded that they had a significant effect on the rotor flow in their interaction with the rotor boundary layers (cf. Figure 4-3).

Two oblique shocks per rotor passage can also be identified on Figure 4-2; one on each side of the trailing edge. Schlieren photographs by Bryanston-Cross in a cascade and calculations by Abhari also predict their presence [1]. These studies, however, were conducted at design point and predict complex shock patterns as seen in Figure 4-4. The PIV experiment and the CFD results contained in this thesis were conducted at lower pressure and temperature and reflected shock patterns were not observed.

4.7 Sensitivity of the Flow to Variations in Computational Parameters

The purpose of the CFD calculations is to obtain a basis for the evaluation of the PIV data. The PIV data is more sparse than the CFD solutions. For this reason, the sensitivity of the CFD solution to the boundary conditions and the rotor/stator relative position must be assessed to define the conditions under which PIV data from different images can be averaged and aggregated. The effect of test conditions on the rotor passage flow are investigated first to determine if different pictures with the same rotor/stator indices can be used together. The effect of rotor/stator index is then investigated to quantify the magnitude of the periodic unsteadiness due to rotor/stator interactions.

4.7.1 Sensitivity to Boundary Conditions

In order to quantify the importance of the initial conditions for the different images, the flow field in the rotor passage was computed for four extreme cases of initial conditions for the same rotor/stator index: highest and lowest mass flow (images 4005 and 2649 with $\dot{m} = 9.63$ kg/s and $\dot{m} = 11.59$ kg/s, respectively) and most shallow and steepest rotor inlet flow angle (images 4055 and 4014 with $\theta = 44.8^o$ and $\theta = 49.4^o$, respectively). This implies that the mass flow for the different images is roughly $\dot{m} = 10.6$ kg/s $\pm 10\%$ and the rotor inlet flow angle $\theta = 47.1^o \pm 2.3^o$. The PIV experiments were conducted slightly off the design conditions of $\dot{m} = 16.55$ kg/s and $\theta = 57.0^o \pm 2.3^o$. The convention for the definition of θ is illustrated in Figure 4-6.

The rotor inlet flow angle, the mass flow and the rotor/stator index for each image are presented in Table 3.3. The stator exit flow angle and mass flow were obtained using the similarity principle, from Rolls-Royce streamline curvature calculations at the PIV experimental conditions. The rotor inlet flow angle was computed by accounting for the rotor speed for each image. The rotor/stator index was calculated using the rotor position on the digital pictures (cf. Section 3.4.5).

The 2D components of velocity for the extreme cases described above are presented in figure 4-7. The velocity profiles across the rotor passage are shown at four different axial

locations illustrated in Figure 4-6. The velocities in the absolute frame are expressed in $[m/s]$ and are plotted as a function of the circumferential location.

The results show that the axial component of velocity is fairly constant for all the experimental conditions in the upstream two-third of the rotor passage. The maximum difference between the four extreme cases is about $1m/s$ for a velocity of 100 to $200m/s$. As expected for the rotor inlet flow, the conditions with the smaller inlet angle yield the smallest circumferential component of velocity. The maximum difference in v is on the order of $20m/s$ and $10m/s$ at $x = 0.01$ and $x = 0.02$ respectively which corresponds to just upstream of the rotor and to the first third of the rotor passage. At $x = 0.03$, both the axial and circumferential components of velocity agree within $1m/s$ for a velocity magnitude of several hundred m/s. At the rotor exit, especially in the wake, the initial conditions become significant again with differences of more than $40m/s$ between the four cases. As expected, the low mass flow case has the smallest axial and circumferential velocities and the high mass flow case the highest.

This analysis shows that for images taken at the same rotor/stator position, the initial conditions should not prevent comparison of the data within the rotor passage and that for the inlet and exit flow, the PIV data can be aggregated as long as the test conditions are sufficiently similar (a 5% difference in supply tank pressure, temperature and rotor speed translate into a few percent difference in velocity component magnitude).

4.7.2 Sensitivity to Rotor/Stator Relative Position

In Table 3.3, the rotor/stator relative position is given for each picture. κ is defined as the ratio of the rotor position and the stator pitch. Since the laser flashes were not synchronized with the rotor angular position during the PIV experiments, the rotor/stator position for the different images is somewhat random. It is therefore necessary to assess the effect of rotor/stator index on the flow field to determine which PIV images can be compared with each other.

Figure 4-9 presents the 2D components of velocity at 4 axial positions (cf. Figure 4-6) in the rotor passage for five different rotor/stator indices, as presented in Figure 4-8. It is important to note that the velocity profiles for $\kappa = 0.0$ and $\kappa = 1.0$ are the same because

the CFD code only accounts for periodic unsteadiness of the flow. In the present case, the unsteadiness is due to stator/rotor interactions and has a period of one stator pitch.

The results for the different rotor/stator indices vary by several hundred percent for the different cases especially at the inlet of the rotor. This shows that the wakes of the stators have a large influence on the rotor flow and that it is important to use an unsteady solution with rotor/stator interaction to study the flow in the ACE turbine. The wake of the stator is seen to diffuse out as it progresses through the rotor passage. At two-thirds of the rotor passage, the maximum difference is about 20% for both the axial and circumferential velocities and diminishes slightly as the flow exits the rotor passage. It can be concluded that the comparison or averaging of data from images with different rotor/stator indices would not be very instructive as CFD predicts very different results. Also, this conclusion makes a point for synchronizing the laser timing to the rotor speed in turbomachinery PIV experiments to get repeated measurements of the flow under similar conditions. This added feature would allow to quantify the effects of periodic unsteadiness and random unsteadiness due to vortex shedding and other unsteady aperiodic fluid phenomena.

4.8 Chapter Summary

Converged solutions of the flow through the ACE turbine were computed using UNSFLO with the boundary conditions of the PIV experiments. CFD solutions were compared for four extreme cases of the PIV experimental conditions: highest and lowest mass flow and most shallow and steepest rotor inlet angle. The effects of the different test conditions was found to be relatively benign within the rotor passage and to be small for most pictures at the rotor inlet and outlet. On the other hand, the influence of the rotor/stator relative position was found to be so significant that PIV results should not be compared with each other unless the rotor/stator index is the same.

Image	P_{ref} [Pa]	T_{ref} [K]	U_{ref} [m/s]	ρ_{ref} [kg/m^3]	RE	P_{out}	V_{rotor}	γ	TVCON	T_{wall}	Prandtl number
2649	255155	330	283.1	4.0732	7.082E+07	0.21	0.688	1.279	0.68	0.90	0.769
2650	245606	327	281.9	3.9521	6.844E+07	0.21	0.691	1.279	0.68	0.91	0.769
2651	238097	325	281.1	3.8552	6.656E+07	0.22	0.666	1.279	0.68	0.92	0.769
2652	230755	323	280.0	3.7638	6.474E+07	0.23	0.669	1.279	0.68	0.92	0.769
2653	223343	321	279.2	3.6655	6.285E+07	0.25	0.671	1.279	0.68	0.93	0.769
4001	235329	324	280.5	3.8248	6.591E+07	0.22	0.694	1.279	0.68	0.92	0.769
4002	228690	322	279.9	3.7330	6.418E+07	0.23	0.669	1.279	0.68	0.92	0.769
4003	221371	320	278.8	3.6415	6.237E+07	0.24	0.698	1.279	0.68	0.93	0.769
4004	214481	318	278.0	3.5496	6.061E+07	0.25	0.674	1.279	0.68	0.94	0.769
4005	207369	316	276.9	3.4580	5.883E+07	0.26	0.676	1.279	0.68	0.94	0.769
4007	248911	325	281.1	4.0286	6.956E+07	0.21	0.693	1.279	0.68	0.92	0.769
4008	242012	323	280.1	3.9443	6.787E+07	0.22	0.695	1.279	0.68	0.92	0.769
4009	233670	321	279.1	3.8357	6.577E+07	0.22	0.698	1.279	0.68	0.93	0.769
4010	227022	319	278.2	3.7513	6.411E+07	0.24	0.700	1.279	0.68	0.94	0.769
4011	219376	316	277.2	3.6510	6.217E+07	0.25	0.675	1.279	0.68	0.94	0.769
4013	246182	328	282.3	3.9513	6.851E+07	0.21	0.690	1.279	0.68	0.91	0.769
4014	240170	325	281.1	3.8884	6.713E+07	0.22	0.666	1.279	0.68	0.92	0.769
4015	232137	324	280.4	3.7764	6.504E+07	0.22	0.694	1.279	0.68	0.92	0.769
4017	218482	319	278.4	3.6048	6.165E+07	0.25	0.672	1.279	0.68	0.93	0.769
4019	253487	330	283.0	4.0483	7.037E+07	0.21	0.688	1.279	0.68	0.90	0.769
4021	237947	325	281.0	3.8537	6.652E+07	0.22	0.666	1.279	0.68	0.92	0.769
4022	231187	323	280.2	3.7661	6.482E+07	0.23	0.668	1.279	0.68	0.92	0.769
4023	223694	321	279.2	3.6703	6.294E+07	0.25	0.697	1.279	0.68	0.93	0.769
4025	245394	326	281.6	3.9581	6.846E+07	0.21	0.692	1.279	0.68	0.91	0.769
4026	237544	325	281.0	3.8476	6.641E+07	0.22	0.666	1.279	0.68	0.92	0.769
4027	230944	322	279.8	3.7724	6.484E+07	0.23	0.696	1.279	0.68	0.93	0.769
4028	223518	320	279.0	3.6726	6.294E+07	0.24	0.698	1.279	0.68	0.93	0.769
4029	217176	318	278.0	3.5941	6.137E+07	0.25	0.674	1.279	0.68	0.94	0.769
4034	225650	322	279.6	3.6912	6.340E+07	0.24	0.696	1.279	0.68	0.93	0.769
4035	217976	320	278.7	3.5895	6.145E+07	0.25	0.672	1.279	0.68	0.93	0.769
4037	251256	325	281.2	4.0635	7.019E+07	0.21	0.692	1.279	0.68	0.92	0.769
4038	244403	324	280.7	3.9681	6.841E+07	0.21	0.694	1.279	0.68	0.92	0.769
4039	236688	321	279.5	3.8756	6.653E+07	0.22	0.670	1.279	0.68	0.93	0.769
4053	222056	319	278.5	3.6623	6.265E+07	0.25	0.672	1.279	0.68	0.93	0.769
4055	249997	329	282.9	3.9943	6.942E+07	0.21	0.717	1.279	0.68	0.91	0.769
4056	242636	327	281.8	3.9091	6.765E+07	0.22	0.691	1.279	0.68	0.91	0.769
4057	235494	325	280.9	3.8175	6.587E+07	0.23	0.693	1.279	0.68	0.92	0.769

Table 4.1: Computational parameters for the CFD calculations.

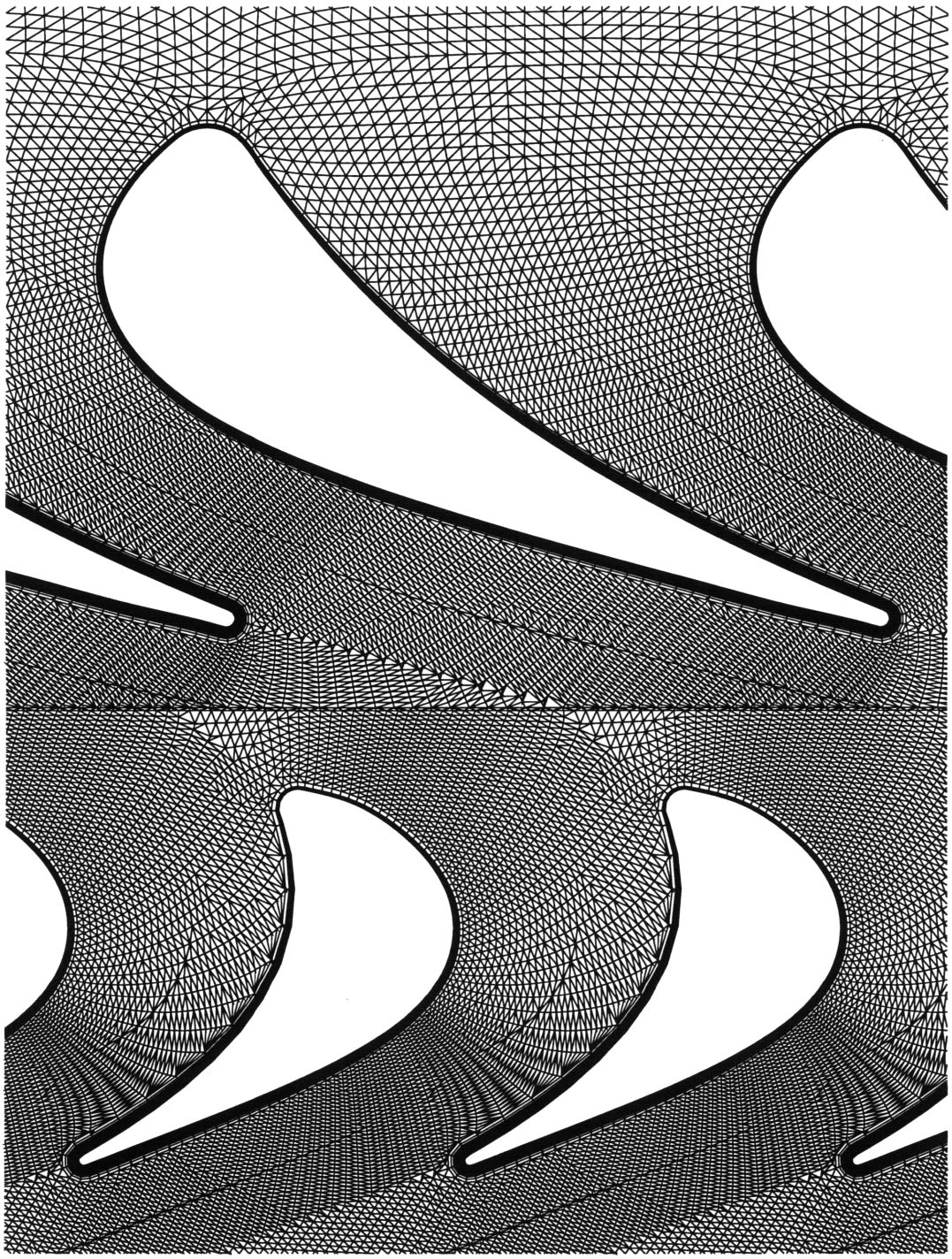

Figure 4-1: Computational grid used to model the flow through the ACE turbine.

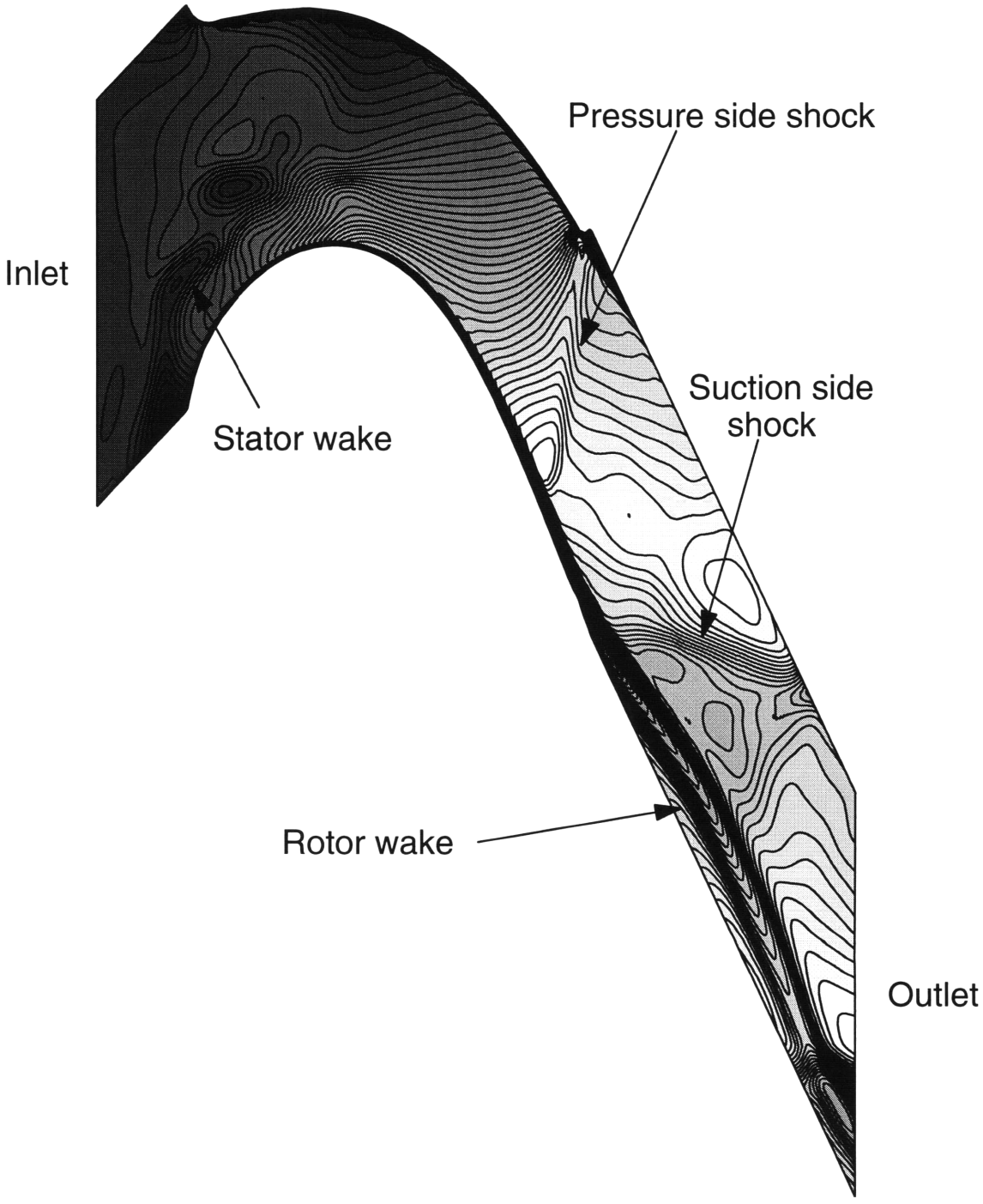

Figure 4-2: Velocity map for the rotor passage in the rotor relative frame (test conditions correspond to image 2651). Each contour level corresponds to 7.5 m/s.

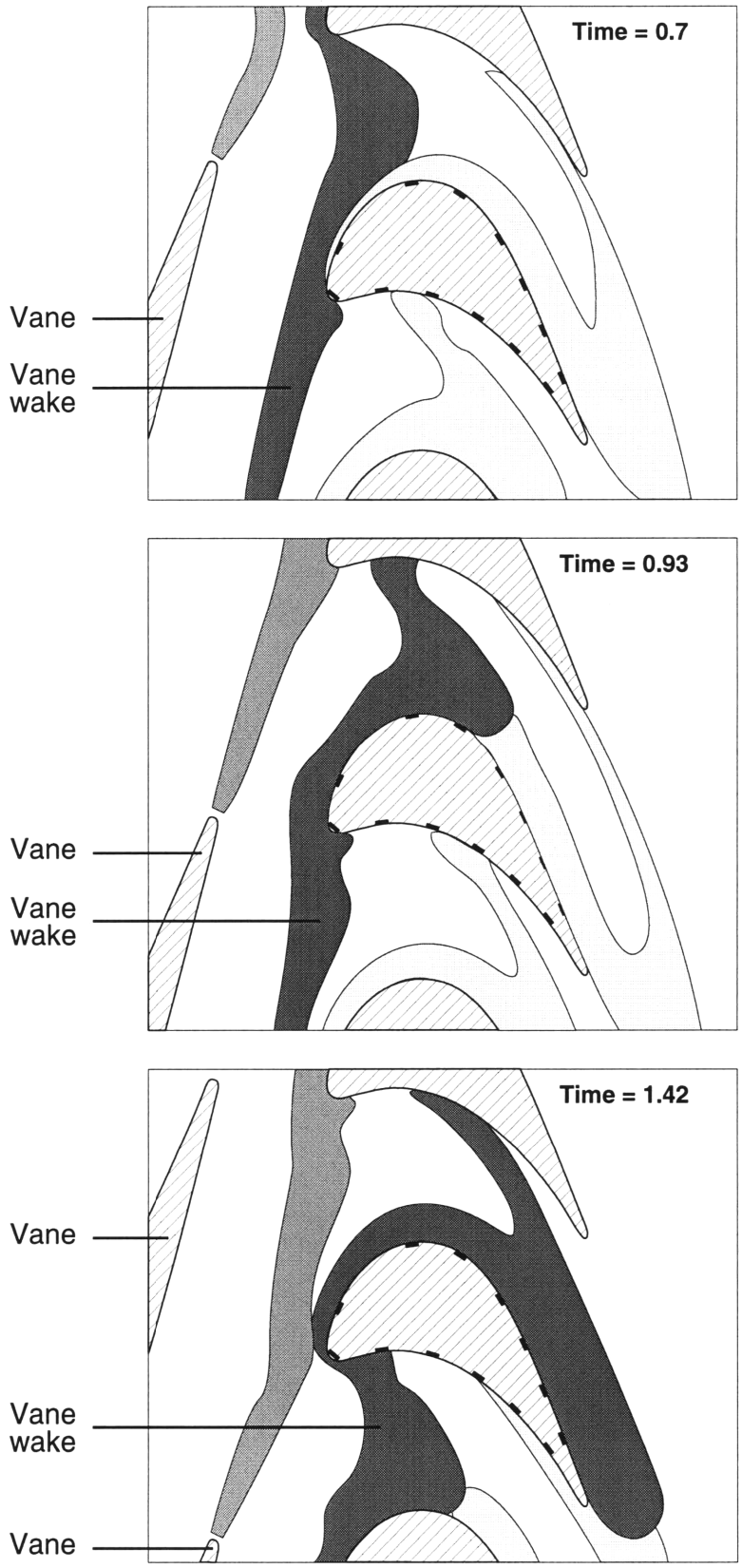

Figure 4-3: Convection of the stator wake in the rotor passage [1].

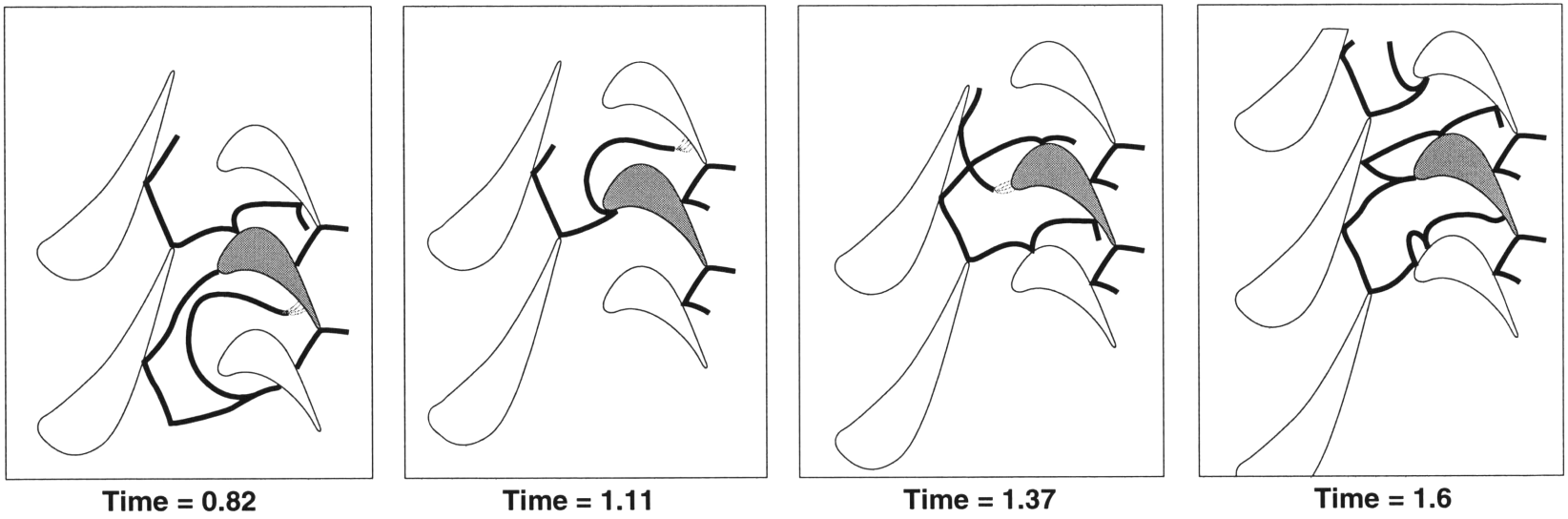

Figure 4-4: Time-unsteady shock patterns in the ACE turbine stage [1].

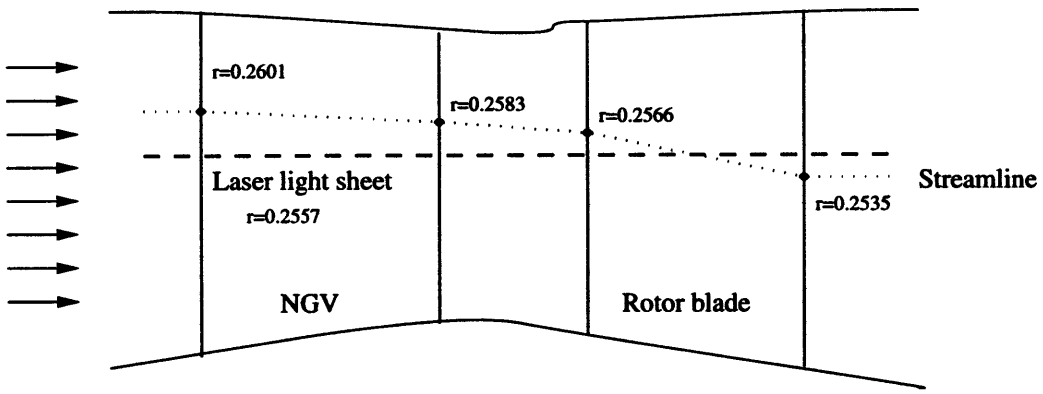

Figure 4-5: Schematic drawing showing the streamline used for the quasi-3D numerical model and the actual position of the light sheet in the PIV experiments. 'r' denotes the radial position in [m].

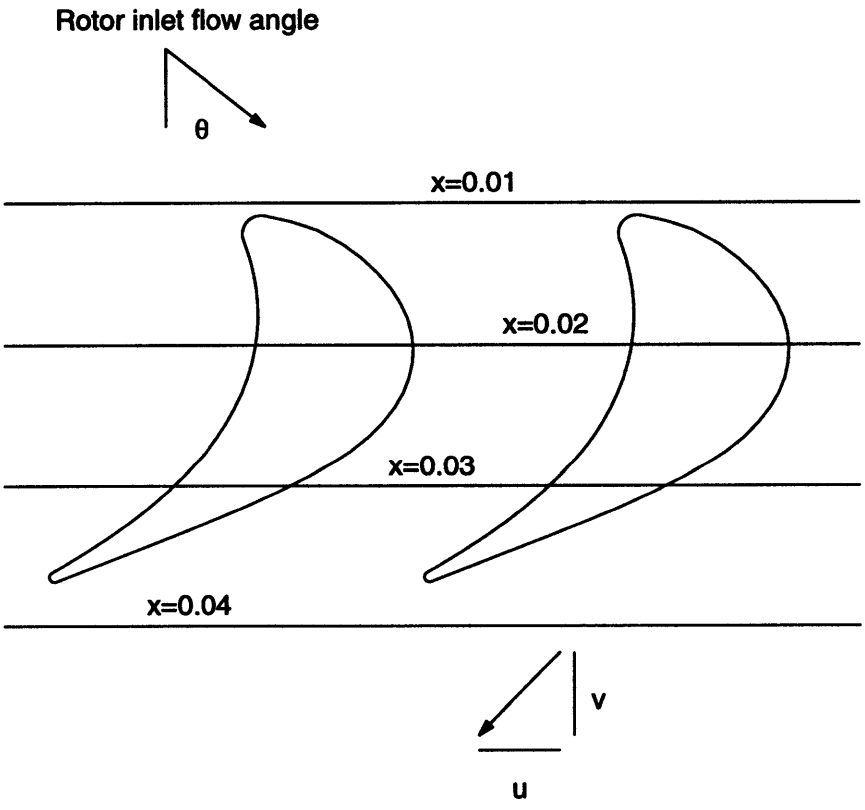

Figure 4-6: Axial location,x , of the velocity profiles and definition of the rotor inlet flow angle.

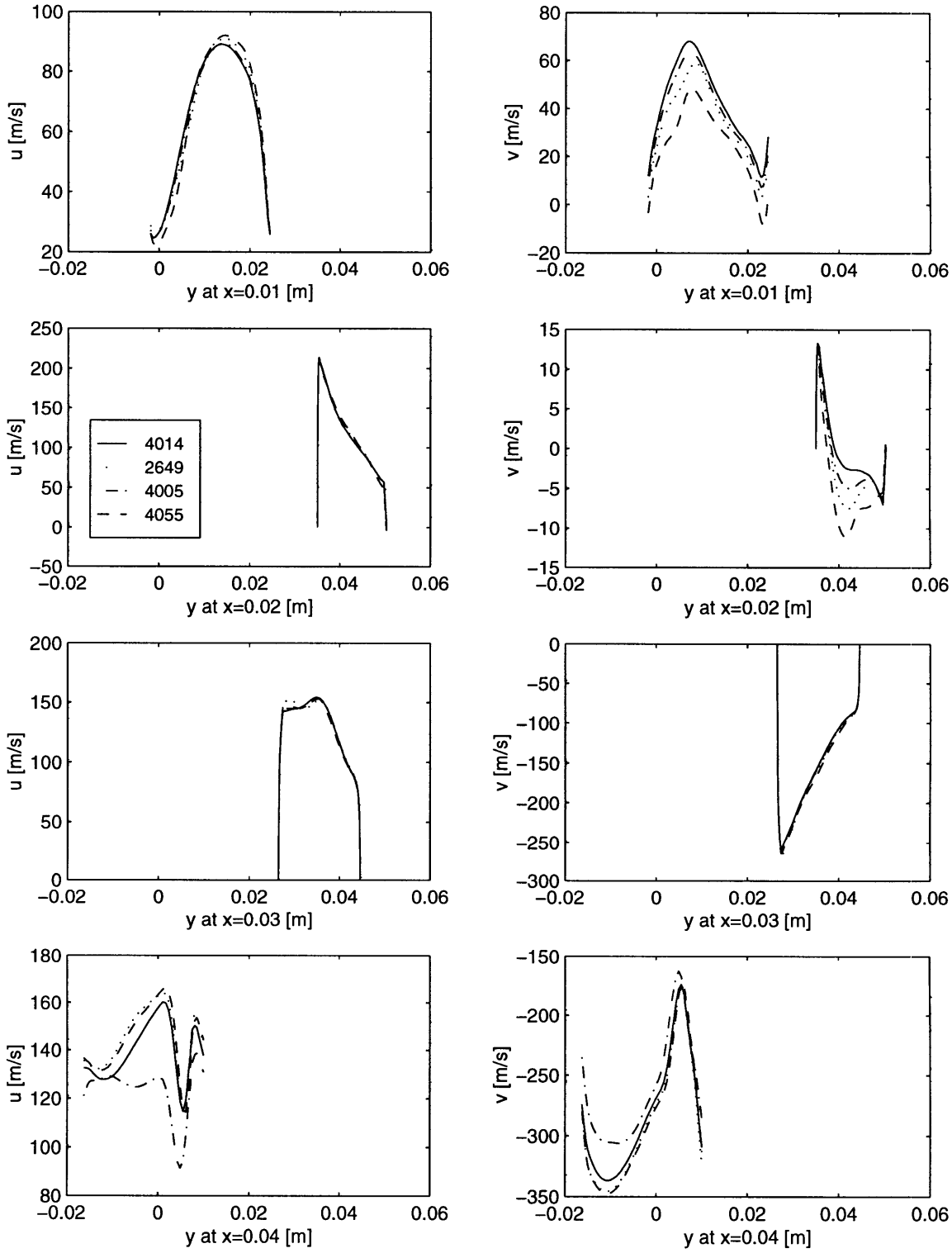

Figure 4-7: Absolute velocity profiles in a single rotor passage for extreme initial conditions at 4 axial locations.

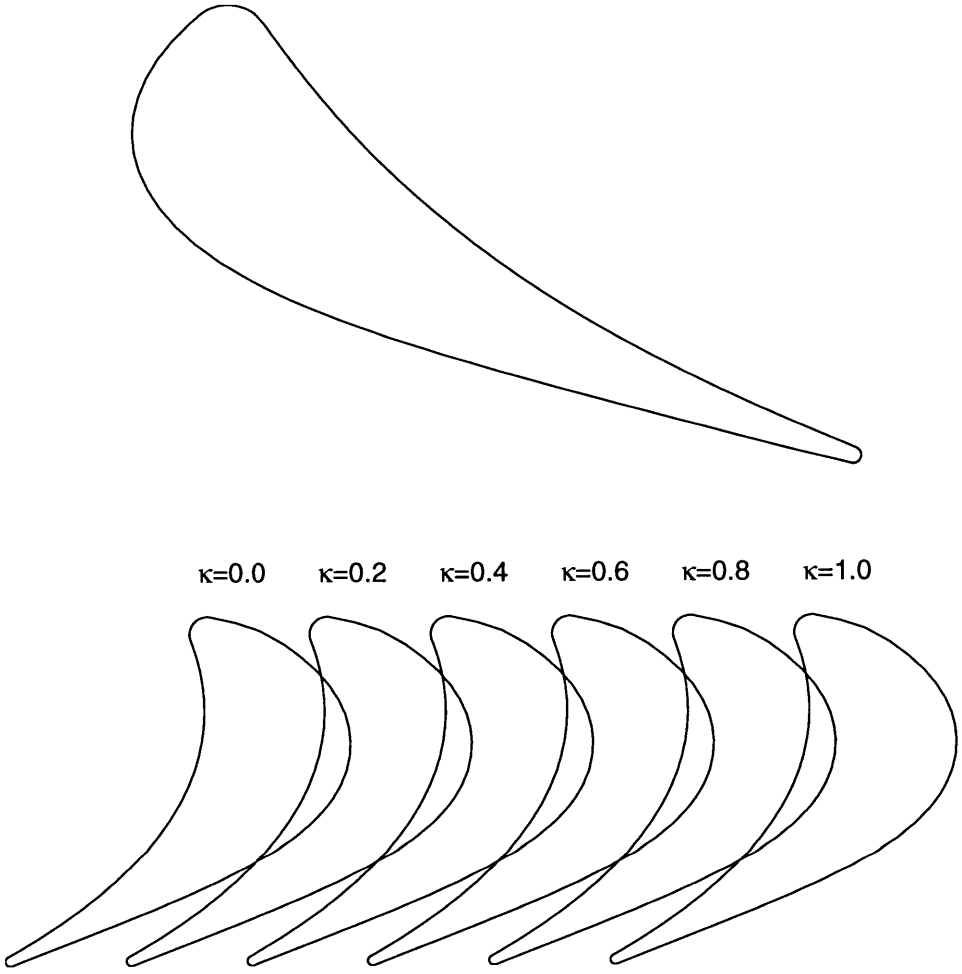

Figure 4-8: Schematic of 5 rotor/stator index positions.

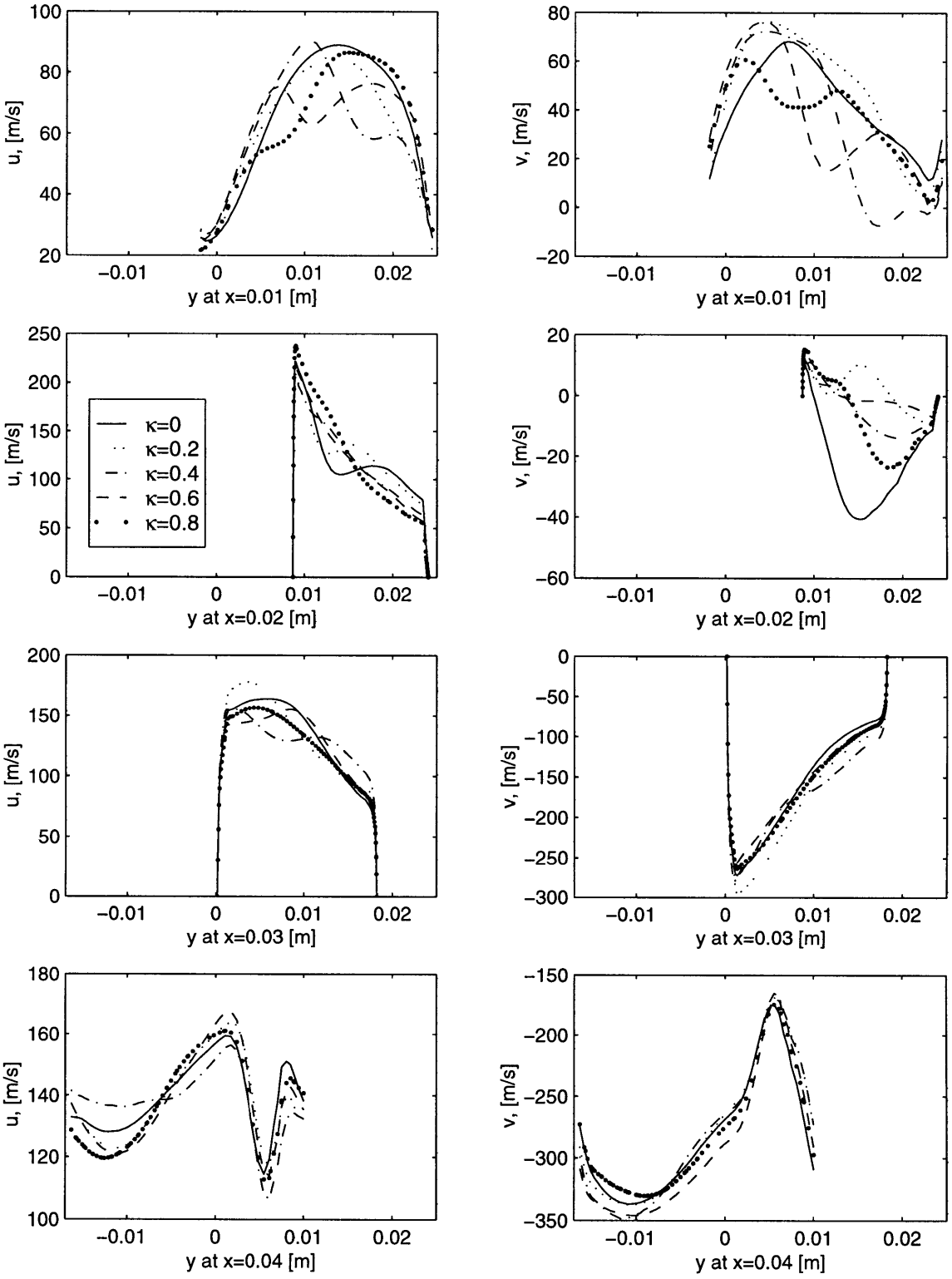

Figure 4-9: Absolute velocity profiles in a single rotor passage for 5 different equispaced rotor/stator indices at 4 axial locations.

Chapter 5

Comparison of PIV Measurements with CFD Results

5.1 Introduction

Computational Fluid Dynamics has become more and more widespread as a tool for research and design. The level of complexity of the flows modeled is ever increasing and this trend justifies the need for an experimental technique yielding CFD like results for code validation. PIV is a strong candidate for such a task and its suitability is tested in this chapter. The combination of CFD and PIV results is very instructive in understanding fundamentals of fluid dynamics. This better understanding can then be used to further improve both the computational and experimental techniques.

This chapter focuses on obtaining a quantitative comparison of the PIV and the CFD results and an explanation for any discrepancy. This task is challenging because of the nature of the data: CFD solutions are structured arrays of flow properties over an entire domain and represent averages over the area of a computational cell; PIV results give local but randomly positioned solutions to the motion of particles immersed in the fluid. The flow predicted by the two methods is intrinsically different: CFD codes assume periodicity of the flow and explicit boundary conditions; PIV is an instantaneous snap shot of the unsteady flow. Each method carries its uncertainty: CFD with 2D approximation, numerical smoothing and other numerical assumptions; PIV with successive experimental errors.

The first step in the evaluation was to compare the general features of the solutions and

velocity profiles at different axial locations. Particle dynamics was then studied to explain the discrepancies between the two sets of solutions to the flow through the ACE turbine.

5.2 Comparison of the Velocity Fields

5.2.1 General Features

In order to establish a first order comparison of the CFD and PIV results, the CFD solution was interpolated to the location of the PIV vectors. Figures 5-3 and 5-4 show the velocity fields for both methods. The order of magnitude for the velocity and the general trend of the flow are similar in both cases. A more detailed look reveals that the velocity magnitudes and the flow angles are more uniform for the numerical solution than for the PIV results, in particular at the inlet. In the boundary layer region of the trailing edge of the rotor, the CFD predicts lower velocities than found with PIV.

The PIV and CFD results were qualitatively consistent with each other, but subtle differences motivated a deeper investigation of the discrepancies and of their source.

5.2.2 Comparison of Velocity Profiles

To obtain a more quantitative comparison of the data, velocity profiles in the rotor passage were extracted from the CFD solution of the flow field at equispaced axial locations. Figure 5-5 shows a composite illustration of the velocity profile evolution at six different axial locations. For each axial location, PIV data within $\pm 0.0005\ m$ (2% of the axial rotor chord) of the plane of the axial cut was compared to the numerical velocity profile. Figures 5-6 through 5-11 present the comparison of the CFD results in Figure 5-5 with PIV data for 6 axial cuts and for two adjacent rotor passages. The figures include data from two different PIV images (2651 and 4001) with approximately the same rotor/stator index ($\kappa = 0.9$ and $\kappa = 0.85$ respectively). CFD solutions for both images are displayed.

Rotor Inlet

Figure 5-6 is the profile of the axial and circumferential components of velocity just ahead of the rotor inlet. There is up to 60% difference between CFD and PIV for the axial velocity and up to 25% for the circumferential velocity. The velocity predicted by PIV is found to be higher and lower than the CFD solution depending on the location. The axial location of Figure 5-6 is at the exit of the interblade passage, in a region where the effects of the stator wake are strong. The numerical code does not predict aperiodic unsteadiness. Hence, some of the discrepancy between CFD and PIV might be accounted for by the fact that PIV captures the aperiodic unsteadiness of the stator wake while CFD does not.

Rotor Passage

Figures 5-7, 5-8 and 5-9 show the evolution of the velocity profiles as the flow progresses through the rotor passage. The stator wake is observed well into the rotor passage. It eventually diffuses out as it moves downstream and the velocity profile across the channel becomes more monotonic. Consequently, the spread in the PIV data diminishes as the flow becomes more uniform. Still, PIV and CFD do not agree perfectly and PIV tends to predict lower flow velocities than CFD within the rotor passage.

Rotor Outlet

In figures 5-10 and 5-11, the profiles for the exit of the rotor passage are presented. The spread in the PIV results increases for the axial component of velocity and, overall, the axial velocity predicted by PIV is lower than the numerical calculation. In the circumferential direction, PIV predicts a higher velocity than CFD.

5.2.3 Conclusions of the Comparison

The comparison of the CFD and PIV results was encouraging. The results were in general within 25% of each other, in particular within the rotor passage. The most striking difference in the solutions, however, stemmed from the spread of the PIV data, which was within a band of $\pm 20\%$. The important question, then, is whether the spread is real (i.e. does it

come from unsteadiness in the physical flow and the CFD code is not sophisticated enough to capture it) or whether it is an artifact of the experimental procedure. The author hypothesizes that a large fraction of the disagreements within the data can be accounted for by studying the dynamics of seed particles in a fluid. In this experiment, the seed particles were chosen based on their optical properties at the expense of their flow tracking capabilities. If the mean size of the particles and the spread in the distribution of particles is too large, (1) the particles will not follow the flow properly and (2) different particles will predict different flow velocities depending on their size. A study of particle dynamics is instructive in understanding and quantifying some of the differences between the CFD and PIV results. A model for the motion of seed particles in a fluid from the theory of dusty gases is presented below and implemented to delineate the limits of PIV measurements.

5.3 Particle Dynamics

All PLV techniques inherently measure the Lagrangian velocity of particles, $\vec{V}_p$. It is therefore important to determine whether these measurements can be used to infer the Eulerian velocity of the fluid, $\vec{V}_f(\vec{x}, t)$ [3]. A look at results from the theory of dusty gases can help quantifying the extent to which PIV can predict flow fields.

5.3.1 Theory of Dusty Gases

The behavior of seed particles in a fluid is contingent on (1) the concentration of the particles, and (2) the size of the particles with respect to the length scales of the flow field. This section will focus solely on the extreme case when the concentration is low enough that the probability of interference between particles is close to zero, which is the appropriate case for the experiments in this thesis. At high concentration, the problem is much more complicated. The direct interaction between the particles through collision and the effects on the flow of the proximity of particles can create extra turbulence and increase the dissipation of kinematic energy of the turbulent flow. Size influences the extent to which the particles follow turbulent components of the flow. The smaller the particle is, compared to the turbulence length scale, the better the particles track the flow [22].

The following model is a slightly more general version of the theoretical model proposed by Hinze for the motion of a small particle suspended in a turbulent fluid [22]. The theory stems from the following assumptions:

1. The turbulence of the fluid is homogeneous and steady.
2. The domain of turbulence is infinite in extent.
3. The particle is spherical.
4. The particle is small compared to the smallest wavelength present in the turbulence.
5. During the motion of the particle, the neighborhood will be formed by the same fluid particles.
6. Any external force acting on the particle originates from a potential field, such as a gravity field.

From these assumptions, the momentum balance for the slow motion of a particle in a fluid of variable velocity can be written as:

$$\begin{aligned}\frac{\pi}{6}d^3\rho_p\frac{d\vec{V}_p}{dt} = {} & \frac{\pi d^3}{12}\rho_f\frac{A_c}{V}C_D(Re_p)\mid\vec{V}_f-\vec{V}_p\mid(\vec{V}_f-\vec{V}_p)+\frac{\pi}{6}d^3\rho_f\frac{d\vec{V}_f}{dt} \\ & +\frac{\pi}{12}d^3\rho_f\left(\frac{d\vec{V}_f}{dt}-\frac{d\vec{V}_p}{dt}\right)+\frac{3}{2}d^2\sqrt{\pi\rho_f\mu}\int_{t_0}^{t}dt'\frac{\frac{d\vec{V}_f}{dt'}-\frac{d\vec{V}_p}{dt'}}{\sqrt{t-t'}}+F_e\end{aligned} \tag{5.1}$$

where the subscript f refers to the fluid, the subscript p to the particle and t_0 is the starting time; $\vec{V}_f$ is the velocity of the fluid surrounding the particle but sufficiently remote that it is not disturbed by the relative motion of the particle; A_c is the frontal area of the particle and V is its volume; $C_D(Re_p)$ is the drag coefficient of the particle and can be estimated from a curve fit of the drag data for spheres; the particle Reynolds number, Re_p, is defined as:

$$Re_p = \frac{\rho_f\mid\vec{V}_f-\vec{V}_p\mid d}{\mu} \tag{5.2}$$

On the left-hand side of Equation 5.1, the term is the force necessary to accelerate the particle. On the right hand side, the first term is the viscous resistance force; the second

term is due to the pressure gradient in the fluid surrounding the particle, caused by the acceleration of the fluid; the third term is the force to accelerate the apparent mass of the particle relative to the ambient fluid; the fourth term accounts for the deviation in flow pattern from steady state; and the last term F_e is an external potential force.

For particles with densities much larger than the fluid, the second, third and fourth terms on the right hand side become insignificant. For styrene particles in CO_2 and $Argon$, the ratio of densities is approximately 225 and these terms can be ignored. The effects of constant external potential forces, such as a gravitational field, can also be ignored because the free falling velocity is independent of the fluid motion and can be treated separately.

Equation 5.1 can be simplified to:

$$\frac{d\vec{V}_p}{dt} = \frac{1}{2}\left(\frac{\rho_f}{\rho_p}\right)\left(\frac{A_c}{v}\right) C_D(Re_p) \mid \vec{V}_f - \vec{V}_p \mid (\vec{V}_f - \vec{V}_p) \tag{5.3}$$

5.3.2 Particle Path Model

The trajectory and velocity of discrete particles in a flow field can be estimated by solving Equation 5.3. In order to do so, both the drag coefficient of the particle and the aerodynamic flow field must be specified. That is $C_D(Re_p)$, ρ_f/ρ_p, and $\vec{V}_f$ must be known over the entire flow field [13]. The CFD results presented in Chapter 4 can be used as a discrete solution of the flow field. The drag coefficient can be computed using an analytical solution or an experimental curve fit for the drag of a sphere.

The most important parameter in determining the drag coefficient of a sphere is the Reynolds number as defined in Equation 5.2. In the case of seed particles, the Reynolds number is based on the relative velocity between the particle and the local flow field, the local fluid density and viscosity and the particle diameter [23]. For low speed incompressible flow, the drag coefficient of a sphere can be computed analytically using Stokes' solution, valid for $Re_p < 1$:

$$C_D(Re_p) = \frac{24}{Re_p} \tag{5.4}$$

and Oseen's correction which extends the Stokes solution to $Re_p < 5$. For conditions up to

$Re_p < 200$, an empirical curve fit by Torobin and Gauvin [23] can be used:

$$C_D(Re_p) = \frac{24}{Re_p}(1 + 0.15Re^{0.687}) \tag{5.5}$$

For the motion of seed particles in a transonic flow, the Reynolds number was found to be always smaller than 1. The particle tracking model presented below uses Stokes' solution to calculate the coefficient of drag of the particle. Substituting Equation 5.4 into Equation 5.3 yields a simplified governing equation for the motion of a single particle in a flow field:

$$\frac{d\vec{V}_p}{dt} = \frac{18\mu}{\rho_p d^2}(\vec{V}_f - \vec{V}_p) \tag{5.6}$$

The trajectories of seed particles in the ACE rotor passage were determined by integrating Equation 5.6 numerically using the Runge-Kutta-Nyström method [25]. The calculations were started at the inlet of the rotor passage (x=0.006) for different circumferential positions with the particle velocity set equal to the local flow velocity. The time step used for the numerical integration was determined from the local velocity and a distance step size of 0.5% of the rotor axial chord. Trajectories were computed for particles with different initial circumferential position and different diameters. The calculations were ended when the particles crossed the rotor passage exit plane or came in contact with a rotor blade.

In addition to tracking the motion of discrete particles in the flow field, the motion of fluid particles initiating from the same positions as the seed particles was computed to quantify the deviation of the seed particle trajectories from that of the flow. The trajectories were computed by solving numerically the definition of instantaneous velocity:

$$\frac{d\vec{X}_f}{dt} = \vec{V}_f \tag{5.7}$$

When solving Equations 5.6 and 5.7 numerically, the local fluid velocity, $\vec{V}_f$, was required at each time-step. It was computed by interpolation of the CFD flow field solution.

5.4 Results

5.4.1 Particle Dynamics in the Rotor Passage

The motion of a particle of high relative density in a fluid differs from the motion of a fluid particle in two ways: both the trajectory of the particle and its velocity are different from that of the fluid. Quantifying the difference is paramount to using the Lagrangian velocity of the particle to infer the Eulerian velocity of the fluid.

The particle tracking model was used to follow the path and velocity of particles in one rotor passage at the test conditions of image 2651 (cf. Table 4.1). Solutions were computed for particles originating from 11 different locations spanning the rotor inlet plane and for particle diameters ranging from 0.5 *to* $4.0\mu m$ in $0.5\mu m$ increments. Also, the path and velocity history of the fluid was calculated for fluid particles originating from the 11 rotor inlet locations. These solutions represent the optimum behavior of a seed particle.

The results were useful in explaining the discrepancies found between the CFD and PIV results. The investigation was carried out in two steps. First, the trajectories of the particles were studied and second, the Lagrangian velocity of the particles was compared to the Eulerian velocity of the fluid for the cases presented above.

Particle Trajectory

Figure 5-12 presents the trajectory of particles of different diameters originating from eleven circumferential locations spanning the inlet of the rotor passage. During the design of the present PIV experiment, the size of the seed particles was recognized as a critical design parameter. The most important criteria was to ensure that the seed particles behaved much like a fluid particle through a shock wave [7]. This is of course critical in a transonic turbine. Figure 5-12 shows however that the progressive acceleration of the flow through the rotor passage can be just as important. The most apparent effect of particle size on trajectory is seen on the downstream half of the suction side of the rotors. As postulated in Chapter 3, the large particles migrate away from the suction side as they flow down the passage. For $2.5\mu m$ diameter particles, the domain containing the pathlines of all the particles represents less than half of the passage width at the rotor exit. The velocity prediction is expected to

be greatly impacted by the inability of the seed particles to track the flow.

Particle Velocity History

In order to quantify the impact of particle size on PIV accuracy, the difference between the velocity of the particles and the velocity of the fluid along the particle pathline was computed for the eleven particle inlet positions presented above and for eight different particle sizes ($0.5\mu m$ to $4.0\mu m$). Figures 5-13 through 5-16 show four of these cases. Depending on the axial location of the particle and its size, the expected velocity deficit of the particle with respect to the flow is expected to be as high as 80 m/s for both the axial and the circumferential component of velocity. The magnitude of the velocity deficit corresponds very closely to the difference between the experimental results of PIV and the CFD solution.

This comparison of the particle model with the CFD results makes two things clear:

1. The highest difference between the two predictions occur after shock fronts. On Figures 5-13 through 5-16, this can be seen at axial locations $x \approx 0.037$ and $x \approx 0.047$. These correspond to the rotor trailing edge pressure side and suction side shocks. Their impact is important for both the axial and circumferential components of velocity. In particular, the pressure side shock has a predominant effect on the axial deficit as the flow is mostly axial in the rotor relative frame there, and is more pronounced for particle pathlines closer to the pressure side (Figure 5-16). Likewise, the suction side shock has a greater effect on the circumferential velocity because the flow is predominantly circumferential there and the velocity deficit associated with the shock is found to be greater for particle pathlines closer to the suction side.

2. The particle behavior is not only influenced by strong velocity gradients such as shocks. There is a velocity deficit associated with both the unsteadiness of the flow due to the stator wake at the inlet of the rotor passage and the constant acceleration of the flow as it progresses through the rotor passage. The first observation is more pronounced for the axial component of velocity as the flow is mostly axial at the rotor inlet; the second is more predominant for the circumferential velocity as the flow must turn through more than 120^o from inlet to exit. These two phenomena are illustrated in Figures 5-13 through 5-16.

5.4.2 Particle Dynamics in the Stator Vane Passage

In the previous section, the seed particle motion was modeled for particles entering the rotor passage with the same velocity as the surrounding fluid particles. To complete the investigation, it is important to test this assumption. If the particles were to enter the rotor passage with a velocity much different from that of the flow, including this feature in the model might be important in fine tuning the correlation between the size of the seed particles and the difference between the PIV and CFD results.

The particle motion model was implemented for the flow through the stator passage, using the same CFD solution as above as a baseline for the flow field and for four different stator inlet initial positions. Here again it was assumed that the particles entered the passage with the same velocity as the fluid. This assumption is justified because the stator inlet flow is uniform and the acceleration upstream of the turbine stage is gentle. The trajectories of the particles in the stator passage are presented in Figure 5-17. Figure 5-18 shows the velocity deficit for two different initial positions and five different particle sizes. The plots demonstrate two facts:

1. The large particles stray from the path of the fluid particles with a bias towards the pressure side of the stators, as for the rotor flow.

2. The velocity deficit is smaller than in the rotor passage, mainly because the velocities are smaller throughout most of the stator passage and because the turning of the flow is less. The maximum velocity deficit is of 30 m/s out of 300 m/s and occurs at the exit of the stator passage. The deficit decays as the particles flow through the interblade passage, and at the inlet of the rotor, the deficit is down to ± 10 m/s in the worst case scenario.

5.4.3 Influence of Particle Rotor Inlet Conditions

The rotor inlet velocity is of the order of 60 m/s in the rotor inertial frame. Consequently, the 10 m/s velocity deficit calculated above is a non negligible fraction of the inlet velocity. To quantify the error associated with assuming that the particles velocity at the rotor inlet matched the flow velocity, the particle motion was computed again, but this time, the initial

conditions included a 10 m/s axial velocity deficit and a -10 m/s circumferential velocity deficit for the particles - the worst case scenario calculated in Section 5.4.2. Figure 5-19 presents a comparison of the velocity deficit evolution for two cases: (1) the particles are initially at the flow velocity and (2) the particles have an initial velocity deficit as described above. The effect of the initial condition on the velocity history of the particles was found to be negligible. The velocity deficit decays very quickly at the rotor inlet, and the downstream particle dynamics are unaffected. It can be concluded that the assumption of Section 5.4.1 is well founded and that the results are good predictors of the seed particle motion.

5.4.4 Particle Size Estimation

The PIV experiment presented in this thesis was designed to use particles with a diameter of 0.5 $\mu m \pm 0.1$ μm. Had this been the case, the particles would have tracked the flow as demonstrated in Section 5.4.1. The fact that there is a wide spread in the PIV results suggests that particles of larger diameter are observed on the images. This hypothesis was tested in two ways, first by comparing the density of the particles in the tank and in the PIV images and second by comparing the trajectory of the particles on the images to the predictions of the model.

Seed Particle Density

Before each PIV test, the particle diameter distribution was measured in the supply tank using a laser aerosol spectrometer. For the test corresponding to image 2651, the seed particle diameter distribution had a mean of 1.10 μm and standard deviation of 0.6 μm (cf. Figure 5-1). The density was designed to be one particle/mm^3 in the supply tank. The supply tank initial pressure is a factor of 1.2 greater than the pressure in the turbine stage at the instant of the picture. The particle density is therefore expected to be 1.2 times smaller in the image, yielding 825 $particles/mm^3$ in the turbine passage. The PIV data covers an area of approximately 16 cm^2 and the effective width of the laser light sheet is assumed to be 1 mm. This implies that the image should contain 1320 particles. 500 particles were identified on average, which corresponds to 38% of the particles. Under the assumption that larger particles can be observed more easily than smaller ones, the upper

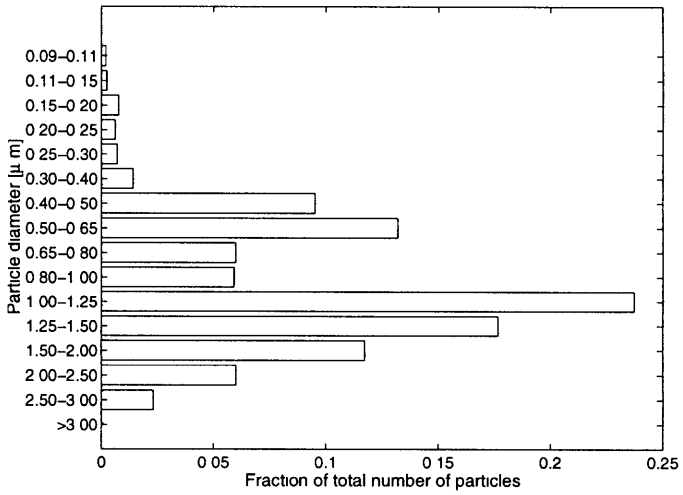

Figure 5-1: Styrene particle diameter distribution for a typical PIV test (image 4001).

38% of a Gaussian distribution of particle size corresponds to particles of diameter greater than $\mu + 0.3\sigma$ or 1.3 μm.

Particle Position Envelope

The minimum particle size was also estimated by comparing the position of the particles on the PIV images with the position of particles of different sizes as predicted by the model. The fluid streamline originating at $x = 0.006$ and $y = -0.0125$ was found to follow the contour of the suction side of the rotor blade. Hence, by plotting the path of particles of different sizes, originating from this same position, an envelope for the possible position of the particles in the pictures can be obtained. Figure 5-2 shows the particle trajectory for five diameters and the position of all the PIV particles in image 2651. No particles were identified beyond the boundary defined by the path of a $1.5\mu m$ particle. This suggest that the smallest particle size captured on the PIV images was $1.5\mu m$. This is consistent with the result found above.

5.5 Evaluation of PIV Results

In light of the analysis above, the comparison of the CFD solution with the PIV results can be revisited assuming the diameter of the smallest particles is $1.5\mu m$. Hence, a velocity deficit on the order of 10 to $40 m/s$ is expected throughout the rotor passage. To estimate

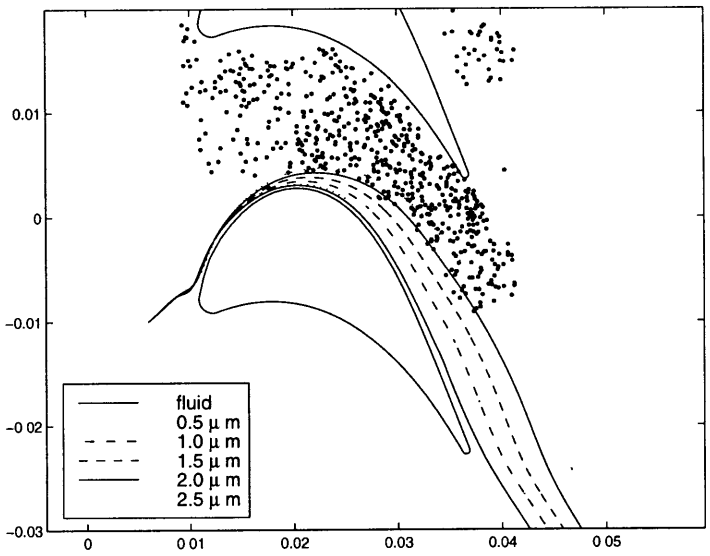

Figure 5-2: Particles of different diameters following the suction side of the rotor blade and comparison with PIV.

if the particle dynamics are responsible for the discrepancies found in Section 5.2, the PIV velocity results were compared to the velocity of the fluid and the velocity of different size particles as predicted by the model. Figures 5-20 and 5-21 show the envelope of velocities for particles originating from $(x = 0.006, y = 0)$ and $(x = 0.006, y = 0.01)$ along with the PIV solutions along the fluid streamline. For the axial velocity the particle velocity deficit fails to explain all the features of the calculation. In the circumferential direction, however, the envelope formed by the fluid velocity history and the $2.5\mu m$ particle velocity history successfully bounds most of the PIV results, in particular within the rotor passage and at the rotor exit.

Since the particle dynamics model was successful at explaining the discrepancies between the CFD and PIV in the circumferential direction, it is safe to assume that the differences in the axial direction cannot be blamed entirely on experimental error in the PIV results. Looking at the evolution of the flow through the rotor passage offers an explanation for the above contradiction. The circumferential component of the flow is only subject to a fairly constant acceleration. By contrast, the axial flow is affected by the stator wakes and multiple shocks and successively accelerates and decelerates (cf. Figures 5-20 and 5-21). These features are difficult to accurately predict and might be complemented by random unsteadiness in the stator wakes, which UNSFLO is not capable of calculating. Hence,

the disagreement between CFD and PIV could partly result from the numerical model predicting only periodic unsteadiness.

Abhari arrived at similar conclusions when comparing heat transfer experimental measurements in the ACE turbine stage with theoretical predictions with UNSFLO [1]. Time-resolved Nusselt number comparisons showed results with the same order of magnitude, but the two solutions often exhibited a phase shift. In addition, the comparison suggested that random unsteadiness may play an important role in establishing the patterns of the flow.

5.6 Chapter Summary

In this chapter, the PIV results for two images with similar rotor/stator index were compared to the CFD solution corresponding to the experimental conditions. Four important conclusions were drawn out of this comparison:

1. The PIV and CFD results were within the same order of magnitude and followed the same trends across the rotor passage. However the PIV solution covered a wide band of velocity and disagreed with CFD by as much as 60%.

2. Recognizing the importance of the size of the seed particles in the accuracy of the PIV predictions, a particle dynamics model was built. The insight from the model was that particle size should be a critical factor in the design of a PIV experiment. The velocity deficit is proportional to the square of particle size. Hence, significant errors both in trajectory predictions and velocity magnitude predictions can result from using oversized particles.

3. The PIV experiment was designed to use 0.5 μm particles. In reality, the mean size of the particles was measured to be 1.1 μm in the supply tank and the smallest particle captured by the optics was estimated to be approximately 1.5 μm in diameter. This shortcoming of the experiment was responsible for a large fraction of the PIV/CFD disagreement.

4. The particle motion model successfully explained the difference between the CFD and PIV results for the circumferential component of velocity. In contrast, the predictions

for the axial velocity were not as satisfying. This suggests that the CFD model is not sufficiently flexible to accurately calculate the unsteadiness in the rotor passage.

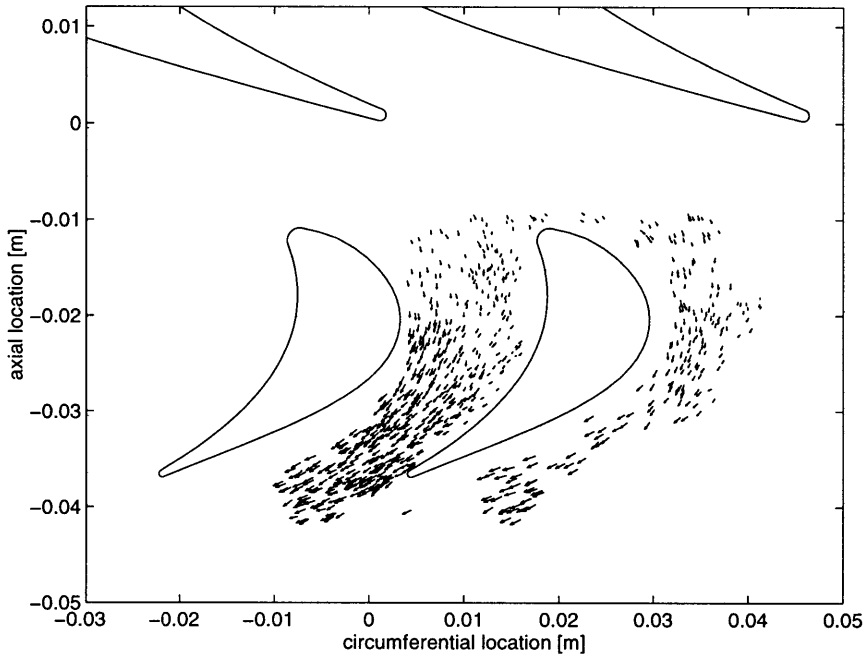

(a) PIV flow field (image 2651)

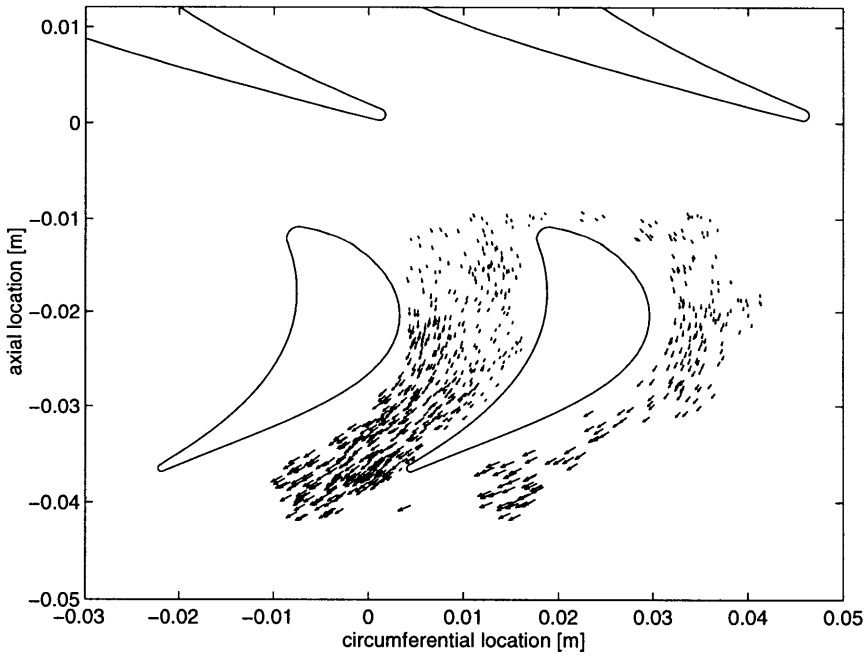

(b) CFD solution of the flow field at the location of the PIV vectors

Figure 5-3: Velocity flow field in the turbine passage using PIV and CFD.

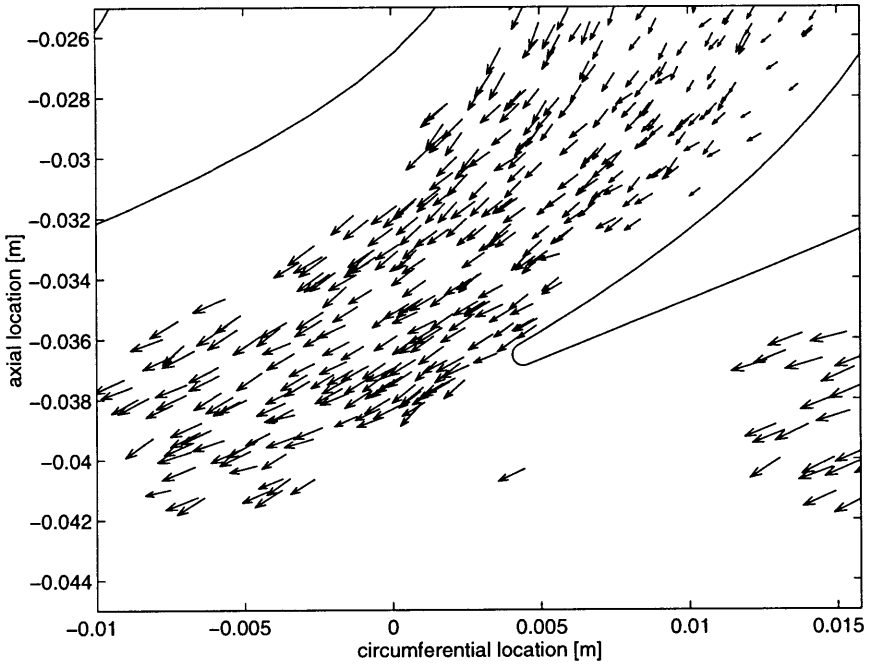

(a) PIV flow field (image 2651)

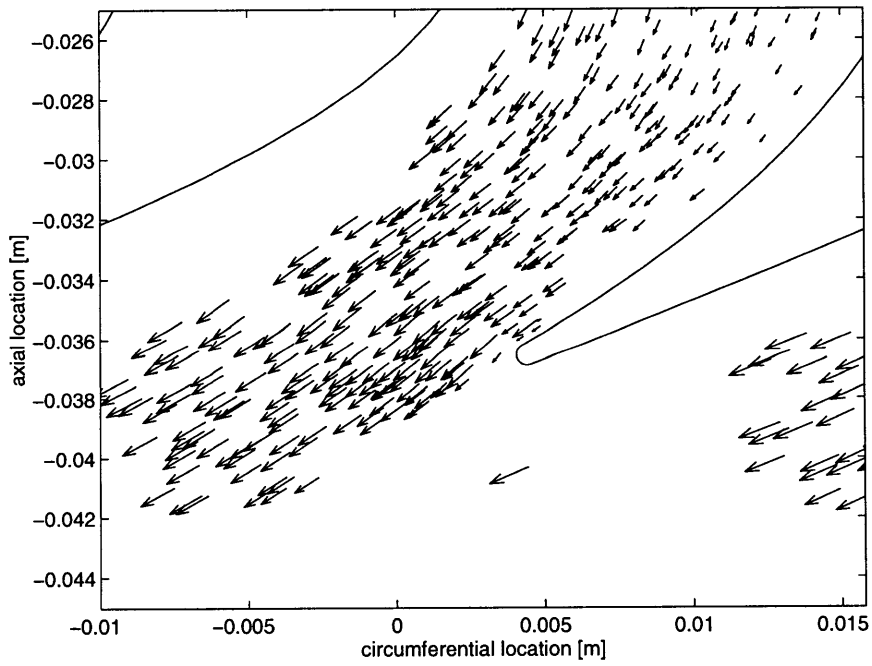

(b) CFD solution of the flow field at the location of the PIV vectors

Figure 5-4: Close-up of rotor exit flow solution using PIV and CFD.

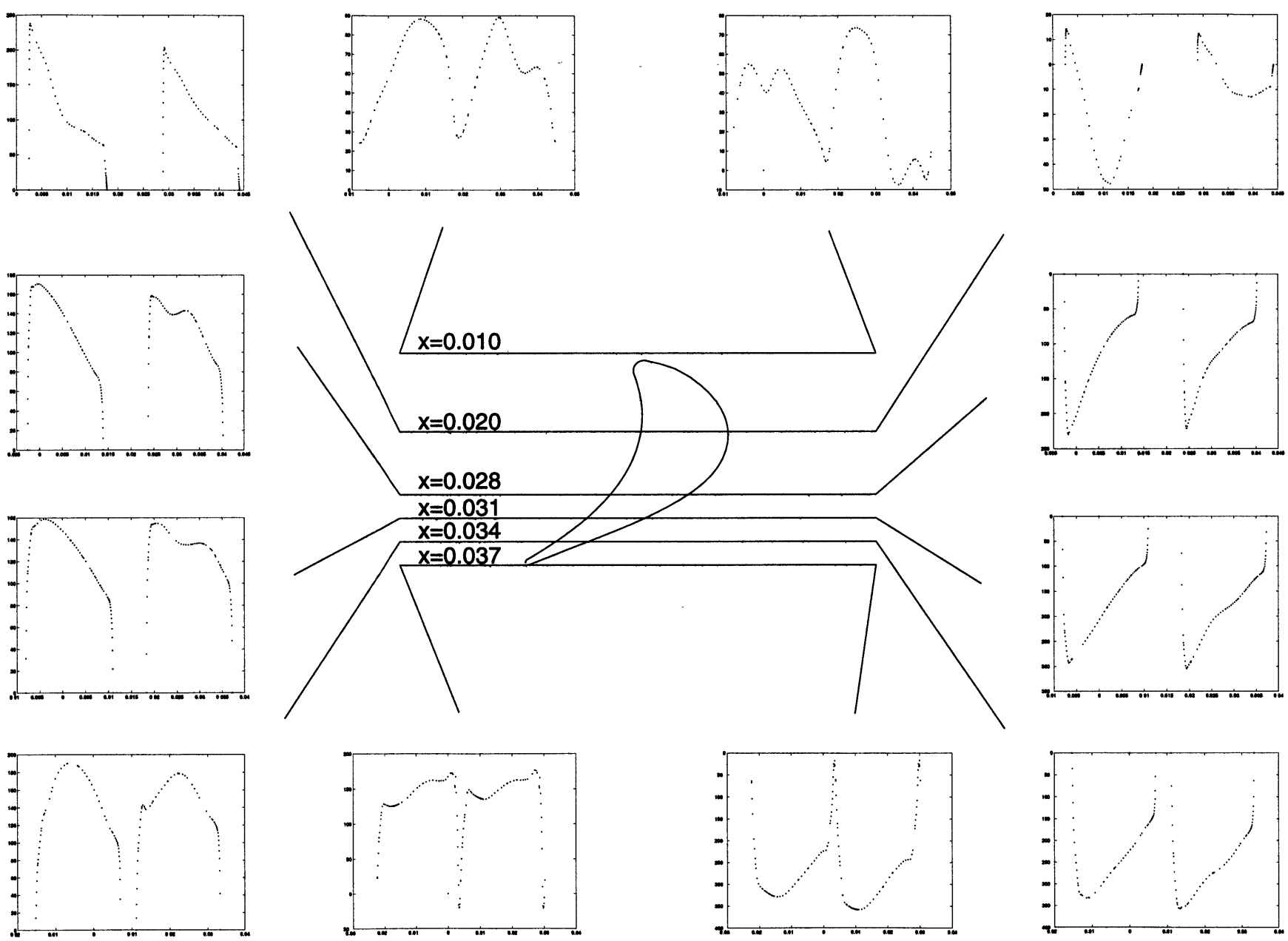

Figure 5-5: Composite diagram of the axial and circumferential velocities in the rotor passage (image 2651).

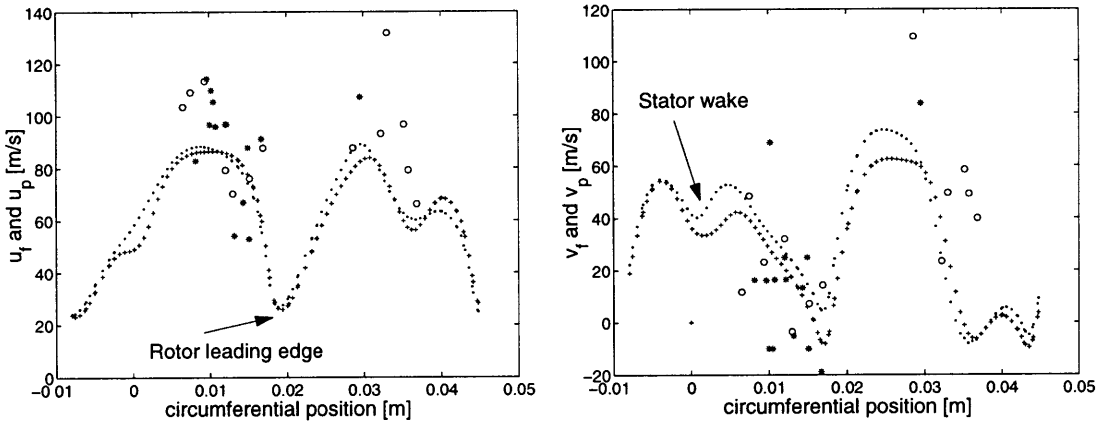

Figure 5-6: Axial and circumferential CFD velocity profiles at axial location $x = 0.010$ and comparison with PIV (rotor relative frame; wheel speed = 187.2 m/s).

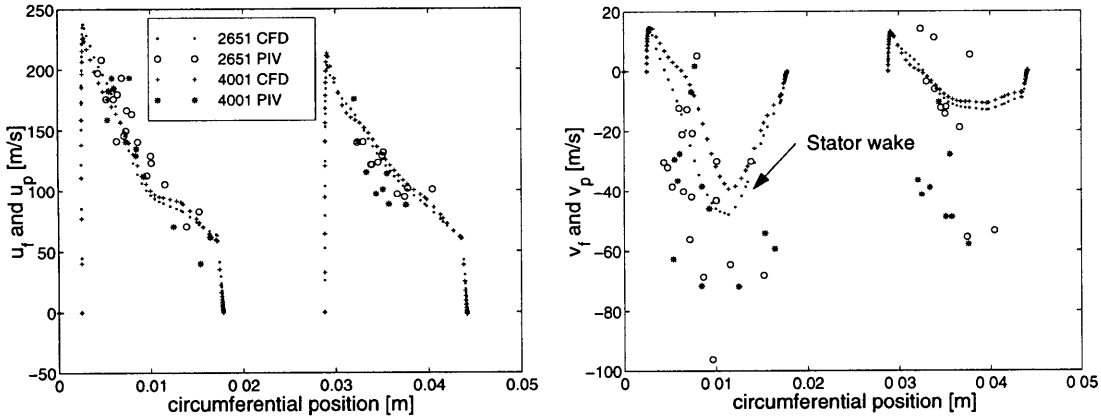

Figure 5-7: Axial and circumferential CFD velocity profiles at axial location $x = 0.020$ and comparison with PIV (rotor relative frame; wheel speed = 187.2 m/s).

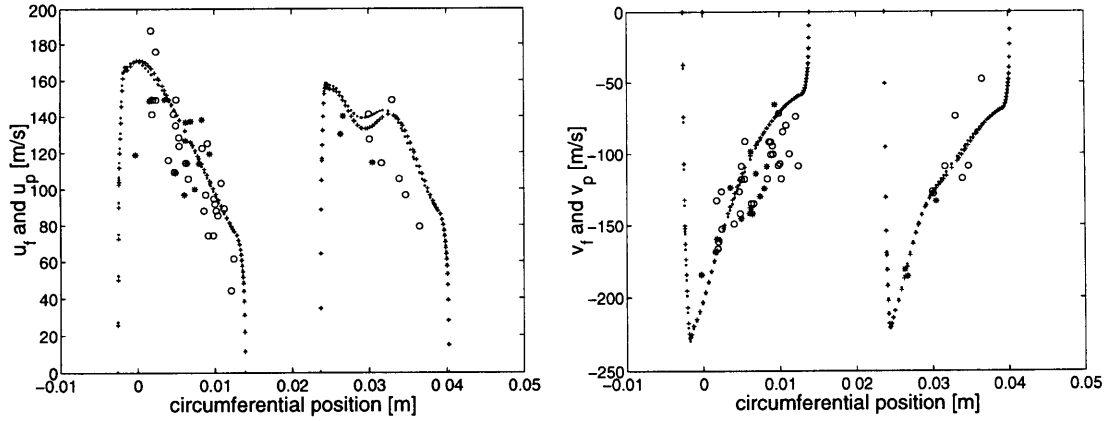

Figure 5-8: Axial and circumferential CFD velocity profiles at axial location $x = 0.028$ and comparison with PIV (rotor relative frame; wheel speed = 187.2 m/s).

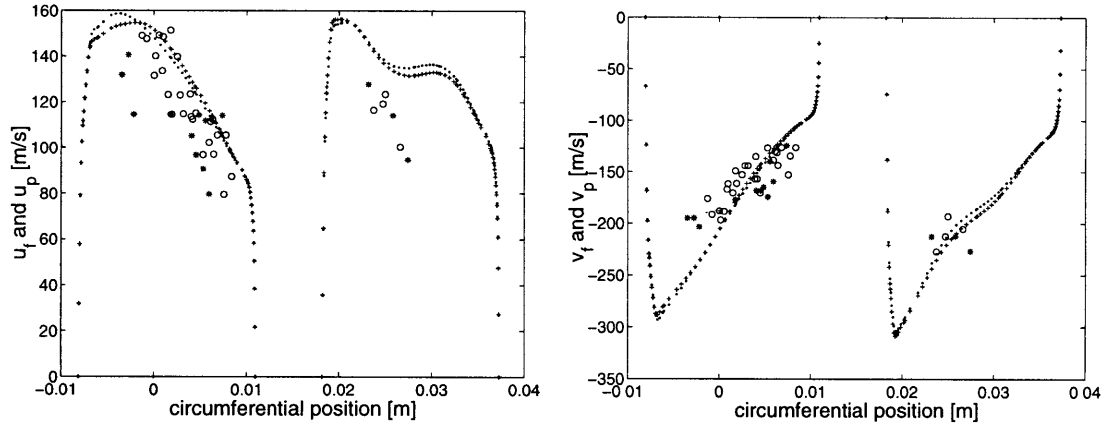

Figure 5-9: Axial and circumferential CFD velocity profiles at axial location $x = 0.031$ and comparison with PIV (rotor relative frame; wheel speed = 187.2 m/s).

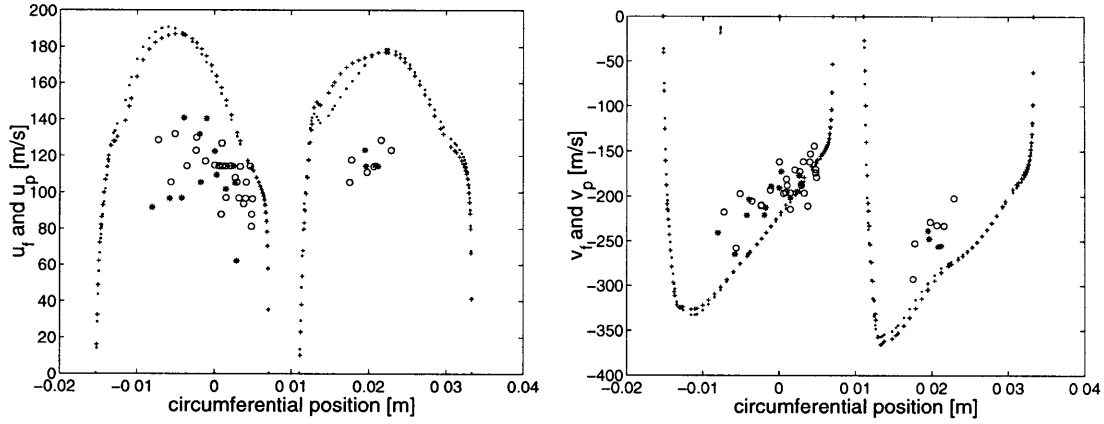

Figure 5-10: Axial and circumferential CFD velocity profiles at axial location $x = 0.034$ and comparison with PIV (rotor relative frame; wheel speed = 187.2 m/s).

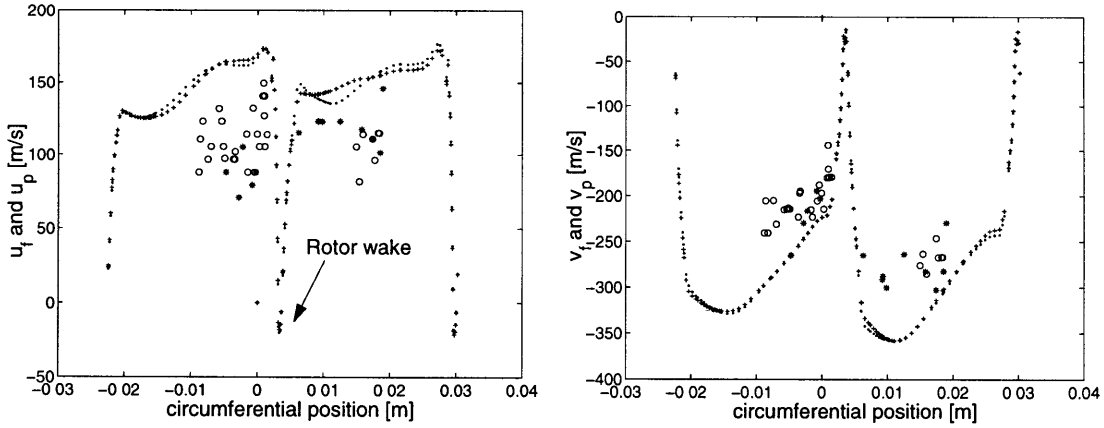

Figure 5-11: Axial and circumferential CFD velocity profiles at axial location $x = 0.037$ and comparison with PIV (rotor relative frame; wheel speed = 187.2 m/s).

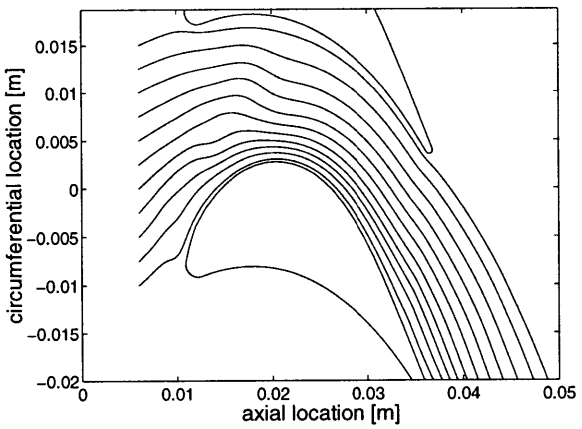

(a) Fluid particles

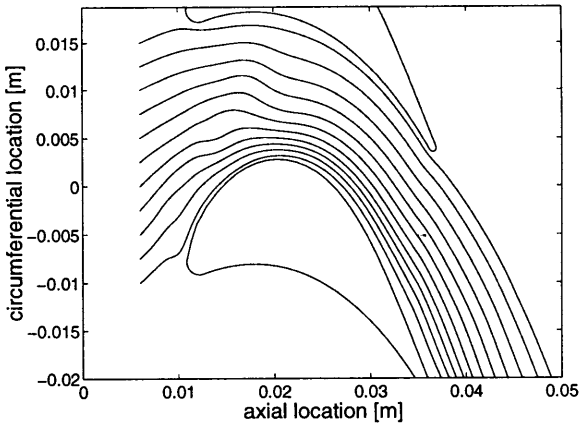

(b) $d = 0.5\mu m$

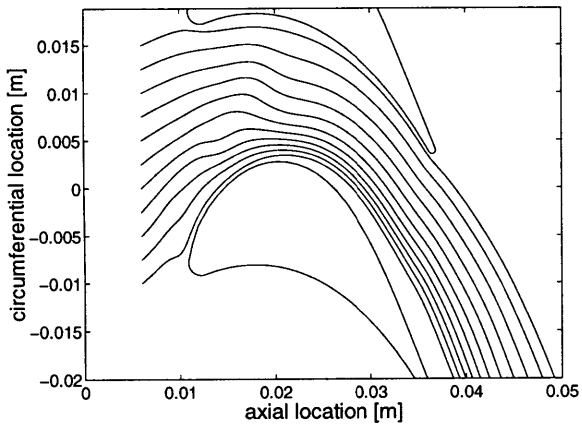

(c) $d = 1.0\mu m$

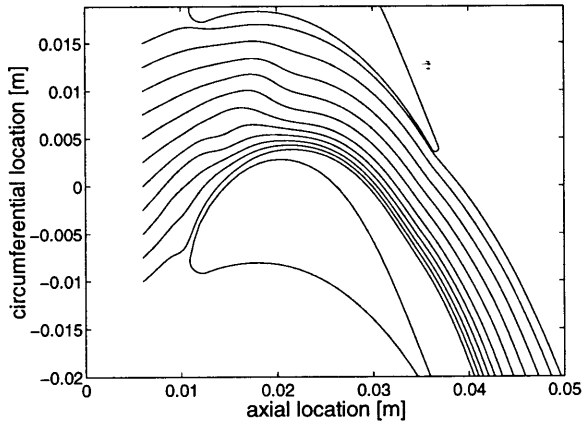

(d) $d = 1.5\mu m$

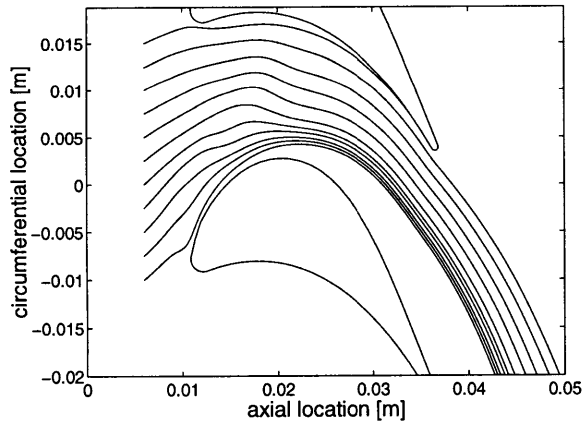

(e) $d = 2.0\mu m$

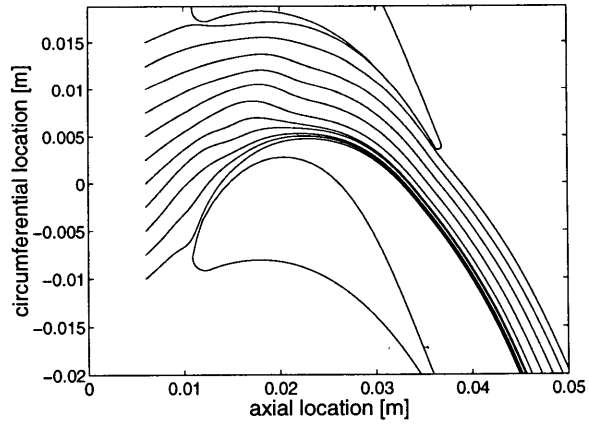

(f) $d = 2.5\mu m$

Figure 5-12: Fluid streamlines and particle trajectories in the rotor passage. Particle diameters range from $d = 0.5\mu m$ to $d = 2.5\mu m$.

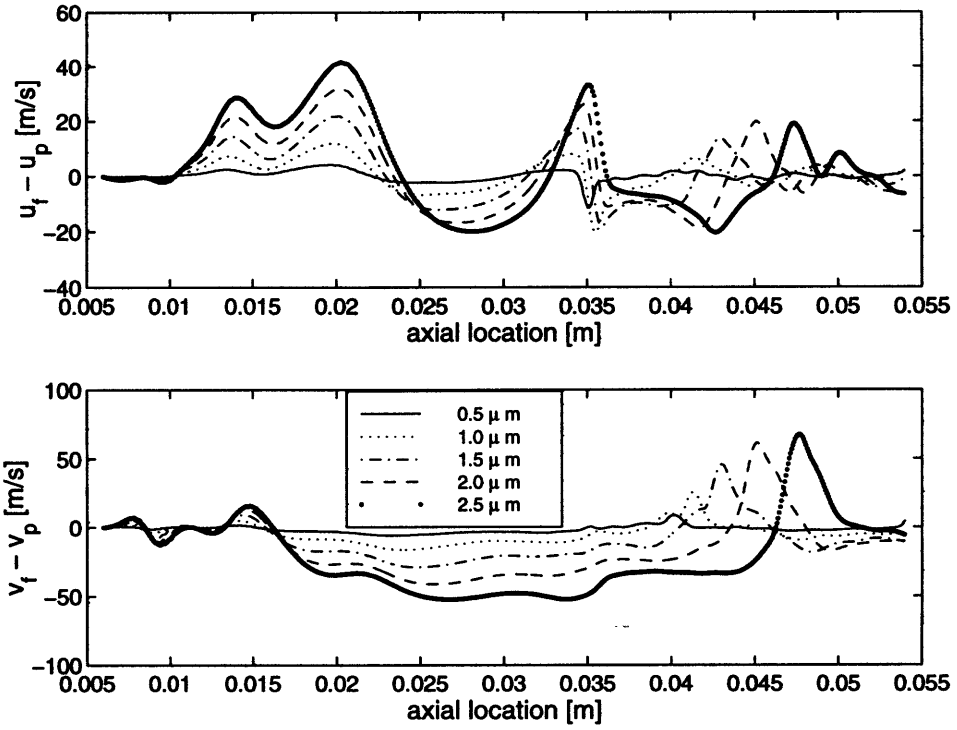

Figure 5-13: Axial and circumferential velocity deficit for different size particles originating from $x = 0.006$ and $y = -0.005$.

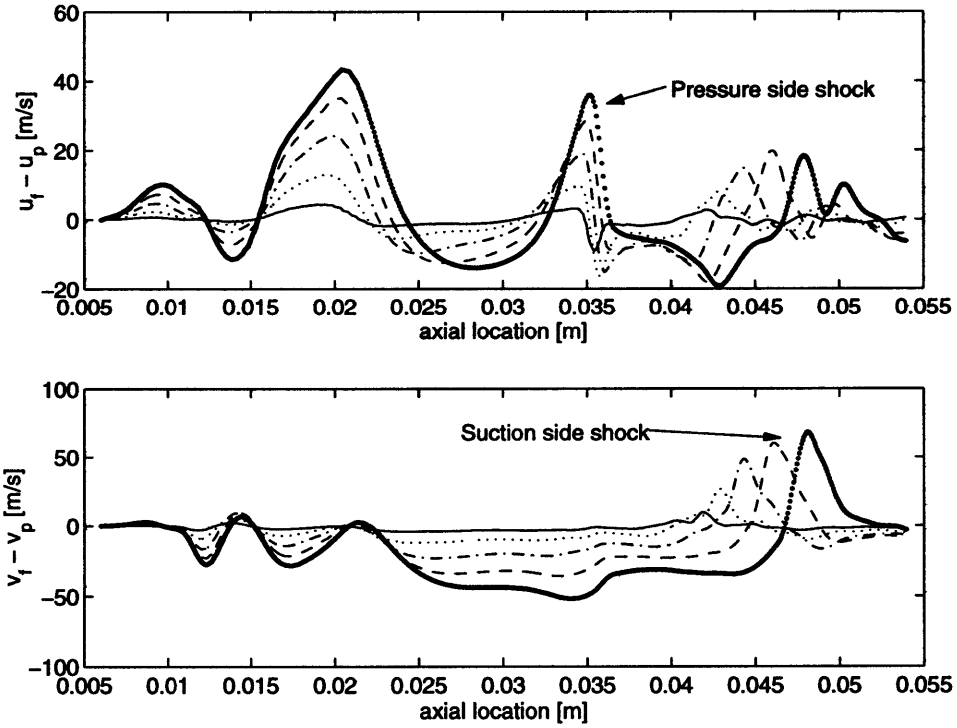

Figure 5-14: Axial and circumferential velocity deficit for different size particles originating from $x = 0.006$ and $y = 0$.

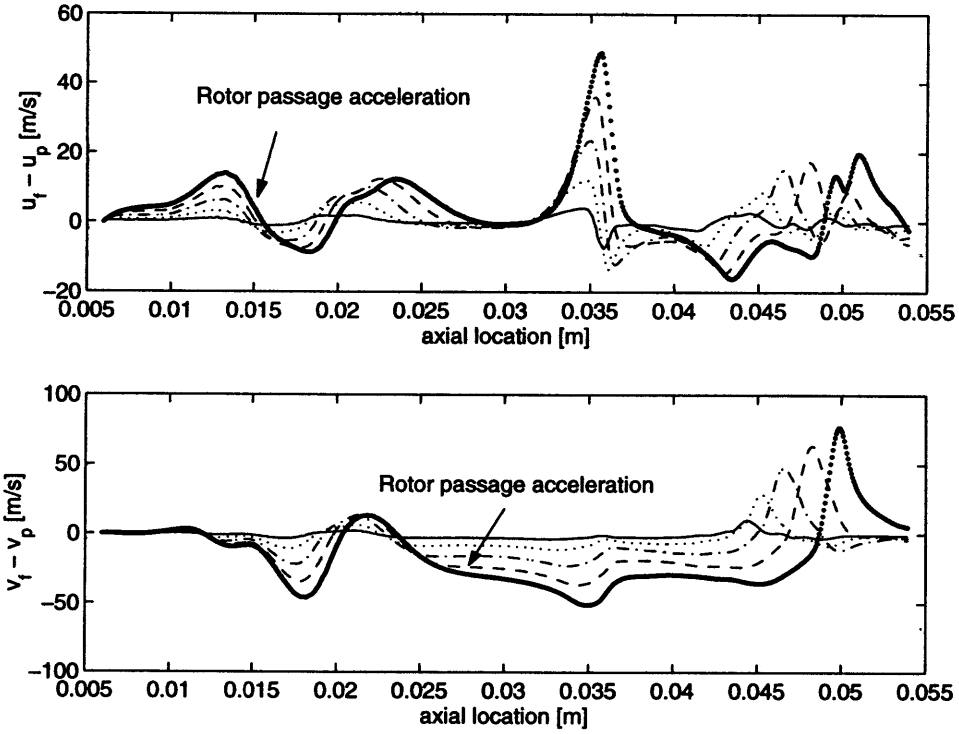

Figure 5-15: Axial and circumferential velocity deficit for different size particles originating from $x = 0.006$ and $y = 0.005$.

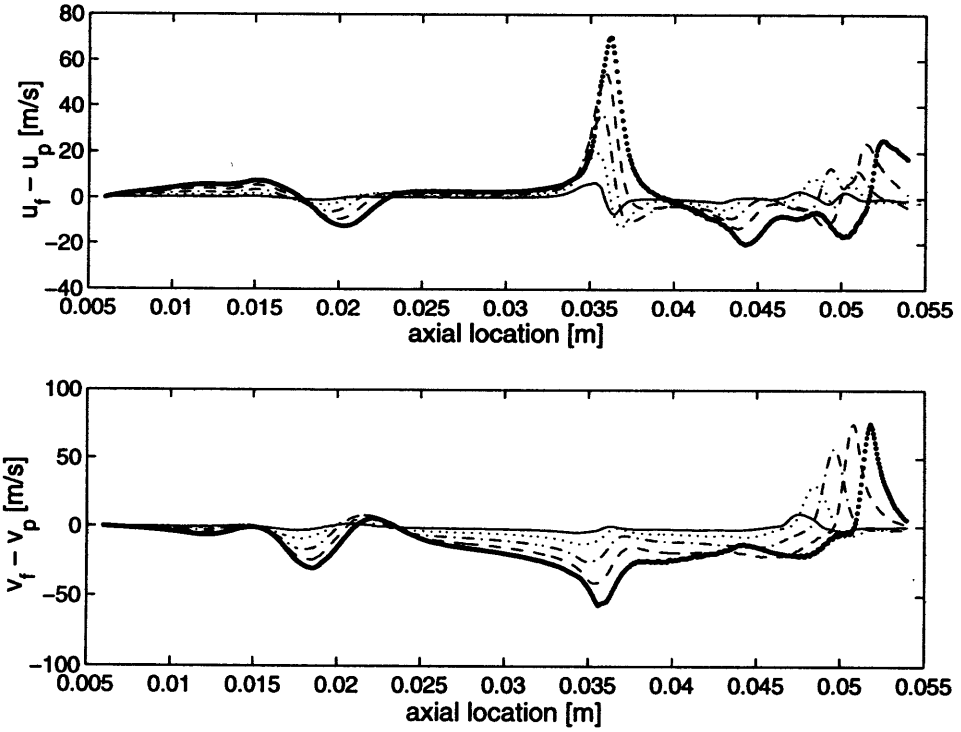

Figure 5-16: Axial and circumferential velocity deficit for different size particles originating from $x = 0.006$ and $y = 0.01$.

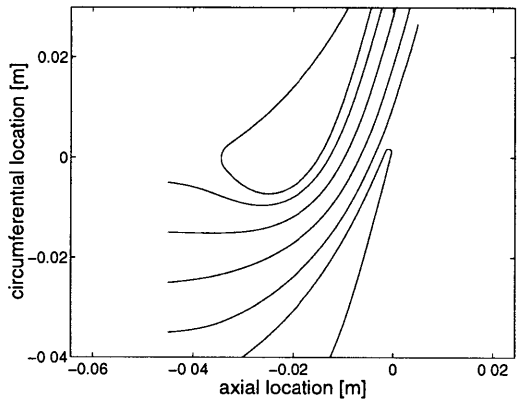

(a) Fluid particles

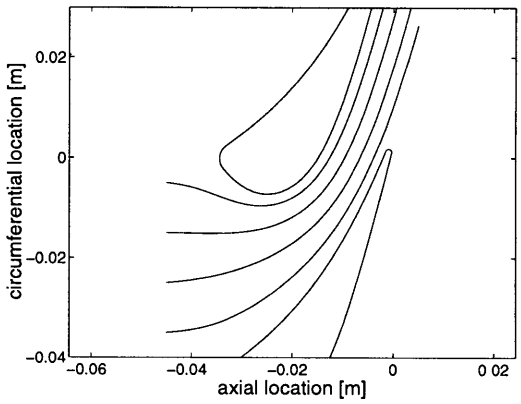

(b) $d = 0.5\mu m$

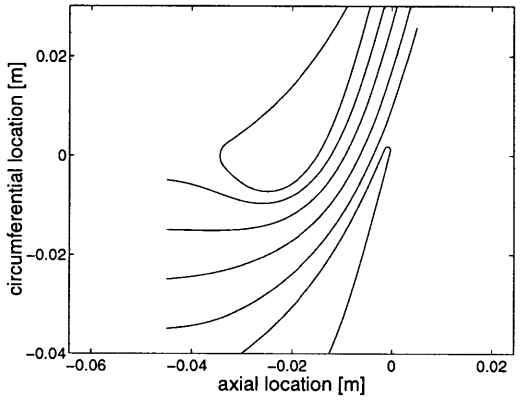

(c) $d = 1.0\mu m$

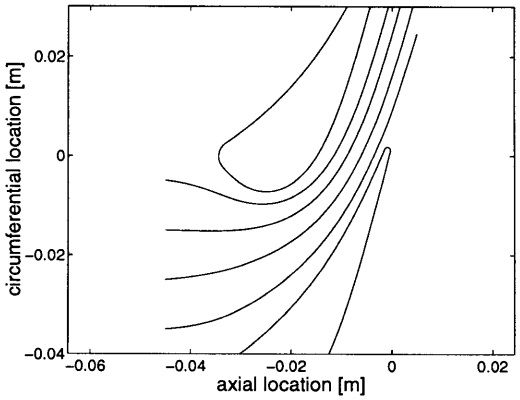

(d) $d = 1.5\mu m$

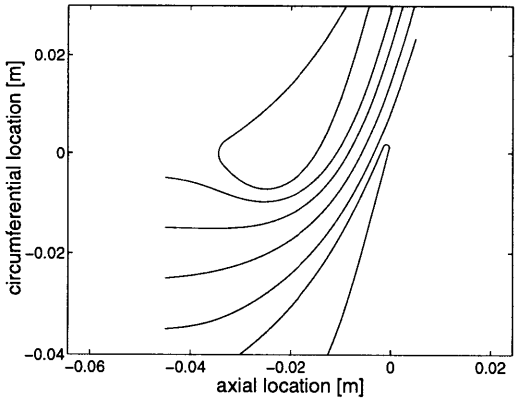

(e) $d = 2.0\mu m$

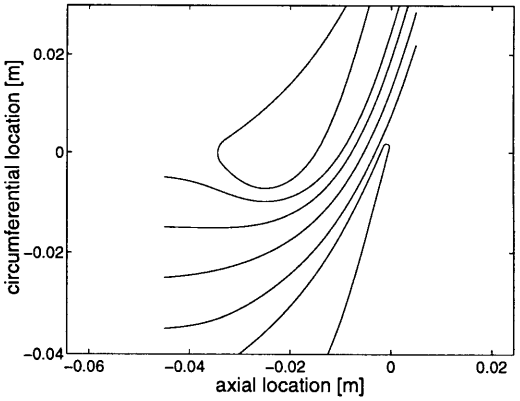

(f) $d = 2.5\mu m$

Figure 5-17: Fluid streamlines and particle trajectories in the stator passage. Particle diameters range from $d = 0.5\mu m$ to $d = 2.5\mu m$.

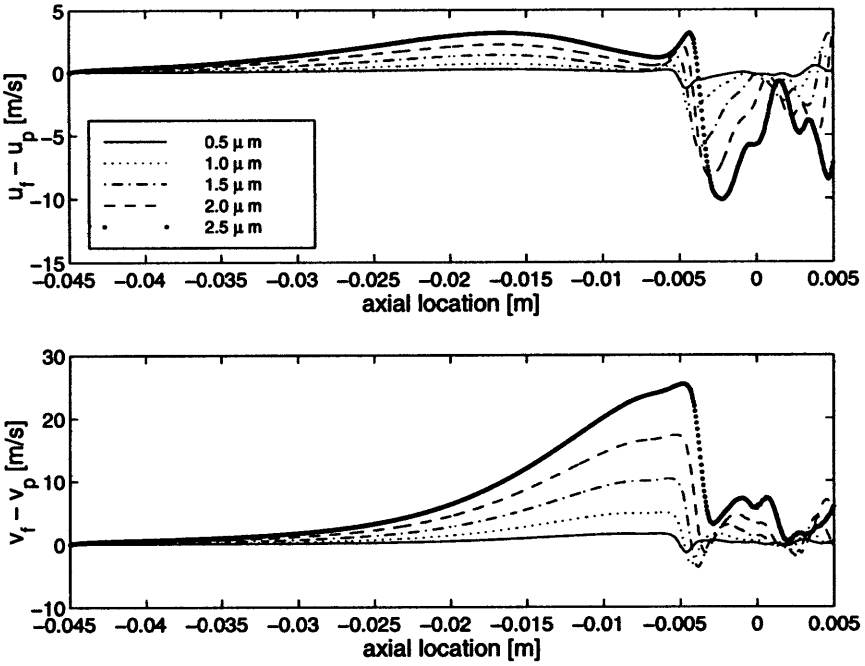

(a) Particle originating from $x = -0.045$ and $y = -0.025$

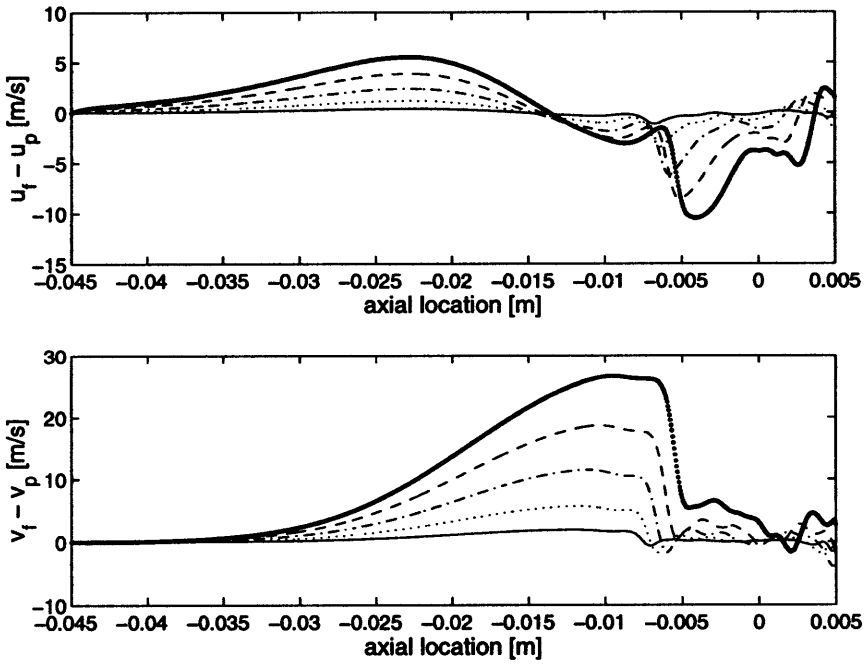

(b) Particle originating from $x = -0.045$ and $y = -0.015$

Figure 5-18: Axial and circumferential velocity deficit for different size particles in the stator passage.

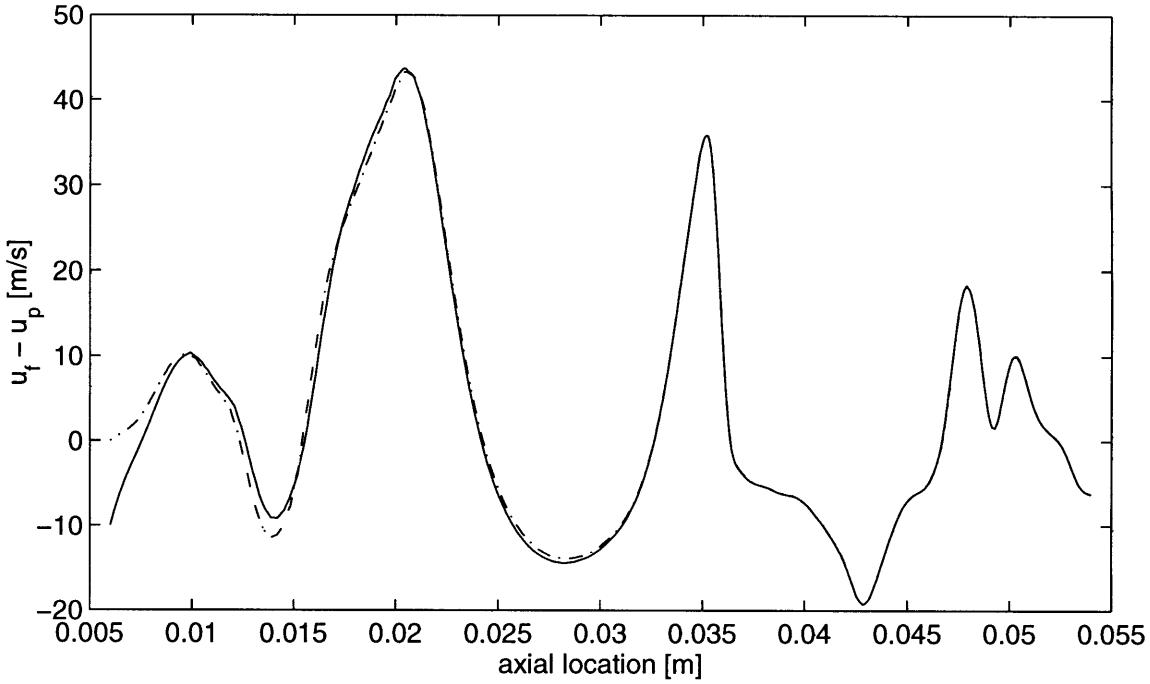

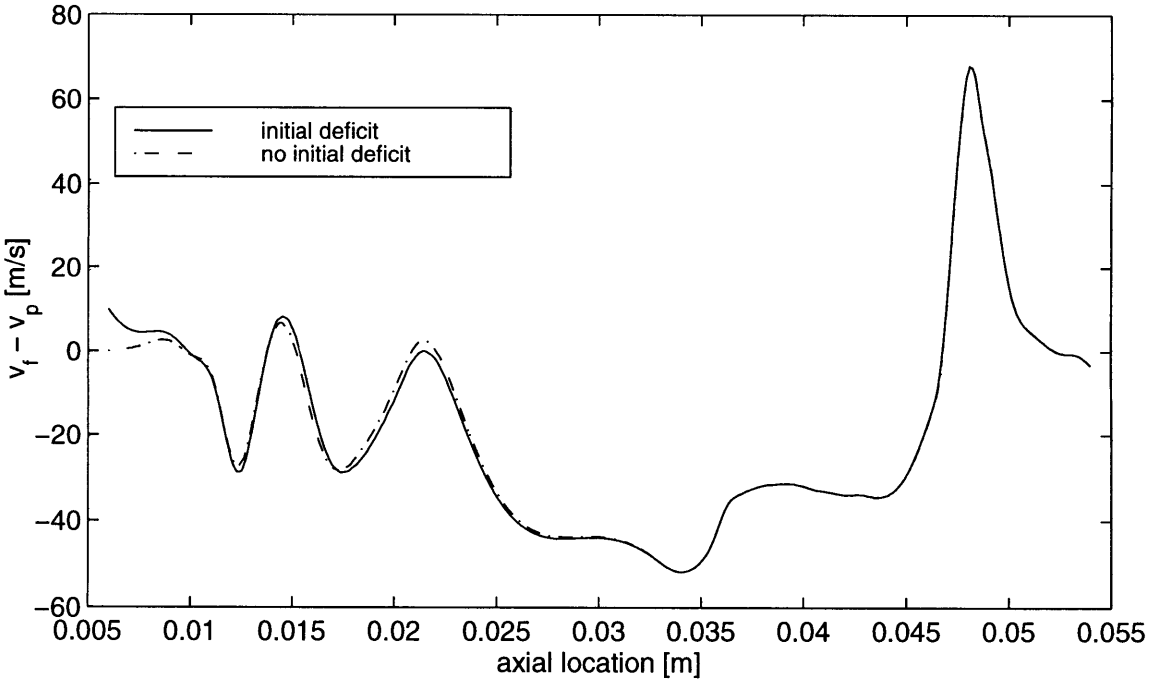

Figure 5-19: Axial and Circumferential velocity deficit in the rotor passage for a $2.5\mu m$ particle originating from $x = 0.006$ and $y = 0$. Two cases are presented: no initial deficit and initial velocity deficit of $(u_f - u_p)_{initial} = -10\ m/s$ and $(v_f - v_p)_{initial} = 10\ m/s$.

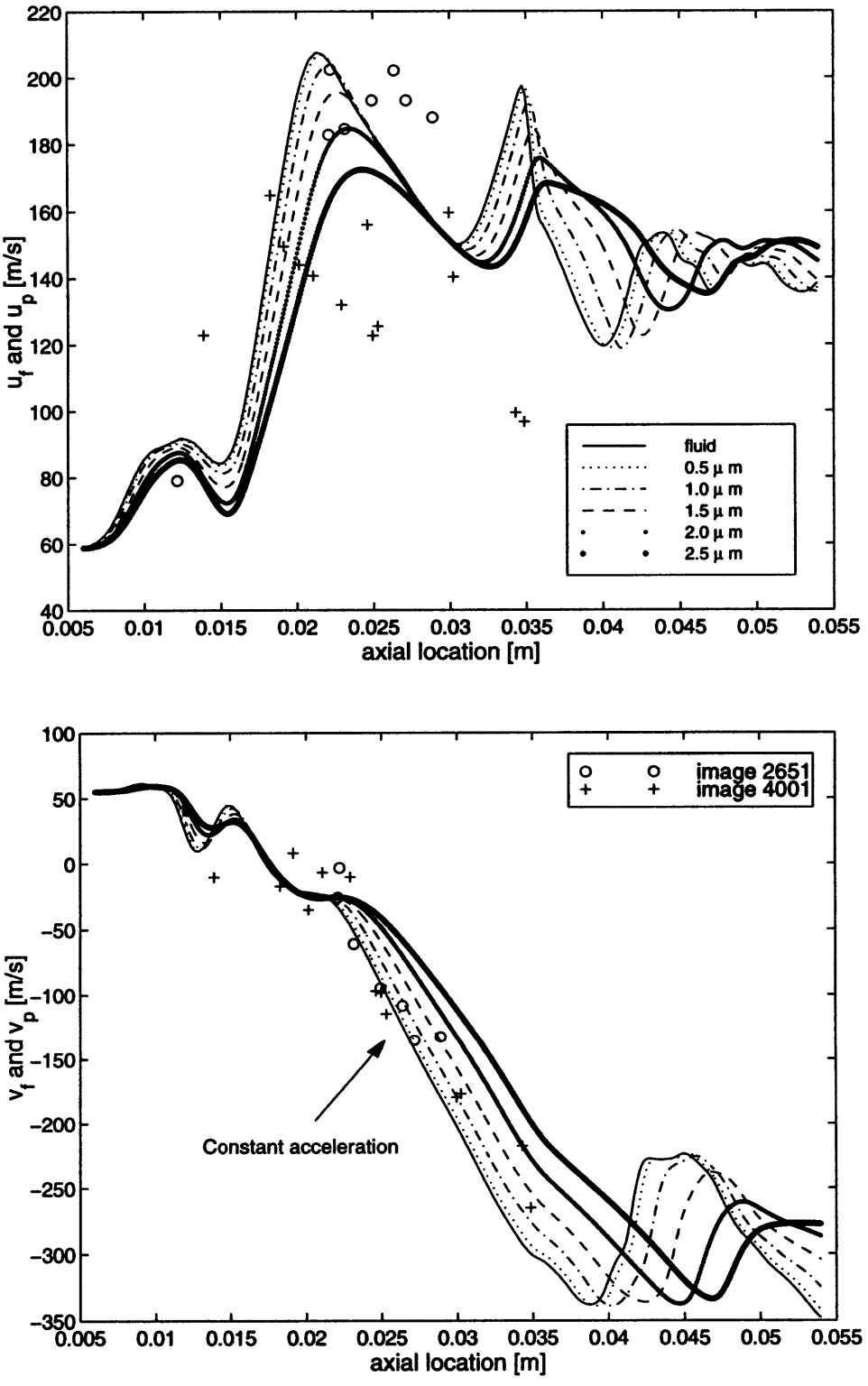

Figure 5-20: Axial and circumferential velocity history in the rotor passage for different size particles originating at $x = 0.006$ and $y = 0$ and comparison with PIV.

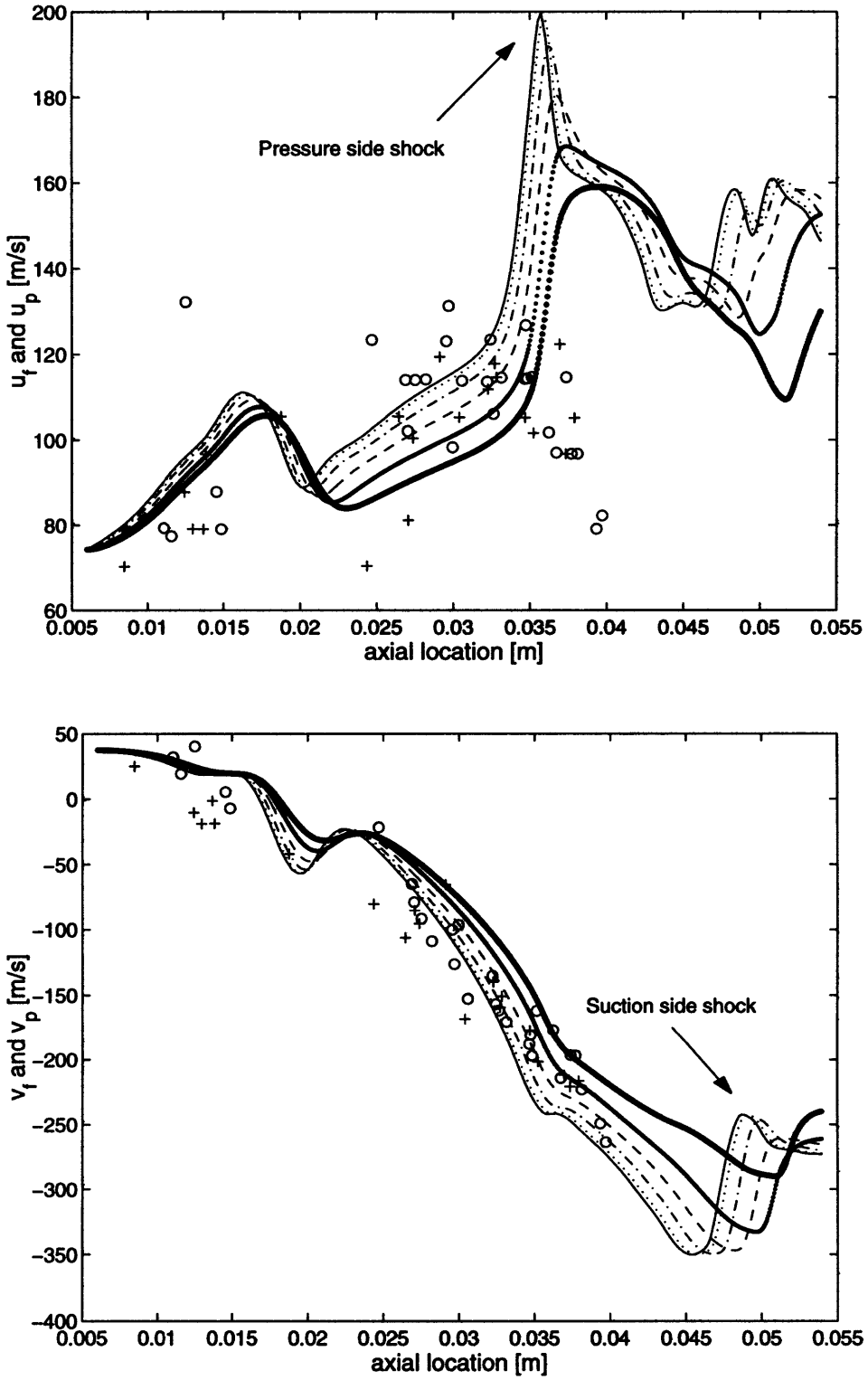

Figure 5-21: Axial and circumferential velocity history in the rotor passage for different size particles originating at $x = 0.006$ and $y = 0.01$ and comparison with PIV.

CHAPTER 6

CONCLUSIONS

6.1 Summary of the Research

This thesis presented research aimed at improving the flexibility and accuracy of turbine testing in a blowdown environment. The two centers of focus dealt with designing a high accuracy differential pressure probe and with demonstrating the feasibility and validity of particle image velocimetry in a blowdown turbine environment:

1. Three differential pressure probes were designed and complemented with three total pressure and temperature probes. The measurements were used to calculate Mach number and mass flow in the plenum located upstream of the turbine. These calculations were compared with measurements of mass flow by Keogh using a Venturi nozzle at the turbine exit. The comparison served to validate the model of the blowdown turbine dynamics used to correct the Venturi measurements and calculate the actual turbine mass flow.

2. A particle image velocimetry experiment was designed and implemented in the MIT Blowdown Turbine. The low-density PIV images were reduced using a particle-tracking algorithm and auto-correlation of particle pairs to calculate particle velocity.

   The flow measured using PIV in the Rolls-Royce ACE turbine stage was also modeled using the 2-D coupled Navier-Stokes/Euler UNSFLO code. Solutions were compared for different boundary conditions and for different rotor/stator indices. Shock patterns were identified in the rotor passage.

The PIV results were compared to the unsteady CFD solutions. A model of the motion of seeding particles in the turbine stage was developed and the results were used to explain some of the differences between CFD and PIV.

6.2 Contributions of the Work

The most significant contributions of this thesis can be summarized as follows:

1. The concept of a differential pressure probe was demonstrated in a blowdown environment and the instrument was successfully used in conjunction with total pressure and temperature probes to infer Mach number and mass flow per unit effective area within 1% uncertainty.

2. The first set of PIV measurements in a turbine rotor have been rigorously compared with CFD calculations and with numerical predictions of seed particle motion.

3. The choice of the seeding particles in a PIV experiment was found to be the most critical parameter governing the accuracy of the flow visualization method. A factor of five in the size of the particles can bring the uncertainty of the measurement from a few percents to over 100%.

Additional conclusions included in this thesis are as follows:

- The mass flow calculations successfully validated the measurement correction proposed by Keogh for the measurement of mass flow in the MIT Gas Turbine Facility using a Venturi nozzle [24].

- PIV can be successfully implemented in a fully scaled rotating turbine. Furthermore, the concept was demonstrated in a transient short-duration blowdown experiment.

- In the ACE turbine, the test conditions and rotor/stator position have substantial influence on the aerodynamic properties of the flow and it was found that PIV images with different conditions should not be aggregated in general.

- The random unsteadiness present in the rotor passage flow was found to be significant. Both PIV and comparisons ran by Abhari [1] showed that modeling periodic unsteadiness only was not sufficient to fully predict the rotor inlet flow.
- For the flow through the ACE turbine, 0.5 μm diameter seeding particles have optimum flow tracking capabilities

6.3 Recommendations for Future Work

Based on these conclusions, additional research is suggested in the following areas:

1. The oscillations associated with the sudden expansion at the beginning of a blowdown test should be studied so that they can be properly accounted for in the differential pressure measurements.
2. The next generation of differential pressure probes should use a more rugged pressure sensor without sacrificing accuracy. The sensor should be calibrated using a multi-point calibration as the Kulite sensor non-linearity was found to be a primary source of uncertainty in the measurement of differential pressure.
3. The PIV solutions to the ACE turbine flow should be compared to the results of a 3-D computational model to quantify the magnitude of the 3-dimensional effects and the error associated with a 2-D PIV solution of the flow.
4. Subsequent PIV experiments should use 0.5 μm particles as both experimental [8] and numerical investigation demonstrates their ability to track the flow. These small particles will be hard to capture on the optical medium and the field of the image should consequently be reduced. A field of view of one rotor passage would be sufficient for analysis.
5. It is useful to synchronize the timing of the PIV laser firing with the frequency of the rotor so that images with the same rotor/stator index and the same test conditions can be compared.

Appendix A

Aerodynamic Measurement Error Analysis

A.1 Introduction

In this appendix, the uncertainty levels of experimental measurements presented in Chapter 2 are discussed. The errors in the dynamic and stagnation pressures and stagnation temperature are studied and used to estimate the propagated uncertainty in Mach number and mass flow calculations.

A.2 Measurement Error

All measurements have errors, defined as the differences between the measured values and the true physical value of the quantity [4]. The specific causes of error in an experiment can be many. In spite of this diversity, the total error of a measurement, δ_k, can be expressed in term of two classes of errors: the bias component of error, β, and the random or precision component of error, ϵ_k, such that:

$$\delta_k = \beta + \epsilon_k \tag{A.1}$$

A.2.1 Precision Error

Precision errors are observed in repeated measurements of the same quantity. The results of the different measurements do not agree because of numerous sources of error such as certain human errors, disturbances in the equipment, fluctuations in experimental conditions and insufficient measuring system sensitivity. For N measurements of the same quantity, there is a distribution of the precision errors with standard deviation σ. For a normal error distribution, the interval $\mu \pm 2\sigma$ includes 95% of the total scatter of the measurements. The larger the standard deviation, the larger the scatter of the measurements. To estimate the standard deviation, the statistic S, called the precision index, is calculated. S is defined as:

$$S = \left[\sum_{k=1}^{N}(X_k - \bar{X})^2\right]^{1/2} \cdot \left[\frac{1}{N-1}\right]^{1/2} \tag{A.2}$$

where $\bar{X}$ is the average value of the measurements X_k, and is given by:

$$\bar{X} = \frac{1}{N}\sum_{k=1}^{N} X_k \tag{A.3}$$

Hence, the precision error can be reduced by averaging several measurements and using the average instead of any of the individual measurements:

$$S_{\bar{X}} = \frac{S}{\sqrt{N}} \tag{A.4}$$

A.2.2 Bias Error

The bias error is the component of error that remains constant during a measurement and is common to successive measurements of the same quantity. Bias errors are caused by calibration errors, recurring human errors, defective equipment and limitations of the system resolution. They are very difficult to quantify, but a bias limit B should be estimated as an upper limit to the bias error β.

A.2.3 Degrees of Freedom in Error Sources

Measurement errors originate from numerous sources but also occur at different stages of a measurement: during calibration, data acquisition and data reduction for example. Elemental precision and bias errors (i) can be combined for different categories of errors (j):

$$S_j = \left[\sum_{i=1}^{n} S_{ij}^2\right]^{1/2} \tag{A.5}$$

Then, the precision index for the overall measurement is calculated as the root-sum-square of the elemental precision indices for the different categories:

$$S_{measurement} = \left[\sum_{j=1}^{m} S_j^2\right]^{1/2} \tag{A.6}$$

A.3 Propagation of Uncertainty

In an experiment, quantities are often measured to calculate other quantities [5]. The uncertainty associated with each measurement creates an uncertainty in the calculated quantity. For a calculation based on independent variables, the propagation of uncertainty can be estimated based on a statistical theorem. For a linear function y of n independent variables x_i with standard deviation σ_i, the standard deviation of y is:

$$\sigma_y = \sqrt{\left(\sum_{i=1}^{n} \frac{\partial y}{\partial x_i}\right)^2} \tag{A.7}$$

For a calculated result y, a function of n independent variables, $x_1, x_2, ..., x_n$, each with experimental uncertainty, $u_1, u_2, ..., u_n$, the propagated uncertainty is u_y. To estimate u_y, each uncertainty is assumed to be small enough that a first-order Taylor expansion of $y(x_1, x_2, ..., x_n)$ is a reasonable approximation:

$$y(x_1 + u_1, x_2 + u_2, ..., x_n + u_n) \approx y(x_1, x_2, ..., x_n) + \sum_{i=1}^{n} \frac{\partial y}{\partial x_i} u_i \tag{A.8}$$

Under this assumption, y is a linear function of independent variables. Theorem A.7 is applicable to y, assuming that uncertainties behave much like standard deviations:

$$u_y = \sqrt{\sum_{i=1}^{n} \left(\frac{\partial y}{\partial x_i} u_i \right)^2} \tag{A.9}$$

Normally, the bias uncertainties and precision uncertainties in y are propagated separately. The overall uncertainty, U_y, is then calculated as a root-sum-square of the two uncertainties, B_y and P_y:

$$U_y = \sqrt{B_y^2 + P_y^2} \tag{A.10}$$

U_y is a measure of the largest error reasonably expected.

In experimental applications, the bias errors and the precision errors are often impossible to estimate because the exact value of the quantity being measured is not known and the sample of measurements of a single quantity under the same conditions is very small. Also, many sources of errors are difficult to identify. In light of the engineering reality, an aggregate estimate of the experimental error is often used in lieu of the bias and random uncertainties.

A.4 Pressure and Temperature Measurements

The driver behind the 2:1 pressure ratio turbine tests was to generate high accuracy experimental measurements of performance. The mass flow probe was developed with this purpose in mind. The uncertainty associated with the three measurements - total and dynamic pressure and total temperature - is estimated below as well as the propagated error in the Mach number and mass flow calculations.

Total Temperature Measurements

The total temperature is measured using Omega $0.0005in$ diameter type K thermocouples inside an impact head. The accuracy of the sensor was studied by Cai [9]. There are four major sources of error: the calibration error, the conduction error, the radiation error and

the error due to the recovery factor. The bias error was found to be 0.1% and the precision error 0.05% [24].

Total Pressure Measurements

The total pressure was measured using a Kiel probe and 100 psid Kulite sensor, calibrated with a two-point calibration. Cai estimated the total pressure measurement uncertainty to be less than 0.5% for the bias component and less than 0.1% for the precision component [9].

Dynamic Pressure Measurements

The dynamic pressure is measured using a Kulite 5 psid sensor connected to a Pitot tube and calibrated using a Setra 1 psid sensor as a reference. Non-linearity is the principle source of bias uncertainty in the Kulite measurement (0.5% $FS = 0.025\ psi$). This uncertainty, however is reduced by calibrating the sensor in the region of interest during the test. The bias uncertainty then can be taken to be the bias uncertainty of the Setra sensor or 0.3% $FS = 0.003\ psi$. The precision uncertainty for the Kulite is quoted to be 0.1% $FS = 0.005\ psi$, but can be reduced to 0.02% $FS = 0.001\ psi$ by taking $n = 30$ or more successive measurements.

This analysis only accounts for sensor uncertainty and neglects uncertainties due to the design of the Pitot and Kiel probes. These sources of uncertainty might be important and should be quantified in subsequent studies by calibrating the probe and sensor in a wind tunnel.

Ratio of Specific Heats

Keogh estimated the uncertainty in the specific heat at constant pressure, C_p, to come from a bias of 0.2%. The ratio of specific heats can be calculated from C_p using the relationship for an ideal gas:

$$C_p = \frac{\gamma R}{\gamma - 1} \tag{A.11}$$

Quantity	C_*	B	S	n	U_{95}
P_t	0.5	0.5%	0.1%	30+	0.5%
δP	0.5	1.0%	0.3%	30+	1.0%
γ	0.5	0.001%	–	–	0.001%
M	–	0.6%	0.2%	30+	0.6%

Table A.1: Propagated uncertainty in Mach number measurements.

Hence, the bias uncertainty in γ can be calculated as:

$$B_\gamma = \frac{R}{(C_p - R)^2} B_{C_p} \tag{A.12}$$

For the 2:1 pressure ratio turbine experiments conducted in CO_2, the uncertainty in γ is less than 0.001%.

A.5 Uncertainty in Mach Number Calculations

Mach number is inferred from the dynamic pressure, δP, and stagnation pressure, P_t using the compressible flow Equation 2.3. The propagated bias and precision uncertainties can be calculated as:

$$\frac{\epsilon_M}{M} = \frac{\sqrt{\left(\frac{\partial M}{\partial P_t}\right)^2 \epsilon_{P_t}^2 + \left(\frac{\partial M}{\partial \delta P}\right)^2 \epsilon_{\delta P}^2 + \left(\frac{\partial M}{\partial \gamma}\right)^2 \epsilon_\gamma^2}}{M} \tag{A.13}$$

Defining the influence coefficient for each variable as:

$$C_* = \frac{\partial M}{\partial *} \cdot \frac{*}{M} \tag{A.14}$$

Equation A.13 can be rewritten as:

$$\frac{\epsilon_M}{M} = \sqrt{\left(C_{P_t} \cdot \frac{\epsilon_{P_t}}{P_t}\right)^2 + \left(C_{\delta P} \cdot \frac{\epsilon_{\delta P}}{\delta P}\right)^2 + \left(C_\gamma \cdot \frac{\epsilon_\gamma}{\gamma}\right)^2} \tag{A.15}$$

A summary of the influence coefficients and the uncertainties is presented in Table A.1.

A.6 Uncertainty in Mass Flow Calculations

The mass flow is obtained by rearranging the compressible flow equation for the non-dimensional mass flow (Equation 2.4). As for the Mach number, the uncertainty in the calculation can be expressed as:

$$\frac{\epsilon_{\dot{m}}}{\dot{m}} = \frac{\sqrt{\left(\frac{\partial \dot{m}}{\partial P_t}\right)^2 \epsilon_{P_t}^2 + \left(\frac{\partial \dot{m}}{\partial \delta P}\right)^2 \epsilon_{\delta P}^2 + \left(\frac{\partial \dot{m}}{\partial T_t}\right)^2 \epsilon_{T_t}^2 + \left(\frac{\partial \dot{m}}{\partial \gamma}\right)^2 \epsilon_{\gamma}^2 + \left(\frac{\partial \dot{m}}{\partial A_{eff}}\right)^2 \epsilon_{A_{eff}}^2}}{\dot{m}} \tag{A.16}$$

or in terms of the influence coefficients:

$$\frac{\epsilon_{\dot{m}}}{\dot{m}} = \sqrt{\left(C_{P_t}\frac{\epsilon_{P_t}}{P_t}\right)^2 + \left(C_{\delta P}\frac{\epsilon_{\delta P}}{\delta P}\right)^2 + \left(C_{T_t}\frac{\epsilon_{T_t}}{T_t}\right)^2 + \left(C_{\gamma}\frac{\epsilon_{\gamma}}{\gamma}\right)^2 + \left(C_{A_{eff}}\frac{\epsilon_{A_{eff}}}{A_{eff}}\right)^2} \tag{A.17}$$

where:

$$C_* = \frac{\partial \dot{m}}{\partial *} \cdot \frac{*}{\dot{m}} \tag{A.18}$$

At this point, too little data is available to generate a correlation between the test conditions and the effective area and hence, an uncertainty for that measurement is not available. It was therefore ignored for the calculation of the mass flow uncertainty. The uncertainty calculated is in fact the uncertainty in the mass flow per unit area. Producing a correlation of the effective area with Reynolds number will have two conflicting consequences. The uncertainty in the mass flow measurement might be greater because of the uncertainty in the correlation. However, the correlation will decrease the bias uncertainty in the mass flow measurement because the reference used - the Venturi mass flow measurement - has a smaller bias error associated with it. A summary of the influence coefficients and the uncertainties in the mass flow per unit area calculations is presented in Table A.2.

Quantity	C_*	B	S	n	U_{95}
P_t	0.5	0.5%	0.1%	30+	0.5%
δP	0.5	1.0%	0.3%	30+	1.0%
T_t	0.5	0.1%	0.05%	30+	0.1%
γ	0.002	0.001%	–	–	0.001%
$\dot{m}$	–	0.6%	0.2%	30+	0.6%

Table A.2: Propagated uncertainty in mass flow measurements.

A.7 Summary

The uncertainty associated with calculating Mach number and mass flow using measurements of total and differential pressure and total temperature was assessed. Both propagated uncertainties were found to be less than 1%. The estimate, however, accounted only for uncertainties in the sensor measurements and neglected the effect of the probe on the flow being measured. The recovery factor of the pressure probes should be assessed by calibrating the instruments in a wind tunnel.

The greatest source of uncertainty in the calculation of Mach number and mass flow was the bias uncertainty in the differential pressure measurement, due to the non-linearity of the Kulite sensor. The impact of this source of uncertainty can be reduced by using a multi-point calibration for the sensor.

Appendix B

PIV Measurement Error Analysis

B.1 Introduction

All experimental measurements carry uncertainty. PIV is no exception. The experimental procedure and data reduction are, however, so complicated that the overall uncertainty is very difficult to accurately calculate. It is nonetheless important to bound it in order to compare PIV measurements with theoretical calculations. This appendix presents the significant sources of error in a PIV experiment and an estimate for their magnitude.

B.2 Sources of Uncertainty

The process of obtaining a velocity flow field using PIV includes many steps and utilizes many instruments. To thoroughly survey the sources of error, each step in the PIV process is analyzed in turn.

Optical Distortions

The PIV pictures are captured through a series of glass window and optical lenses, generating optical distortions in the image. To quantify the distortion of the entire optical system, a calibration grid located in the plane of the laser light sheet was photographed. The local distortion was calculated by measuring the pixel length of segments of known dimension throughout the image. Several hundred samples were taken. The statistics of

Direction	Mean	Standard Deviation
Axial	17.10 $\mu m/pixel$	0.14 $\mu m/pixel$
Circumferential	17.58 $\mu m/pixel$	0.19 $\mu m/pixel$

Table B.1: Statistics from the calibration of the PIV optical set-up.

the calibration is presented in Table B.1.

All PIV pictures were processed using the mean scales in Table B.1 to transform velocities in $pixels/s$ into m/s. The scales can be bound for a confidence interval of 95%. In the axial direction, the scale is 17.10 $\mu m/pixel \pm 0.23$ $\mu m/pixel$ and in the circumferential direction, it is 17.58 $\mu m/pixel \pm 0.31$ $\mu m/pixel$. This implies a bias uncertainty of 1.3% in axial velocity and 1.8% in circumferential velocity.

Rotor Speed

The rotor speed is used in the PIV data reduction to calculate velocity in the rotor inertial frame. It is obtained by integrating the signal from a once-per-revolution sensor located on the rotor shaft. The acquisition speed is 3000 Hz and a revolution takes 8.25 ms on average. This implies that the precision uncertainty in the measurement of angular speed is $\pm 2\%$. However, the error can be considerably reduced by curve fitting the data.

Auto-Correlation

The velocity is calculated by measuring the distance between the image of a particle at two successive instants of time. A digital PIV image is a discrete medium made of unit blocks called pixels. Hence, the size of a pixel restricts the accuracy of the measurement of the distance between two paired particle images. The distance is calculated by correlating a region surrounding one of the particles onto the region surrounding the second particle. Bons estimated the accuracy of this process to be less than 0.5 $pixels$ [6]. Depending on the local velocity magnitude, the coarseness of the digital image can be responsible for precision uncertainty in the measurement of velocity ranging from 2.5% to 10%.

Quantity	Uncertainty	Type
Optical distortion (axial)	$\pm 1.3\%$	bias
Optical distortion (circumferential)	$\pm 1.8\%$	bias
Rotor speed	$\pm 2\%$	precision
Cross-correlation	$\pm 2.5\% - 10\%$	precision
Pair mismatching	?	–
Velocity vector position	$\pm 0.00001\ m$	precision
Flow tracking capabilities	$\pm 1\% - 100\%$	–

Table B.2: Sources of uncertainty in PIV measurements.

Mismatching of Particle Pairs

In regions where the particle density is high, the particle matching algorithm can potentially pair particles that do not belong together. The uncertainty associated with this is difficult to quantify. In general, spurious vectors are detected during the image processing sequence. However, as many as 5% of vectors are expected to be mismatched in a reduced flow field.

Velocity Vector Position

The origin of the velocity vectors was taken as the half-way point between paired particles. The uncertainty in the position is expected to be less than 0.5 *pixels* as it is based on the correlation procedure presented above. This translates into a precision uncertainty of 0.00001 m in both the axial and circumferential directions.

Flow Tracking Properties of the Seed Particles

The principle of PIV is to use the Lagrangian velocity of seed particles to estimate the Eulerian velocity of the fluid. The accuracy of this technique is highly contingent on the choice of the seeding material. As discussed in detail in Chapter 5, the diameter of the seed particles determined their tracking capabilities. In fact, trajectory and velocity errors of 100% are noticed for diameters only five times greater than the optimum diameter.

B.3 Summary

There are many sources of error associated with the PIV process, many of which are unknown or not quantifiable. For example, the accuracy of the digitalization process from photographic film to digital image is unknown; the accuracy of numerical steps such as correlation are difficult to estimate; the uncertainty associated with the 3-dimensional behavior of the flow cannot be quantified without a 3-D solution of the flow. In addition, it is impossible to quote an overall figure for the error of a given PIV measurement because the relationship between the different sources of error is unknown and uncertainties cannot be aggregated easily. Table B.2 gives a summary of the sources of uncertainty identified above.

BIBLIOGRAPHY

[1] ABHARI, R. S. *An Experimental Study of the Unsteady Heat Transfer Process in a Cooled Fully Scaled Transonic Turbine Stage.* Ph.D. thesis, Massachusetts Institute of Technology, January 1991.

[2] ABHARI, R. S., GUENETTE, G. R., EPSTEIN, A. H., AND GILES, M. B. "Comparison of Time-Resolved Turbine Rotor Blade Heat Transfer Measurements and Numerical Calculations". *ASME Gas Turbine Conference* (Orlando FL, June 1991).

[3] ADRIAN, R. J. "Particle-Imaging Techniques for Experimental Fluid Mechanics". *Annual Review of Fluid Mechanics, Vol. 23* (1991), pp. 261–304.

[4] THE AMERICAN SOCIETY OF MECHANICAL ENGINEERS. *Measurement Uncertainty: Intruments and Apparatus*, 1990.

[5] BECKWITH, T. G., MARANGONI, R. D., AND LIENHARD, J. H. *Mechanical Measurements*, fifth ed. Addison-Wesley Publishing Company, 1993.

[6] BONS, J. P. *Complementary Velocity and Heat Transfer Measurements in a Rotating Turbine Cooling Passage.* Ph.D. thesis, Massachusetts Institute of Technology, September 1997.

[7] BRYANSTON-CROSS, P. J., AND EPSTEIN, A. H. "The Application of Sub-Micron Particle Visualisation for PIV (Particle Image Velocimetry) at Transonic and Supersonic Speeds". *Progress in Aerospace Science, Vol. 27* (1990), pp. 237–265.

[8] BRYANSTON-CROSS, P. J., EPSTEIN, A. H., GRÉPIN, L., GUENETTE, G. R., AND D'HOOP, E. "Detailed PIV and Flowfield Measurements in a Transonic Turbine". Tech. rep., Massachusetts Institute of Technology, February 1998.

[9] CAI, Y. "Aerodynamic Performance Measurements in a Fully Scaled Turbine". Master's thesis, Massachusetts Institute of Technology, February 1998.

[10] CHANA, K. S., HEALEY, N., AND BRYANSTON-CROSS, P. J. "Particle Image Velocimetry Measurements from Stator-Rotor Interaction Region of a High Pressure Transonic Turbine Stage at the DERA Isentropic Light Piston Facility". *Non-Intrusive Measurements for Propulsion Engines* , 98th AGARD Symposium, (Bruxells, October 1997).

[11] D'HOOP, E. M. "Flowfield Measurements in a Transonic Turbine". Master's thesis, Massachusetts Institute of Technology, 1995.

[12] DOWLING, A. P., AND WILLIAMS, J. E. F. *Sound and Sources of Sound.* Ellis Horwood Limited, 1983.

[13] DRING, R. P., CASPAR, J. R., AND SUO, M. "Particle Trajectories in Turbine Cascades". *Journal of Energy, Vol. 3*, No. 3 (May-June 1979), pp. 161–166.

[14] EPSTEIN, A. H., GUENETTE, G. R., AND NORTON, R. J. D. "The Design of the MIT Blowdown Turbine Facility". Gas Turbine Laboratory Report 183, Massachusetts Institute of Technology, 1985.

[15] GILES, M. B. "UNSFLO: A Numerical Method for Unsteady Inviscid Flow in Turbomachinery". Gas Turbine Laboratory Report 195, Massachusetts Institute of Technology, October 1988.

[16] GILES, M. B. "UNSFLO: A Numerical Method for the Calculation of Unsteady Flow in Turbomachinery". Gas Turbine Laboratory Report 205, Massachusetts Institute of Technology, March 1991.

[17] GILES, M. B., AND HAIMES, R. "Validation of a Numerical Method for Unsteady Flow Calculations". *ASME Journal of Turbomachinery, Vol. 115* (January 1993), pp. 110–117.

[18] GOSS, L. P., POST, M. E., TRUMP, D. D., AND SARKA, B. "A Novel Technique for Blade-to-Blade Velocity Measurements in a Turbine Cascade". *AIAA/ASME/SAE/ASEE 25th Joint Propulsion Conference* (Monterey, CA, July 1989).

[19] GRANT, H. F. "Measuring Time-Averaged Stagnation Pressure in a Pulsatile Air Flow". *ISA 23rd International Instrumentation Symposium* (Las Vegas, Nevada, May 1977).

[20] GUENETTE, G. R. *A Fully Scaled Short Duration Turbine Experiment.* Sc.D. thesis, Massachusetts Institute of Technology, 1985.

[21] HINSCH, K. D. "Three-Dimensional Particle Velocimetry". *Measurement Science & Technology, Vol. 6*, No. 6 (June 1995), pp. 742–753.

[22] HINZE, J. O. *Turbulence: An Introduction to its Mechanics and Theory.* McGraw-Hill Book Company Inc., 1959.

[23] JONES, G. S., KAMEMOTO, D. Y., AND GARTRELL, L. R. "An Investigation of the Effects of Seeding in Laser Velocimetry Systems". *28th Aerospace Sciences Meeting* (January 8-11 1990).

[24] KEOGH, R. "Shaft Efficiency Measurements of a Fully Scaled Turbine in a Short Duration Facility". Master's thesis, Massachusetts Institute of Technology, February 1998.

[25] KREYSZIG, E. *Advanced Engineering Mathematics*, sixth ed. John Wiley & Sons, 1988.

[26] SCHLICHTING, H. *Boundary Layer Theory.* McGraw Hill Inc., 1951.

[27] SHANG, T. *Influence of Inlet Temperature Distortion on Turbine Heat Transfer.* Ph.D. thesis, Massachusetts Institute of Technology, February 1995.

[28] WERNET, M. P. "PIV for Turbomachinery Applications". *Conference on Optical Technology in Fluid, Thermal and Combustion Flow III* (August 1997).